



THÈSE

En vue de l'obtention du

DOCTORAT DE L'UNIVERSITÉ DE TOULOUSE

Délivré par :

Institut Supérieur de l'Aéronautique et de l'Espace

Présentée et soutenue par :

Manar GUNASILAN

le vendredi 16 novembre 2018

Titre :

Crack arrest capability of aluminium alloys under dynamic loading

Capacité d'arrêt de fissure dans les alliages d'aluminium sous chargement dynamique

École doctorale et discipline ou spécialité :

ED MEGeP : Génie mécanique, mécanique des matériaux

Unité de recherche :

Institut Clément Ader

Directeur(s) de Thèse :

M. Patrice LONGERE (directeur de thèse)

Jury :

M. Olivier PANTALÉ Professeur ENI Tarbes - Président

M. Patrice LONGERE Professeur ISAE-SUPAERO - Directeur de thèse

Mme Catherine FROUSTEY Maître de conférences Université Bordeaux - Rapporteur

M. Éric MARKIEWICZ Professeur Université Valenciennes et du Hainaut-Cambrésis -
Rapporteur

Abstract

Understanding the dynamic behaviour and failure of materials is the key for a robust design regarding accidental overloading and/or optimisation of high-speed fabrication conditions. In the present study, aluminium alloys, viz. AA2024-T351 and AA7175-T7351 widely used for aeronautical applications, are considered.

The first part of the present work focuses on the thermomechanical characterization of the materials under consideration. Tension, compression and shear tests were carried out at various strain rates and temperatures by using conventional testing machines and split Hopkinson pressure bar. The strain rate range was 10^{-3} s^{-1} to 4500 s^{-1} , and the temperature range was from 30°C to 200°C . Relaxation tests were also carried out in order to determine the viscous part of the yield stress. When needed, both digital image correlation method (DIC) and mechanical extensometer were used to measure the strain. The specimens' initial and post-mortem microstructure was observed using scanning electron microscope (SEM).

The experimental results show that the alloys have a very different strain hardening capability while having in common a slight strain rate dependence and high temperature dependence. Under tension loading at various temperatures, the fracture of AA2024 is controlled by void growth whereas for AA7175 there seems to exist a critical temperature (around 100°C) below which the fracture is mostly controlled by shear decohesion and above which it becomes mostly controlled by void growth. Under shear and compression loading at high strain rate, AA2024 exhibit a stable behaviour whereas AA7175 is subject to premature failure under adiabatic shear banding.

The second part of the study is devoted to the experimental investigation of the crack arrest capability of both alloys under impact loadings. Kalthoff and Winkler (KW) type impact tests were carried out by using gas launcher. The projectile velocity range was $100 \text{ m}\cdot\text{s}^{-1}$ to $230 \text{ m}\cdot\text{s}^{-1}$. A plate type specimen with two notches representing a pre-cracked structure was used for KW impact tests. High speed camera was used to record the projectile and plate interaction at 10^5 to 10^6 frames per second. The aim was notably to identify and compare the critical impact velocity, defined as the impact velocity above which the plate is wholly fractured, for both alloys. Post-mortem microstructure was observed using scanning electron microscope (SEM) and nano-hardness of the area in the proximity of the crack formed after impact test was determined by nano-indentation apparatus.

KW impact tests show that AA7175 has a lower critical impact velocity compared to AA2024. Furthermore, the appearance of adiabatic shear bands can be seen in the recorded frames during the plate and projectile interaction for AA7175. Microstructure observation of the KW impact test specimen shows that, for AA2024 the fracture was combination of Mode I and Mode II whereas for AA7175 the fracture was dominated by Mode II. The fractured lip surface of KW type impact test specimen reveals the formation of adiabatic shear bands on AA7175. Nano-hardness test results show a hard process zone for AA2024 and soft process zone for AA7175 near the crack region.

The third part of the study is focused on developing a constitutive modelling of the behaviour of the two alloys under consideration in view of further numerical simulations. Matlab R2013a software was used to identify the influence of variables and calibrate constants by curve fitting method. The influence of plastic strain, strain rate and temperature was taken

into account to develop constitutive models. The models were calibrated by experimental results and show good correlation at the considered strain rate and temperature ranges. The constitutive models still have to be implemented into a commercial finite element computation code, e.g. Abaqus, and verified and validated on initial boundary value problems.

Keywords: Aluminium alloys, high strain rate, adiabatic shear band, damage tolerance

Résumé

La compréhension du comportement et de la rupture dynamiques des matériaux est la clé pour une conception robuste à la surcharge accidentelle et/ou l'optimisation des conditions de fabrication à grande vitesse. Dans l'étude présente, les alliages d'aluminium AA2024-T351 et AA7175-T7351, largement utilisés pour des applications aéronautiques, sont considérés.

La première partie du travail présenté se concentre sur la caractérisation thermomécanique des matériaux de l'étude. Des tests de traction, compression et cisaillement ont été effectués à différentes vitesses de déformation et températures en utilisant des machines de test conventionnelles et un dispositif de barres de Hopkinson. La gamme de vitesses était 10^{-3} s^{-1} à 4500 s^{-1} et la gamme de températures de 30°C à 200°C . Des essais de relaxation ont été aussi effectués pour déterminer la partie visqueuse de la contrainte d'écoulement. Quand nécessaire, la méthode de corrélation d'image (DIC) et l'extensométrie mécanique ont été utilisées pour mesurer la déformation. La microstructure initiale et post-mortem des éprouvettes a été observée en utilisant un microscope électronique à balayage (MEB).

Les résultats expérimentaux montrent que les alliages ont une capacité d'érouissage différente et ont en commun une dépendance légère à la vitesse et forte à la température. En traction à différentes températures, la rupture de l'AA2024 est contrôlée par la croissance de cavités tandis que pour l'AA7175 il semble exister une température critique (autour 100°C) au-dessous de laquelle la rupture est surtout contrôlée par la décohesion de cisaillement et au-dessus de laquelle elle devient surtout contrôlé par la croissance de cavités. Sous cisaillement et compression à grande vitesse, l'AA2024 exhibe un comportement stable tandis que l'AA7175 est soumis à une rupture prématurée par cisaillement adiabatique.

La deuxième partie de l'étude est consacrée à l'investigation expérimentale de la capacité d'arrêt de fissure sous impact des deux alliages. Des essais d'impact de type Kalthoff et Winkler (KW) ont été effectués en utilisant un lanceur à gaz. La gamme de vitesse de projectile était 100 m.s^{-1} à 230 m.s^{-1} . Une plaque avec deux entailles représentant une structure pré-fissurée a été utilisée pour les tests d'impact. Des caméras à grande vitesse ont été utilisées à des vitesses de 10^5 à 10^6 images par seconde. Le but était notamment d'identifier et comparer la vitesse d'impact critique, au-dessus de laquelle la plaque est complètement rompue, pour les deux alliages. La microstructure post-mortem a été observée par MEB et la nano-dureté de la zone dans le voisinage de la fissure après impact a été déterminée par un appareil de nano-indentation.

Les tests d'impact KW montrent que l'AA7175 a une vitesse d'impact inférieure à celle de l'AA2024. En outre, l'apparition de cisaillement adiabatique est visible sur les images enregistrées pendant l'interaction projectile/plaque pour l'AA7175. L'observation de la microstructure des plaques impactées montre que pour l'AA2024 la rupture est la combinaison des Modes I et II tandis que pour l'AA7175 la rupture est dominée par le Mode II. La surface des lèvres de la fissure révèle la formation de cisaillement adiabatique pour l'AA7175. Les résultats de test de nano-dureté montrent une zone d'élaboration dure pour l'AA2024 et molle pour l'AA7175 près de la fissure.

La troisième partie de l'étude est consacrée au développement d'un modèle constitutif du comportement des deux alliages en vue de simulations numériques. Le logiciel Matlab R2013a a été utilisé pour identifier l'influence de la déformation plastique, de la vitesse de

déformation et de la température et calibrer les constantes. Les modèles ont été calibrés par des résultats expérimentaux et montrent une bonne corrélation. Les modèles constitutifs doivent encore être implémentés dans un code de calcul par éléments finis commercial, p.ex. Abaqus, et vérifiés et validés sur des problèmes de structures.

Mots clés: Alliages d'aluminium, dynamique rapide, cisaillement adiabatique, tolérance aux dommages

Acknowledgements

First and foremost I would like to express my sincere gratitude to my supervisor Professor Patrice Longère, who guided me and provided the resources to accomplish my goal. He had spent countless hours to discuss various aspect of my research. This work would not be possible without his guidance and help.

Special thanks goes to Véronique Godivier for assisting on usage of scanning electron microscope, Olivier Cherrier and Dr. Emile Roux for helping in carrying out dynamic compression test using split Hopkinson pressure bar, Marc Chartrou for assisting in carrying out tension and compression tests, Alexandre Chardonneau for helping to carry out impact test by using gas launcher and set up tension test using digital image correlation method, Thierry Martin and César Moisés Sanchez Camargo for assisting in conducting nano-hardness test.

I would like to thank workshop team led by Mr Daniel Gagneux for various specimen fabricated during this work.

I thank all my fellow PhD students at Institut Clément Ader for their support, friendliness and all the encouragements. All of my friends in Toulouse, back in Malaysia and abroad have to be thanked for the inspiring and motivating discussions.

I would like to thank National Defence University of Malaysia and Airbus Helicopter France for funding my study in ISAE-SUPAERO.

Last but not least, this important milestone of my life would not have been possible without the precious support from my grandparents, my mother and father, my brothers and sisters.

Gunasilan Manar

Scientific Communications

International peer reviewed journal article

- [ACL1] G. Manar, P. Longère. Crack arrest capabilities of AA2024 and AA7175 aluminium alloys under impact loading. Submitted in Engineering Failure Analysis. 2018

National or International conference proceedings

- [ACT1] G. Manar and P. Longère. Comparative failure of AA2024 and AA7175 at low and high strain rate. Proceedings of M2D2017, 7th International Conference on Mechanics and Materials in Design, Albufeira (Portugal), 11-15 June 2017
https://paginas.fe.up.pt/~m2d/Proceedings_M2D2017/data/papers/6775.pdf
- [ACT2] G. Manar and P. Longère. Shear failure of AA2024 and AA7175 under high strain rate loading. Proceedings of ICEAFV, 5th International Conference of Engineering Against Failure, Chios (Greece), 20-22 June 2018

https://www.matec-conferences.org/articles/mateconf/pdf/2018/47/mateconf_iceaf-v2018_02005.pdf
- [ACT3] G. Manar, N. Mat Jali, P. Longère, Dynamic crack arrest capability of some metallic alloys and polymers, Proceedings of DYMAT, 12th International Conference on Mechanical and Physical Behaviour of Materials under Dynamic Loading, Arcachon (France), 9-14 September 2018

International or national conference without proceedings

- [COM1] G. Manar, P. Longère, E. Roux, A. Hor and M. Salem. Effect of strain rate on the behavior and failure of 2024 and 7075 aluminium alloys. DSTC 2016, 3rd International Conference on Defence and Security Technology, Kuala Lumpur (Malaysia), 15-17 August 2016
- [COM2] G. Manar, P. Longère. Crack arrest capability of aluminium alloys under dynamic loading. ICEFA VIII, 8th International Conference on Engineering Failure Analysis, Budapest (Hungary), 8-11 July 2018

Table of Contents

- 1. Introduction**..... 1
 - 1.1 Background study..... 1
 - 1.2 Aluminium alloys in the context of aerospace and aeronautical..... 2
 - 1.3 Research objective..... 4
 - 1.4 Thesis outline 4
 - 1.5 References 5
- 2. Thermo- mechanical characterization** 7
 - 2.1. Introduction 8
 - 2.2 Materials under consideration 10
 - 2.3 Experimental procedure 10
 - 2.4 Results and discussion..... 27
 - 2.5 Conclusion..... 57
 - 2.7 References 58
- 3. Crack arrest capabilities of AA2024 and AA7175 aluminium alloys under impact loading** 61
 - 3.1 Introduction 62
 - 3.2 Experimental procedure 64
 - 3.3 Results and analysis 70
 - 3.4 Summary 90
 - 3.5 Concluding remarks 94
 - 3.7 References 95
- 4. Constitutive modelling**..... 97
 - 4.1 Introduction 98
 - 4.2 Modelling procedure 98
 - 4.3 Application to AA2024 and AA7175..... 103
 - 4.4 Conclusion..... 117
 - 4.5 References 118
- 5. Conclusions and future scopes** 119
 - 5.1 Conclusion on thermo-mechanical characterization 119

5.2	Conclusion on crack arrest capability of aluminium alloys	119
5.3	Conclusion on constitutive modelling.....	120
5.4	Future works on thermomechanical characterization.....	120
5.5	Future works on crack arrest capability	120
5.6	Future works on constitutive modelling.....	121
	Bibliography	123

1. Introduction

1.1 Background study

On 17 July 2014, the Malaysian airline MH17, boeing 777 aircraft from Amsterdam to Kuala Lumpur was attacked by using BUK surface to air missile system. The impact took place about 30 seconds after the missile was launched at the altitude of about 10,060 m. Due to the BUK missile explosion, about 800 pre formed fragments perforated and heavily damaged the structure near the cockpit, thus separated the fuselage of the aircraft into three parts. Fig. 1. 1(a) and Fig. 1. 1(b) shows the blast load on Boeing 777 commercial aircraft and fractured fuselage due to the blast load. This type of fatal aggression is fortunately rare. What is more frequent is damage due to bird strike and hail storm on aircraft wing structure as shown in Fig. 1. 2(a) and Fig. 1. 2(b). Annual cost for repairing the damages associated with wildlife strikes on aircraft is about USD1.2 billion worldwide where 97% of the reported case in the United States is due to bird strike and this number is affecting the aviation industry which is trying to reduce the overall cost [2-3]. Another important damage on aircraft structure is due to hailstones impact. Hailstones can impact the aircraft either during cruise or on ground and depending on velocity it can experience large deformation and fragmentation [3], [4].



Fig. 1. 1 Explosive load on boeing 777 aircraft by ground to air missile [5][6]

Dynamic failure of ductile materials is invoked in a wide range of situations including high-speed manufacturing process and structures exposed to impact loading, explosive loading or during crash event, accident, etc. [7]. The residual structural integrity and material strength play a major role to be considered for this type of accidental event. Indeed, the question is arising on how this pre-damaged or pre-cracked structure will sustain further dynamic loading in order to guarantee a structure's integrity and security. Materials for airframes need to be chosen based on its required properties to be able to sustain the corresponding loading conditions. Properties like strength, Young's modulus, fatigue initiation, fatigue growth, corrosion are important but the design consideration will be limited by fracture toughness [8]. Manufacturing process like rolling, extrusion, forging and surface treatment method involve plastic deformation and it is essential to understand the behaviour of the corresponding materials.



(a) Cessna 206 H ATA 5700 wing structure



(b) Boeing A737 horizontal stabilizer

Fig. 1. 2 Damage on aircraft structure due to (a) Bird strike [9] (b) Hail stones impact during cruise[10]

1.2 Aluminium alloys in the context of aerospace and aeronautics

Aluminium alloys have been used as a primary airframe materials since 1930 due to their well-known performance, low weight to strength ratio, established manufacturing process and reliable inspection technique thus able to reduce the overall cost [11], [12]. In the recent years, the usage of the composite materials are increasing in the aircraft such as B787 and A380. Although composites has a higher specific stiffness, specific strength , fatigue and corrosion resistance but their drawback is low impact resistance, less adaptability to sudden changes to environmental condition such as humidity, moisture absorption and temperature allow the usage of metallic materials still relevant [12]. Fig. 1. 3 shows the total demand for the aircraft material by weight percentage for the year 2014, where the usage of aluminium alloy is almost half of it.

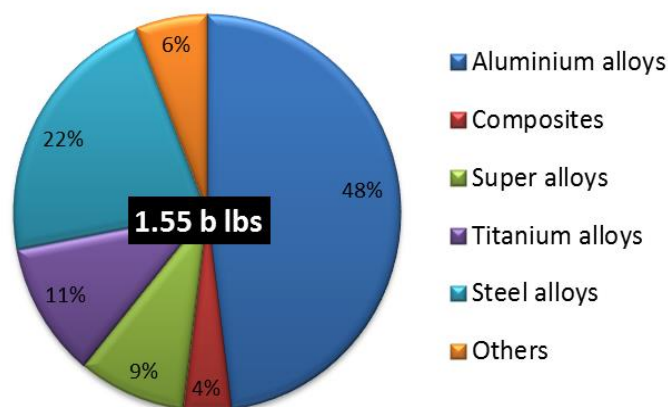
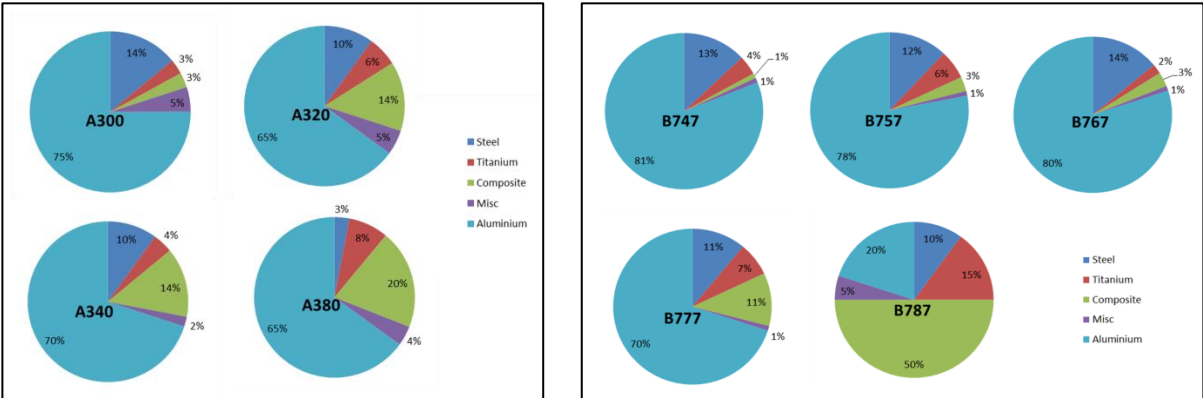


Fig. 1. 3 Total demand for aircraft material by weight percentage for the year 2014[13]

Fig. 1. 4(a) and Fig. 1. 4(b) show, the usage of the main materials for airframe by two major aircraft Production Company, Airbus and Boeing in their aircraft models. The figure shows

that, even though the usage of the composite materials is increasing in the latest commercial aircraft especially for Boeing 787, but the usage of aluminium is still significant.



(a) Airbus aircraft models (b) Boeing aircraft models
Fig. 1. 4 The usage of main materials for airframe by (a) Airbus and (b) Boeing [14]

Two types of materials are considered in this work, which are 2024-T351 and 7175-T7351 aluminium alloys. AA2024-T351 has been solution heat treated, control stretched and naturally aged whereas 7175-T7351 is solution heat treated and artificially aged.

Fig. 1. 5 shows the usage of the 2000 and 7000 series of aluminium alloys in the airbus aircraft in general for all models. Main primary structure of the airframe material is consisting of these two types of aluminium alloys.

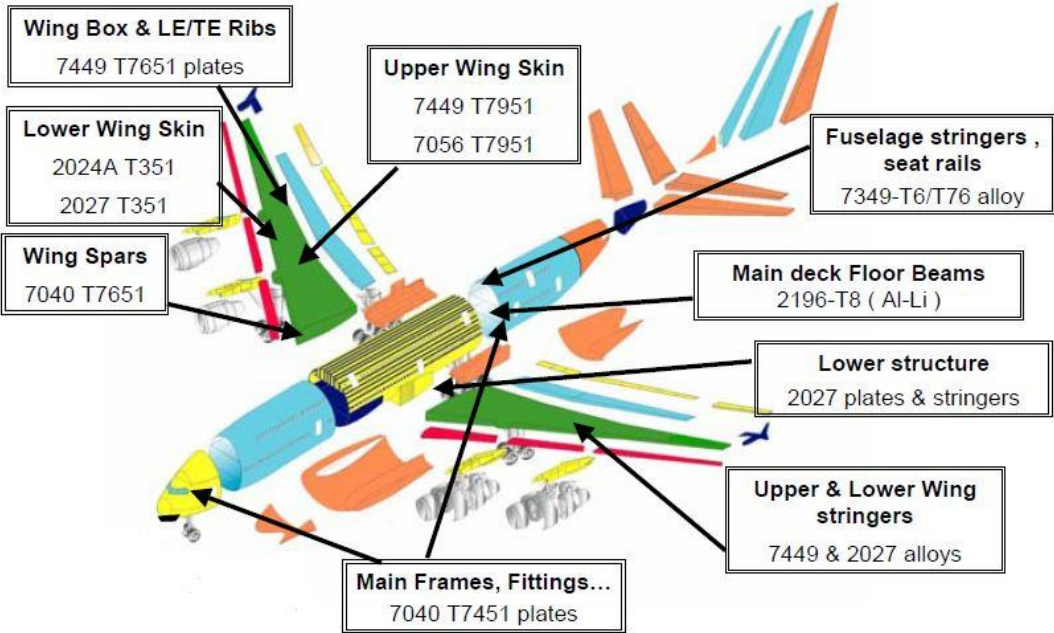


Fig. 1. 5 Usage of 2000 and 7000 series of aluminium alloys in Airbus aircraft parts [14]

1.3 Research objective

Analysis and understanding of fracture mechanisms under large deformation and high strain rate loading in engineering materials is a key point for the design of structures submitted to accidental overloads. After many loading-unloading cycles, small cracks can appear in structures. In the field of aeronautics, (battle) ships or nuclear energy, the knowledge of their propagation conditions when subsequently dynamically reloaded is of interest to prevent accidents and to guarantee the structures security. In the philosophy of the crack arrest capability considered in the present work – not to be confused with the one of the crack arrest standard for brittle fracture–, an engineering structure is supposed to be initially weakened by a crack and the question to answer is how this pre-cracked structure behaves when dynamically reloaded [15]. In the present study, AA2024 and AA7175 aluminium alloys widely used for aeronautical applications are considered.

The present work aims at defining an experimental methodology devoted to study the crack arrest capability of aluminium alloys under impact loading. Tasks notably include

- Development of an experimental procedure of impact testing of notched structures made of the materials under consideration
- Thermomechanical characterization of the behaviour and fracture of the materials under consideration
- Microstructural observation of the ante and post mortem specimens
- Beginning of the constitutive modelling of the behaviour of the materials under consideration

The ultimate objective of this work is to provide industrial design offices with data for their design of aeronautical structures regarding accidental overloading.

1.4 Thesis outline

The present thesis consists of five chapters, appendix and bibliography.

Chapter 2 of the thesis covers the thermomechanical characterization of the materials that are considered in this study, viz. AA2024 and AA7175 aluminium alloys. In this chapter, experimental campaigns were carried out to characterize the material behaviour at various strain rates and temperatures. Tension and compression tests were carried out by using conventional testing machines and split Hopkinson pressure bar. Digital image correlation and mechanical extensometer were used to measure strain for low strain rate tension test. Microstructures of the specimens were observed by using scanning electron microscope (SEM) and optical microscope.

Chapter 3 presents a crack arrest capability of the both aluminium alloys. This chapter explain the details of the Kalthoff and Winkler type impact test that was carried out along with the micro-hardness test on the materials in order to estimate the crack arrest capability of these two alloys at high strain rate deformations. SEM and optical microscopes were used to observe the microstructure of the specimen.

Chapter 4 presents the beginning of the material constitutive modelling based on experimental campaigns that were presented in Chapter 2 on thermomechanical characterization which refers to the theory of the plasticity.

Final chapter is dedicated to conclusion and future scopes. Conclusions are presented separately for each chapter. Improvement and future works are suggested.

1.5 References

- [1] B. F. Blackwell, T. L. DeVault, E. Fernández-Juricic, and R. A. Dolbeer, “Wildlife collisions with aircraft: A missing component of land-use planning for airports,” *Landsc. Urban Plan.*, vol. 93, no. 1, pp. 1–9, 2009.
- [2] J. R. Allan, “The costs of bird strikes and bird strike prevention,” *Hum. Conflicts with Wildl. Econ. Considerations*, no. August, pp. 147–153, 2000.
- [3] S. Abrate, “Soft impacts on aerospace structures,” *Prog. Aerosp. Sci.*, vol. 81, pp. 1–17, 2016.
- [4] I. Neihouse, W. Pepoon, L. Aeronautical, and L. A. Force, “National advisory committee for aeronautics,” *Library (Lond.)*, 1950.
- [5] “Cause of MH17 crash by Dutch Safety Board,” 2015. [Online]. Available: https://www.google.com.my/search?q=mh17&source=lnms&tbn=isch&sa=X&ved=0ahUKEwjP1LfA19vdAhUN-YUKHWN0BRgQ_AUIDigB&biw=1920&bih=945#imgrc=RkLdzNOdbson2M
- [6] “MH-17: The Untold Story. Exploring possible causes of the tragedy.” 2014. [Online]. Available: <https://www.youtube.com/watch?v=iuoIw3jBV4g&t=189s>.
- [7] A. Molinari, S. Mercier, and N. Jacques, “Dynamic failure of ductile materials,” *Procedia IUTAM*, vol. 10, pp. 201–220, 2013.
- [8] J. T. STALEY and D. J. LEGE, “Advances in aluminium alloy products for structural applications in transportation,” *Le J. Phys. IV*, vol. 03, no. C7, pp. C7-179-C7-190, 1993.
- [9] “Flight safety Australia,” 2017. [Online]. Available: <https://www.flightsafetyaustralia.com/2017/08/17-may-to-13-july-2017-4/>.
- [10] “Index of /courstheor/doccourstheo,” 2010. [Online]. Available: <http://www.acop.net/courstheor/doccourstheo/grelejet/Image.image003.jpg@01C778F9.380FAE10.jpg>
- [11] Starke E.A. Jr and Staley J.T., “Application of modern aluminum alloys to aircraft,” *Pergamon*, vol. 32, pp. 131–172, 1996.
- [12] T. Dursun and C. Soutis, “Recent developments in advanced aircraft aluminium alloys,” *Mater. Des.*, vol. 56, pp. 862–871, 2014.
- [13] “Aerospace Supply Chain & Raw Material Outlook,” 2014. [Online]. Available: <https://docplayer.net/7341132-Aerospace-supply-chain-raw-material-outlook.html>.
- [14] K. Rendigs, “Airbus and current aircraft metal technologies.” [Online]. Available: http://www.polishengineers.org/data/history_activities/18.pdf.
- [15] E. Roux, P. Longère, O. Cherrier, T. Millot, D. Capdeville, and J. Petit, “Analysis of ASB assisted failure in a high strength steel under high loading rate,” *Mater. Des.*, vol. 75, pp. 149–159, 2015.

Blank page

2. Thermo-mechanical characterization

Abstract. This chapter presents the thermo-mechanical characterization of the aluminium alloys under consideration, viz. AA2024 and AA7175. An extensive experimental campaign, including tension, compression and shear-compression tests, was carried out in order to study the respective and combined effects of strain, strain rate, temperature and loading path in a wide range of loading conditions. The influence of stress triaxiality is also taken into account by performing tests on the hat shape specimen and also on notched tension specimen. It is shown that AA7175's strength is higher than AA2024's one and that both materials are only slightly rate-dependent and strongly temperature dependent. In addition, AA7175 is subject to premature failure under adiabatic shear banding when submitted to high strain rate loading at low stress triaxiality values. Under positive stress triaxiality, a critical temperature is evidenced above which AA7175's failure results from microvoiding and below which AA7175's failure results from microshear decohesion.

Table of contents

2. Thermo- mechanical characterization	7
2.1. Introduction	8
2.2 Materials under consideration	10
2.3 Experimental procedure	10
2.3.1 Loading cases	10
2.3.1.1 Tension.....	11
2.3.1.2 Compression	13
2.3.1.3 Shear-compression	13
2.3.2 Low strain rate (Quasi static test).....	14
2.3.2.1 Experimental set-ups.....	15
2.3.2.2 Experimental conditions	17
2.3.2.3 Post processing of experimental data (Low strain rate).....	20
2.3.3 High strain rate (Dynamic test)	23
2.3.3.1 Experimental set-up	23
2.3.3.2 Experimental conditions	24
2.3.3.3 Post processing of experimental data (High strain rate)	25
2.3.3.4 Microscopic observation	27
2.4 Results and discussion.....	27
2.4.1 AA2024	28
2.4.1.1 Response under tension and compression loading.....	28
2.4.1.2 Response under shear-compression loading	34

2.4.1.3	Fracture analysis	35
2.4.1.4	Summary	40
2.4.2	AA7175	41
2.4.2.1	Response under tension and compression loading.....	41
2.4.2.2	Response under shear-compression loading	47
2.4.2.3	Fracture analysis	48
2.4.2.4	Summary	54
2.4.3	AA2024 vs AA7175	55
2.4.3.1	Regarding strain hardening	55
2.4.3.2	Regarding strain rate hardening	56
2.4.3.3	Regarding thermal softening	56
2.4.3.4	Regarding fracture.....	56
2.5	Conclusion.....	57
2.6	References	58

2.1. Introduction

Aluminium alloy has been used for about 90 years as primary structural material on for aircraft due to its well-known performance, established design method, manufacturing and reliable inspection technique [1]. The improvement of the aluminium alloys for the aeronautical and aerospace application has been enhanced by understanding the relationship between the composition, processing, microstructure and properties [2].

The aircraft structure can be exposed to extreme loading conditions such as bad weather, bird strike, hail storm, etc., during flight. Understanding the deformation and fracture mechanism under a wide range of high strain rate loadings and stress triaxialities is a key point for the design of the structures submitted to accidental overload [3] or for optimizing the metal forming conditions.

Indeed, stress triaxiality, which is the ratio of the hydrostatic stress over the equivalent stress, is known as one of the important factors that influences the initiation and evolution of ductile fracture in metals and alloys which are governed by void growth [4], [5],[6] . According to Gurson [7], the void nucleation and growth are common in ductile fracture which characterized by large local plastic flow. Fig. 2. 1 shows the relation for equivalent strain to fracture on stress triaxiality. Several tests were performed on 2024-T351 aluminium alloy which cover wide range of stress triaxiality by Bao [8] who found a cut-off value of $-1/3$, in addition the authors show that there is a competition between void growth and shear fracture. Many studies have been done by using specimens with different notch size in order to characterize the effect of the stress triaxiality, see e.g. Achouri et al [9], Bao Y. and Wierbicki [10].

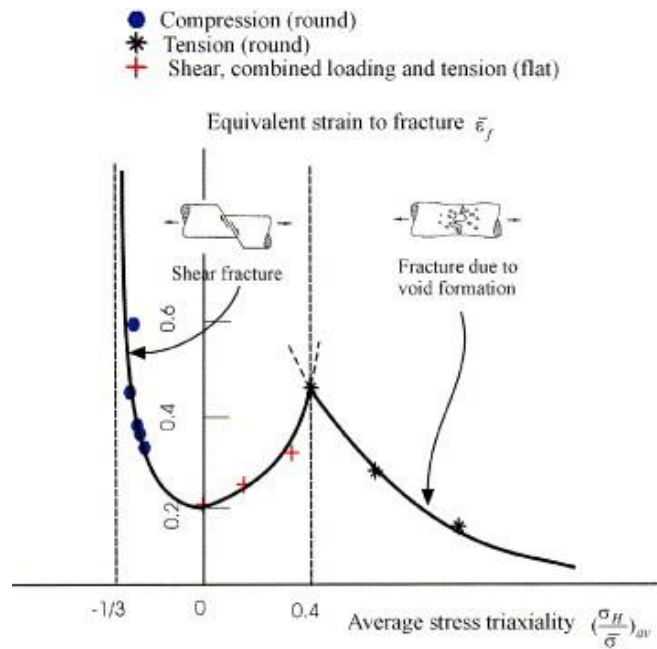


Fig. 2. 1 Equivalent strain to fracture on stress triaxiality [10]

We are here interested in two aluminium alloys widely used in the aerospace sector, viz. AA2024 and AA7175.

Generally speaking, AA2XXX has a good damage tolerance, good fatigue crack growth resistance, high fracture toughness and high ductility due to precipitation of Al_2Cu and Al_2CuMg [1]. Beside the general properties, AA2024 has a moderate yield strength and is a widely used material in fuselage construction.

AA7XXX has higher strength but low corrosion resistance and fracture toughness [1].

AA7XXX is also heat treatable and can provide better strength of all aluminium alloys [1].

Material characterization of this work is focusing on both macroscopic and microscopic factors in view of better understanding the mechanisms of deformation and fracture. Mechanical behavior and fracture of the alloys are studied by conducting thermo-mechanical experiments such as tension and compression under various strain rates, temperatures, and stress triaxialities.

In addition, tests involving shear loading were also carried out in order to obtain results at values of stress triaxiality intermediate between compression and tension. Due to complexity of the stress distribution in the shear region, the interpretation of the experimental results is not straightforward and thus requires specimen with particular geometry shape [11]. This specific shape of the specimen may allow us to study the shear region and possible formation of the ASB. Shear bands, which are one of the precursor for ductile fracture, occur under high strain rate when the rapid local heating due to quasi adiabatic conditions causes intense plastic deformation and hence the name of adiabatic shear bands (ASB) [12]. High strength steel and titanium alloys failure under ASB has been evidenced for long time see e.g. Zener and Holloman [13], Dormeival and Ansart [14], Marchand and Duffy [15], Mazeau et al. [16], Liao and Duffy [17]. Mechanism of ASB that proposed by Froustey et al [18] is linked the multiscale collective behaviour of mesoscopic defects and generation of collective modes of

defects responsible for characteristic stages of strain and damage localization under dynamic loading. ASB was also found under high strain rate deformation on AA7003 by Wu et al [19] The present chapter consists of three main parts. Sub-section 2.3 details the experimental procedure. Sub-section 2.4 presents the results and discussions. Sub-section 2.5 is devoted to the concluding remarks.

2.2 Materials under consideration

The Two types of materials considered in this work are 2024-T351 and 7175-T7351 aluminium alloys. AA2024-T351 alloy has been solution heat treated, control stretched and naturally aged whereas 7175-T7351 is solution heat treated with artificially aged. They are both provided in the form of plates of 6.2 mm and 8 mm thickness for AA2024 and AA7175 respectively.

According to study by Seidt et Gilat, AA2024 does not shows a significant strain rate effect on plastic deformation below 5000 s^{-1} but decrease in stress with increasing temperature and there is no strain hardening at temperature of 300°C [20]. Experimental study by Guang et al, shows that strain rate sensitivity changes from negative to positive for strain rate of 10^{-4} to 9400 s^{-1} and work hardening rates decrease non- linearly with increase of the strain [21]. Nathan et al had found a formation of ASB on AA2024-T351 at higher shear strain rate which is close to $10.5 \times 10^3 \text{ s}^{-1}$ [22].

Quan et al studied the dynamic softening behavior of AA7075 at elevated temperature for different strain rates and found that temperature changes have a significant effect on dynamic softening rate [23]. Kim et al study on AA7175 shows that the strain rate does not affect the fracture toughness until about 600 s^{-1} [24].

The aim of the present work is to go deeper into the thermo-mechanical characterization of both alloys in terms of behavior and fracture. For that purpose tension, compression and shear tests along with post-mortem observations are conducted.

2.3 Experimental procedure

The thermo mechanical characterization is conducted by carrying out conventional tension- compression tests at various strain rates and temperatures.

Table 2. 1 shows the typical range of strain rates and the corresponding testing machines. These works only focus on strain rates from 10^{-3} s^{-1} to 10^4 s^{-1} . Each test was carried out twice and if the results are not consistent then third and fourth test are considered.

We are here distinguishing the tests in terms of

- loading case: tension, compression, shear-compression
- strain rate: low and high strain rates
- temperature: room and high temperature

2..3.1 Loading cases

Several specimens were used based on the type of the tests. Flat type tension specimen was used for quasi static tension test and stress relaxation test. Flat type tension specimen

with notch was also used for quasi static tension test to study the effect of stress triaxiality. Cylindrical type specimen was used for quasi static compression and dynamic compression test. Flat Hat shape specimens were used for quasi static and dynamic shear compression test.

Table 2. 1 The range of strain rates and the corresponding testing machines

Range of strain rate, $\dot{\epsilon}$ (s^{-1})	Speed	Testing machine
10^{-5} to $10^{-1} s^{-1}$	Low speed	Electromechanical or servo-hydraulic
10^{-1} to $10^2 s^{-1}$	Intermediate speed	Special servo-hydraulic
10^2 to $10^4 s^{-1}$	High speed	Split Hopkinson pressure bars
10^4 to $10^6 s^{-1}$	Very high speed	Gas launcher
$> 10^6 s^{-1}$	Ballistic	Explosion

2.3.1.1 Tension

Monotonic Tension test is useful to identify the Young’s modulus, and to study strain hardening and damage effect as well as fracture conditions under various positive stress triaxialities. Relaxation tests are useful to distinguish the rate independent and viscous contributions to the yield stress.

Notched tension specimen was used in this work to study the effect of the stress triaxiality on fracture. The following equation gives the expression of the stress triaxiality (STR) in the necked cross section of the cylindrical specimen according to Bridgman analytical results [25], see (2.1). Fig. 2. 2 shows the sketch for Bridgman equation.

$$\eta = \frac{1}{3} + \ln \left(1 + \frac{a^2 - r^2}{2aR} \right) \tag{2.1}$$

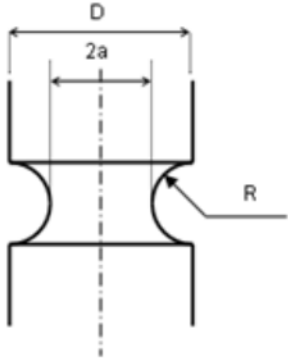


Fig. 2. 2 Cylindrical shape specimen

The maximum STR at the centre of the necked cross section of a cylindrical specimen according the Bridgman analytical results is given by

$$\eta_{\max} = \eta(r=0) = \frac{1}{3} + \ln\left(1 + \frac{a}{2R}\right) \tag{2.2}$$

Yuanli Bai [26] et al had derived the equation which gives the expression of the STR at the centre of the necked cross section of flat specimen by using numerical simulation. Fig. 2. 3 shows evolution of STR as a function of a/R for (2.3). Fig. 2. 4 shows the plane strain specimen [19] for the (2.3).

$$\eta_{\max} = \frac{1}{3} + \sqrt{2} \ln\left(1 + \frac{a}{2R}\right) \tag{2.3}$$

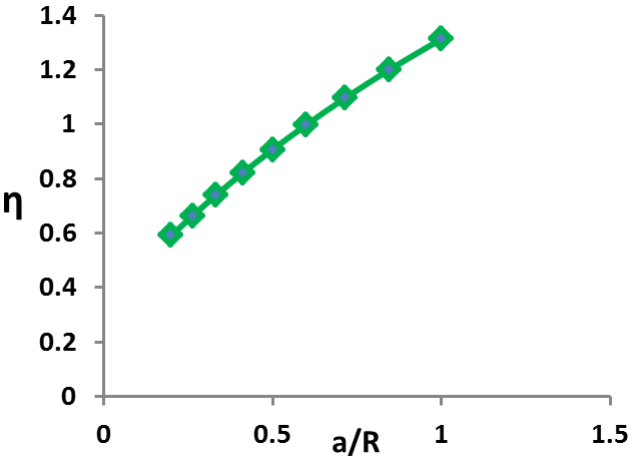


Fig. 2. 3 Evolution of STR as a function of a/R

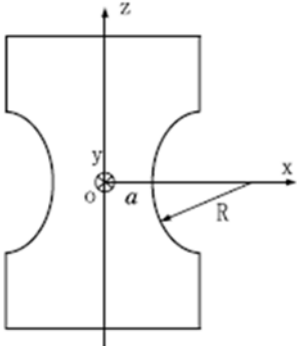


Fig. 2. 4 Plane strain specimen [19]

By applying (2.3), the stress triaxiality can be estimated for flat type notch specimen. Fig. 2. 5 shows the tension specimen used for this test. The specimens were cut along the machine rolling direction of the raw sheet. The specimen is flat type and has a rectangular uniform cross section. Fig. 2. 6 shows sample specimen with different sizes of notch. Size of notch and its corresponding maximum stress triaxiality ratio is given in Table 2.2

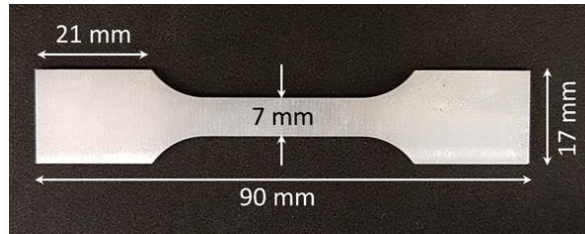


Fig. 2. 5 Quasi static tension smooth specimen. Thickness=2.5 mm

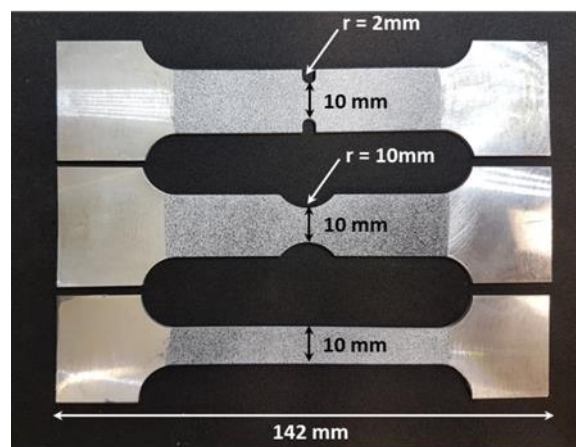


Fig. 2. 6 Quasi static tension smooth and notched specimens. Thickness=2 mm

2.3.1.2 Compression

Compression test, in addition to tension test is useful to study potential compression/tension asymmetry and strain hardening over a strain range wider than the one for tension – experimental results under tension loading are indeed limited to necking onset whereas experimental results under compression loading are limited to barrel effect which generally occurs late in the deformation process.

Fig. 2. 7 show the compression specimen used for this test. The specimen has a diameter of 4.68 mm and height of 5.43 mm.

2.3.1.3 Shear-compression

Shear-compression is useful to study strain hardening and damage effect as well as fracture conditions under (quasi) null and various negative stress triaxialities

In order to identify the shear effect, hat shape specimen was used. Fig. 2. 8 shows two different types of specimen that are designated here in this test as Meyer in reference to [27], see Fig. 2. 8(a) and Couque in reference to [28], see Fig. 2. 8(b). Meyer type specimen is designed in-line with line of compression pressure force where the stress triaxiality ratios are

close to zero. On the other hand the Couque type specimen is inclined with line of compression pressure force where the value for stress triaxiality ratio is negative. This design also can allow shear failure mechanisms to be observed.

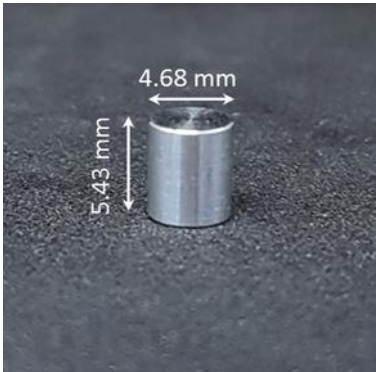


Fig. 2. 7 Quasi static and dynamic compression specimen

In Fig. 2. 8, this is not exactly the original geometry of the hat shape specimens which was cylindrical. In the present work, due to the thickness of the plate the samples are extracted from, it was not possible to machine such cylindrical hat shape specimens. To avoid premature outward bending of the flat hat shape specimen legs involving tension in the shear zone, the legs are constrained by a band of material. This prevents legs from outward bending and ensures a state of shear + pressure (i.e. negative stress triaxiality) in the shear region. This geometry has been designed via numerical simulation using the engineering finite element computation code Abaqus.

Following Table 2. 2 summarizes the expected maximum stress triaxiality values corresponding to the various loading cases studied in the present work. These values are susceptible to evolve all along the deformation process and particularly near the fracture.

Table 2. 2 Expected maximum stress triaxiality values

Loading case	HSS Couque	Compression	HSS Meyer	Smooth tension	R10 tension	R2 tension
Expected stress triaxiality	-0.5	-1/3	-0.2	+1/3	+0.475	+0.572

2.3.2 Low strain rate (Quasi static test)

Low strain rate tests were conducted for tension, compression and shear compression to study the strain rate, temperature and stress triaxiality effects. Two different strain rates were applied on both tension and compression test in quasi static range.

Stress relaxation tests were also carried out in the quasi static range for both tension and compression. The detail about the test condition will be discussed in sub section 2.3.2.2

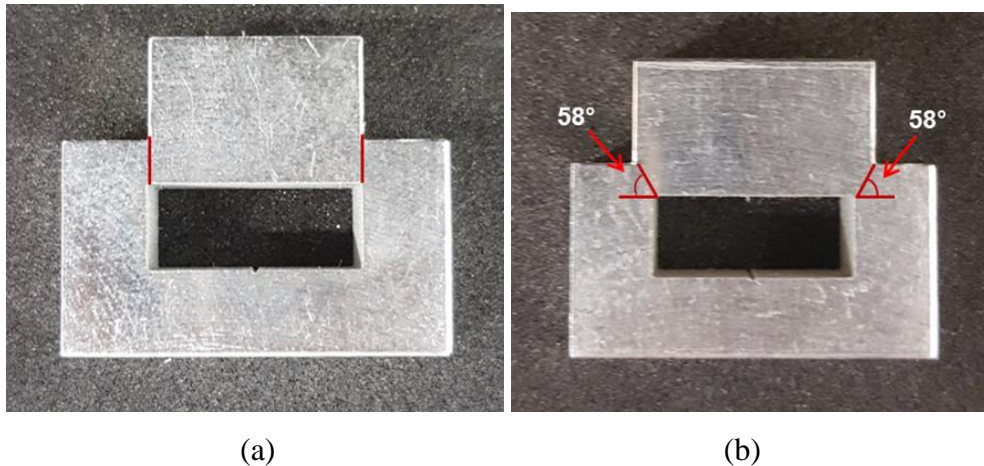


Fig. 2. 8 Quasi static and dynamic shear-compression specimens (a) Meyer and (b) Couque type specimen. The red line indicates the zone of intense shearing. Thickness= 6 mm

2.3.2.1 Experimental set-ups

Experimental set-ups concerning the machines that will be used, along with the displacement and temperature measuring system are discussed below.

- **Quasi static tension tests**

Fig. 2. 9 shows the quasi static tension test set-up. Quasi static monotonic and relaxation tension test was conducted by using Instron 8862, electromechanical universal testing machine with load cell of 100 kN.

Instron mechanical extensometer was used to measure the displacement of the specimen during the test. The temperature range for the extensometer is -80°C to 200°C .

Mechanical extensometer was calibrated before attaching to the specimen. The load and strain limit was set for the extensometer. The extensometer was attached in the centre of the tensile specimen, where the fracture is expected to occur.

The furnace was used to heat the specimens to the required temperature before proceeding with the test. Water was used as cooling fluid to prevent the high temperature from damaging the load cell.

Quasi static tension test is carried out at ambient and elevated temperature Fig. 2. 10 shows the experimental set-up for the quasi static tension test at elevated temperature. The same configuration as quasi static tension at room temperature test was applied for quasi static tension test at elevated temperature.

Apart from normal conventional method by using mechanical extensometer to measure the deformation, digital image correlation (DIC) method was also used to determine the displacement field of the specimen. The specimen is prepared by spraying with white paint and later with black dots, so that the relative movement of the dots can be recorded by using high definition camera. The recorded images were analyzed by using VIC 2D software.

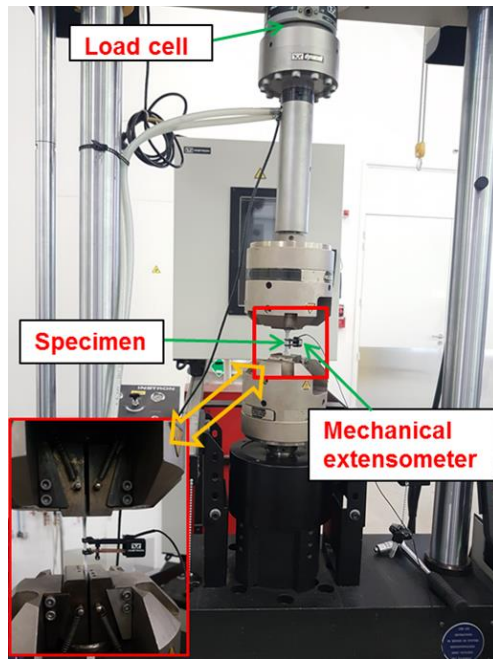


Fig. 2. 9 Quasi static tension test set-up at room temperature

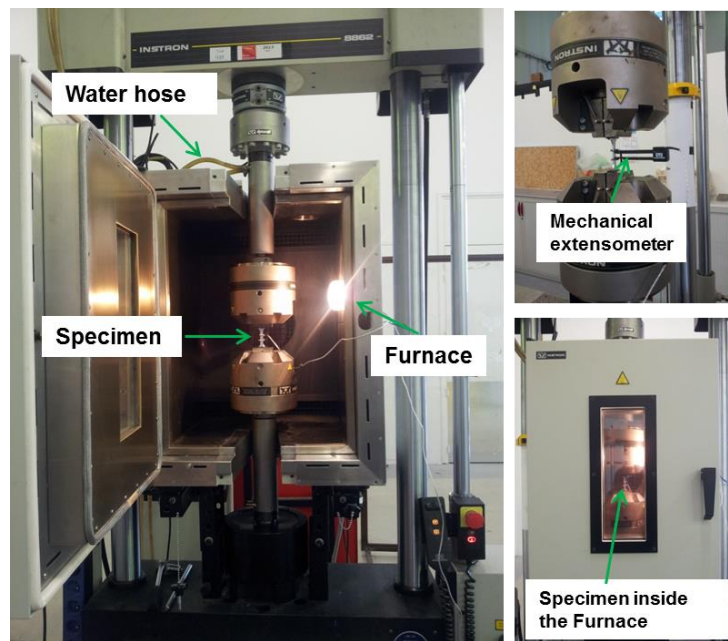


Fig. 2. 10 Quasi static tension test set-up at elevated temperature

- *Quasi static compression test*

Fig. 2. 11 shows the quasi static compression test set-up. The test was carried out by using Instron 8862, electromechanical universal testing machine with load cell of 100 kN. For this test, the specimen used was too small and therefore the extensometer was not able to be fit on the specimen. So as an alternative for the usage of the mechanical extensometer, the specimen deformation was done by determining the total displacement minus the machine

displacement. The measurement details are discussed in the subsection of 2.3.2.3. It is to be noted that this test is conducted only at ambient temperature.

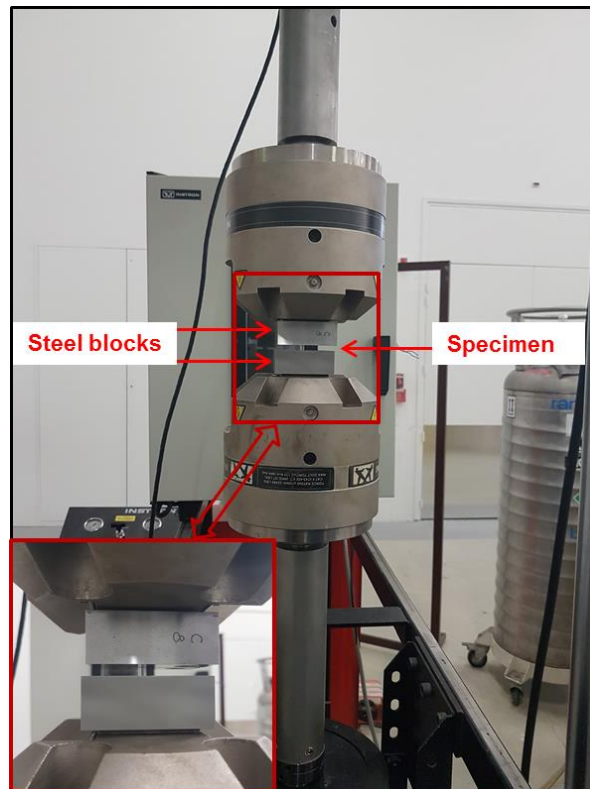


Fig. 2. 11 Quasi static compression test set-up at room temperature

- ***Quasi static shear compression test***

Quasi static shear compression test was done by using Instron universal testing machine with load cell of 10 kN. Fig. 2. 12 shows the experimental set-up for quasi static shear compression test. Specimen was placed between two flat steel blocks in order to perform at the same compression force uniformly along the top of the specimen. Digital image correlation (DIC) method was used to determine the displacement of the specimen. The specimen preparation is same as that of the tension test, where white paint is used as first layer before applying the black spray on it. The recorded images were analyzed by using VIC 2D software.

2.3.2.2 Experimental conditions

In this section the experimental condition will consider under monotonic loading/unloading with different strain rate and temperature range.

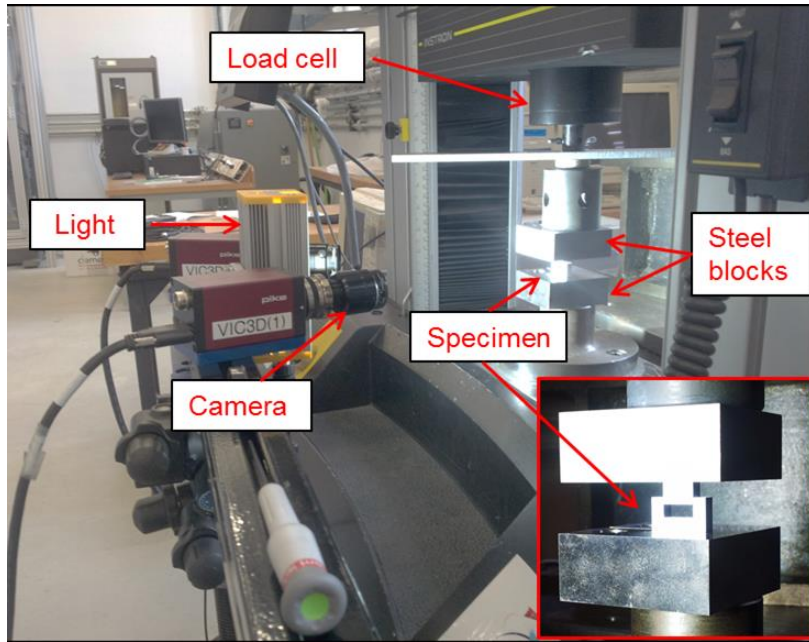


Fig. 2. 12 Quasi static shear-compression test set-up at room temperature

- *Strain rate in quasi static range*

Different tension and compression speeds were applied in order to obtain different strain rates in quasi static ranges. The speeds and their corresponding strain rates are shown in Table 2.3 -2.5.

- Monotonic test

The monotonic tension and compression tests were carried out for two different strain rates in order to characterize the rate sensitivity in quasi static conditions. The test was conducted at ambient temperature. Table 2. 3 and Table 2. 4 show the tension and compression speeds respectively with their corresponding strain rates. It is to be noted that this strain rate is not proportional to the applied machine speed.

Table 2. 3 Tension speeds and their corresponding strain rates

Speed (mm/min)	Strain rate (s^{-1})
1.8	10^{-3}
180	10^{-1}

Table 2. 4 Compression speeds and their corresponding strain rates

Compression speed (mm/min)	Strain rate (s^{-1})
1.8	10^{-2}
180	36

Different velocities were imposed in order to obtain appropriate strain rate values. Tension speed of 1.8 mm/min was applied in order to obtain strain rate of 10^{-3} s^{-1} and speed of 180 mm/min was applied to obtain 10^{-1} s^{-1} . Intermediate speed is not considered because the post processing of the experimental results shows no significant rate sensitivity for both alloys in quasi static range. For compression test, same speeds as the tension test were applied but the strain rate is varying. The strain rate was 10^{-2} s^{-1} and 36 s^{-1} for compression velocity of 1.8 mm/min and 180 mm/min for both alloys.

- Relaxation test

The relaxation test was done for both tension and compression. In this test a constant velocity was maintained over time where the material will experience a certain amount of strain. Then the velocity is set to zero over a time period leading to stress release. This procedure will be repeated several times. Table 2. 5 shows the speeds and corresponding strain rates for stress relaxation test.

Table 2. 5 Speeds and appropriate strain rate for stress relaxation test

Test	Speed (mm min ⁻¹)	Strain rate (s ⁻¹)
Tension	10	6×10^{-3}
Compression	0.18	7×10^{-4}
	0.5	10^{-3}

Fig. 2. 13(a) and Fig. 2. 13(b) shows the velocity and force evolution for the relaxation test at quasi static tension loading. Test velocity is about 0.18 mm/min and reaches maximum force of about 8.1kN.

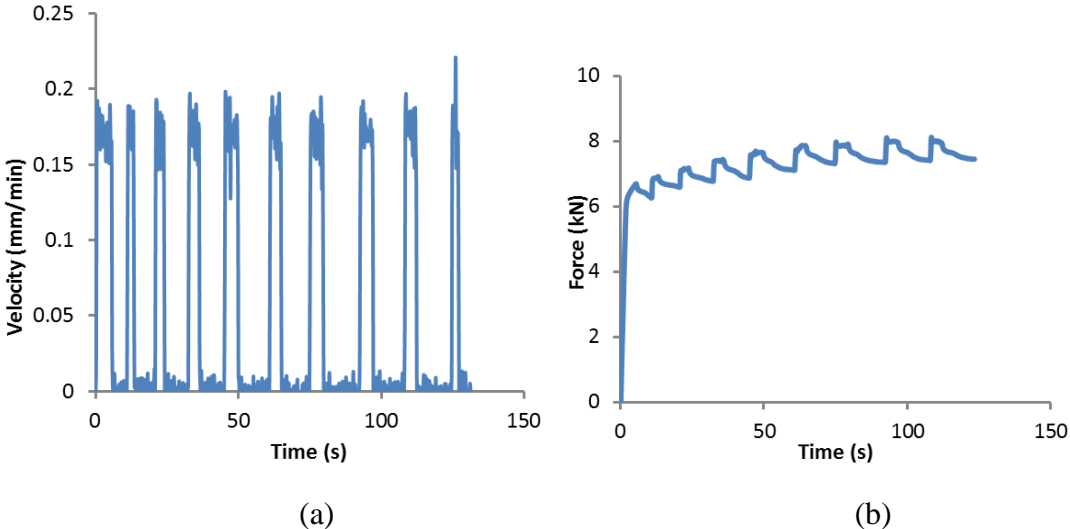


Fig. 2. 13 Tension stress relaxation test results for AA2024 (a) Velocity evolution (b) Force evolution

Fig. 2. 14 shows the true stress vs plastic strain for quasi static tension loading. Relaxation test results is shown in blue curve. Red curve represents the non-viscous plus viscous part of the material and the green curve represents the non-viscous part of the material. This relationship allows us to deduce the viscous part of the material.

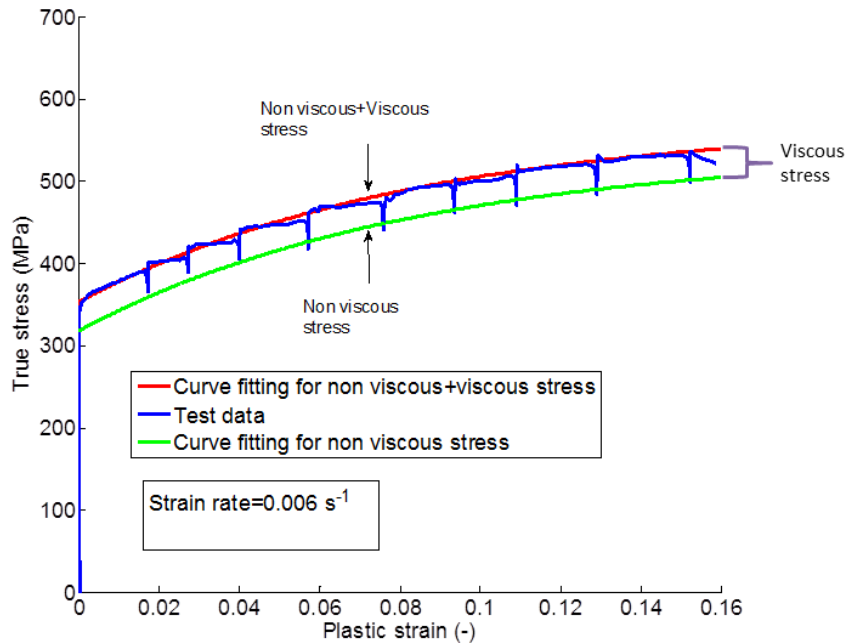


Fig. 2. 14 True stress vs plastic strain for relaxation tension test shows viscous stress

- **Temperature in quasi static range**

To study the effect of the temperature on both alloys, tension test was conducted at various temperature values. The speed was maintained constant but the temperature was varied. Tests were carried out at 30°C, 100°C, 150°C and 200°C. Built-in furnace was used to do the test at elevated temperature, see Fig. 2. 10. For quasi static tension test set-up at elevated temperature, the specimen was placed inside the furnace and heated for 30 minutes at required temperature. This is to allow the specimen to reach thermal equilibrium. Test was conducted until specimen was ruptured. Mechanical extensometer with 25 mm gauge length was fitted on specimen to measure specimen’s elongation. Flat type tension specimen was used in this test, see Fig. 2. 5

2.3.2.3 Post processing of experimental data (Low strain rate)

The post processing of the experimental data was performed by using Microsoft excel. Data acquisition will provide the information of the time and force. Deformation of the specimen is provided by mechanical extensometer or/and digital image correlation. The principle of the computation starts from load versus displacement then stress versus strain, then true stress versus true strain, then equivalent stress vs equivalent plastic strain.

- *Quasi static tension test*

Stress-strain and Young's modulus measurement for uniaxial tension test

Raw data from machine provided by data acquisition system were time and force. Load cell of 100 kN was used for this test. Extensometer provides the displacement measurement of the specimen. Frequency for data acquisition system for quasi static tension test is 5 Hz thus the data will be recorded every 0.2s. First step is to compute the engineering stress, by applying formula,

$$\sigma(Pa) = \frac{F(N)}{A(m^2)} \quad (2.4)$$

Where, σ =engineering stress, F=force, A= initial cross section area of the specimen.

Then engineering strain will be computed based on the initial gauge length over elongation, as given by following equation,

$$\varepsilon = \frac{\Delta l(m)}{l_0(m)} \quad (2.5)$$

Where, ε =engineering strain, l_0 =Initial gauge length, Δl =elongation

The next step is to compute true stress by applying the equation

$$\sigma_T(Pa) = \sigma(Pa)(1 + \varepsilon) \quad (2.6)$$

Where σ_T =True stress, ε =Engineering strain *which is expressed in (2.5)*

Then equivalent stress is computed by applying equation

$$\sigma_{eq} = \sqrt{\frac{3}{2} \underline{\underline{s}} : \underline{\underline{s}}} = |\sigma_T| \quad (2.7)$$

where $\underline{\underline{s}}$ is deviatoric part of the stress tensor $\underline{\underline{\sigma}}$.

True strain is computed by applying (2.8)

$$\varepsilon_T = \ln(1 + \varepsilon) \quad (2.8)$$

Equivalent strain can be computed by applying equation

$$\varepsilon_{eq} = \sqrt{\frac{3}{2} \underline{\underline{\varepsilon}} : \underline{\underline{\varepsilon}}} = |\varepsilon_T| \quad (2.9)$$

Young's modulus was computed by measuring the ratio of the engineering stress over engineering strain in the elastic region, i.e. $E = \Delta \sigma_T / \Delta \varepsilon_T$. This value is the slope of the stress strain curve at elastic part, which is linear. Finally the plastic strain can be computed by removing the elastic part of the flow curve. Then the curve for equivalent stress versus equivalent plastic strain was obtained.

$$\varepsilon_{eq}^p = \varepsilon_{eq} - \frac{\sigma_{eq}}{E} \quad (2.10)$$

Stress-strain measurement for tension on notched specimens, digital image correlation method was used. VIC 2D software was used for post-processing the images that were recorded during the test. The software provides information of the specimen displacements. Virtual extensometer was used to determine the deformation at intended location of the specimen, see Fig. 2. 15. It is to be noted that for tension test on notch specimen the computation only considers up to engineering stress and engineering strain.

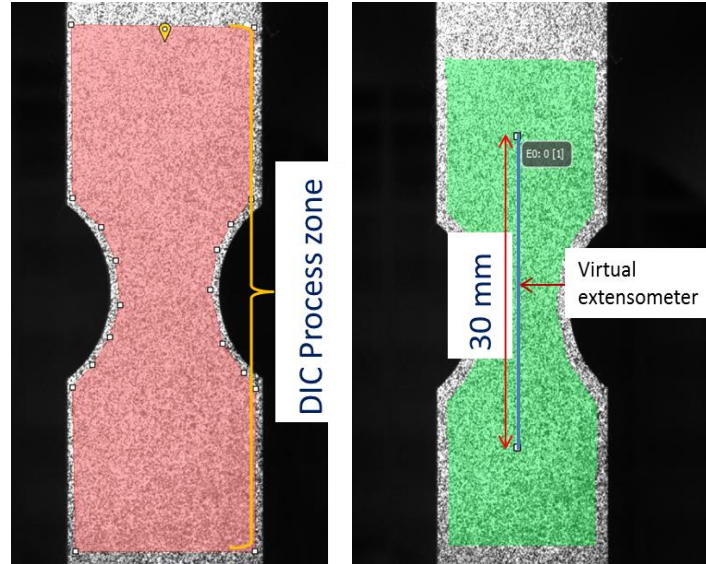


Fig. 2. 15 DIC method shows the process zone and virtual extensometer

- *Quasi static compression test*

Quasi static compression test was carried out at two different speeds, which are 1.8 mm/min and 180 mm/min. Frequencies for data acquisition were 5Hz and 100 Hz for 1.8 mm/min and 180 mm/min respectively. Since the specimen is too small, extensometer could not be fixed into it. So, the total displacement of the specimen was calculated based on total displacement (machine displacement plus specimen displacement) minus machine displacement. In order to calculate the machine displacement, compression test was done without specimen using two steel blocks. The steel block was compressed up to 20 kN and the acquisition data was recorded. Then the test was done using the specimen and compressed by using same steel blocks.

Finally the value for specimen displacement can be calculated by using relationship as shown in (2.11).

$$u_T(F) = u_s(F) + u_M(F) \quad (2.11)$$

Where,

u_T is total displacement, u_s is specimen displacement and u_M is machine displacement.

$u_T(F)$ will be provided directly by machine data acquisition system whereas for $u_M(F)$, the data acquisition provides the compression without specimen as a function of force and given by (2.12).

$$u_M(F) = -4(10^{-9})F^6 + 4(10^{-7})F^5 - 2(10^{-5})F^4 + 3(10^{-4})F^3 - 2.9(10^{-3})F^2 + 2.08(10^{-2})F + 5.3(10^{-3}) \quad (2.12)$$

By applying this relationship, the displacement of the specimen can be computed.

The rest of the calculations are the same as for quasi static tension test by applying equations that was discussed earlier in this sub-section to determine the engineering stress, true stress, equivalent stress, engineering strain, true strain, equivalent strain and plastic strain.

To be noted that initial gauge length, ℓ_0 for quasi static compression specimen is the length of the specimen itself.

Apparent modulus was computed by measuring the ratio of the engineering stress over engineering strain.

- **Quasi static shear-compression test**

Quasi static shear compression test was carried out on modified Meyer and Couque hat shaped specimens (see Fig.2.12) by using digital image correlation method. VIC 2D software was used to do further post processing.

Data acquisition system from machine provides information for force and time. The stress could not be computed due to complexity of the cross section area.

Vertical displacement of the specimen can be computed based on DIC method, which is provided by post processing using VIC 2D software.

Force evolution curve was plotted for this test. The rest of the curve ie, stress versus strain and true stress versus true strain not able to plot due to unknown cross section area of the specimen.

2.3.3 High strain rate (Dynamic test)

High strain rate tests were carried out for compression tests by using Split Hopkinson pressure bar (SHPB) apparatus. SHPB method to investigate the material behavior is proposed by Kolsky [29] and it became a well-established method to characterize the materials under strain rate of the order of 10^3 s^{-1} .

2.3.3.1 Experimental set-up

Split Hopkinson pressure bar (SHPB) was used to perform dynamic compression test in order to characterize a potential high strain rate effect within range of 10^3 s^{-1} to 10^4 s^{-1} . This apparatus consists of three bars which are striker bar, input bar and output bar. Pressure from compressed air will be used to move the striker bar and impact an input bar. Specimen will be placed in between input bar and output bar. Due to transverse expansion of the specimen during loading frictional constraint exist at bar-specimen interface where it can be reduced by using grease as a lubricator [30]. Length of striker bar is 0.3m, length of input bar is 3m and length of output bar is 2m. These bars are made by stainless steel with diameter of 20 mm. Speed measurement of the striker bar is done using photodiode and emitter which placed about 50 mm from the input bar end. When the striker bar passed through the photodiode, the

changes in electric signal will be detected by the data acquisition system and used to determine the striker bar velocity. Table 2. 6 shows the dimension and material properties of SHPB used in this study.

Table 2. 6 Dimension and properties of SHPB at ICA laboratory

Length of striker bar	0.3 m
Length of input bar	3.0 m
Length of output bar	2.0 m
Diameter of bars	0.02 m
Young's modulus of bars	205 GPa
Poisson's coefficient	0.3

When striker bar impacted the input bar, elastic compressive wave will be generated inside the input bar. The magnitude of the pulse will be influenced by the impact speed and the duration of the pulse by striker length. Stress pulse will be propagating along the incident bar and partly transmitted through specimen to the output bar. Strain gauges will record the strain history and the Wheatstone bridge used to measure the strain in term of electrical signal before recorded by data acquisition system.

In order to measure the deformation of the specimen, several pairs of strain gauges are located on each bar. Strain gauges are attached at distance of 135 cm from the specimen for input bar and 50 cm from specimen for output bar. Fig. 2. 16 shows the split Hopkinson pressure bar that is available at ICA laboratory.

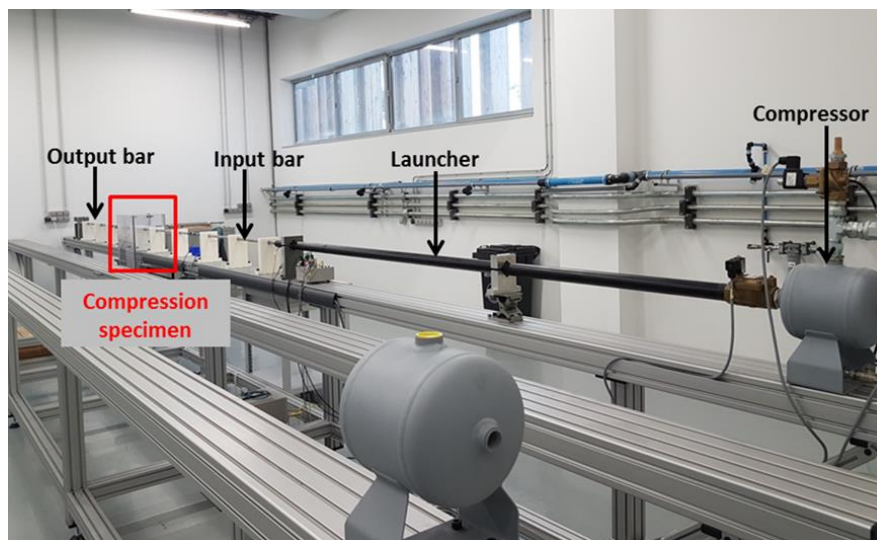


Fig. 2. 16 SHPB apparatus for dynamic compression tests

2.3.3.2 Experimental conditions

Experimental conditions in this sub chapter are considering high strain rate range from 1000 to 4500 s⁻¹. All tests were carried out at room temperature.

- **Dynamic compression test**

Dynamic compression test was conducted at ambient temperature of about 30°C. High speed camera that was used in this experiment is constructed by Photron with the maximum speed of 250,000 frames per second. (128 X 16 pixel). Lighting system provided by two Dedolight HMI with power of 400 W each. Cylindrical shape specimen with diameter of 4.68 mm and length of 5.43 mm was used, see Fig. 2. 7 for quasi static and dynamic compression specimen. Specimen is sandwiched between input and output bars. The specimen dimension is exactly the same with specimen that was used for quasi static compression test. Further information on computing the stress and strain will be explained in the sub chapter 2.3.3.3. Table 2. 7 shows the pressure and their corresponding striker bar velocity during impact.

Table 2. 7 Pressure and striker bar impact velocity

Pressure (Bar)	Striker bar impact velocity (m.s ⁻¹)
1	7.0
2	12.5

- **Dynamic shear compression test**

Dynamic shear compression test was done by using SHPB testing apparatus with the same configurations as for dynamic compression test discussed earlier in section 2.3.3.1. Modified Meyer and Couque type hat shape specimens were used instead of cylindrical type specimen. Fig. 2. 17 shows the hat shape specimen sandwiched in between input and output bars. Extra steel 20 mm-diameter 10 mm-length disks were attached at the specimen/bar interfaces to avoid potential bar indentation. A Pressure of 2 bar provided the striker bar with an impact velocity of 12.5 m.s⁻¹.

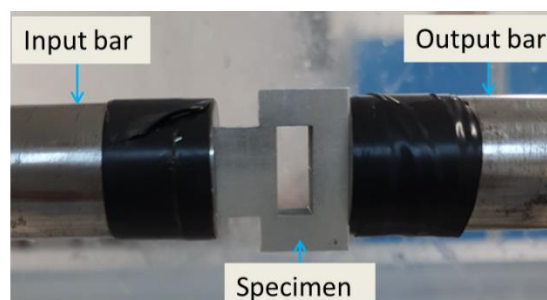


Fig. 2. 17 Hat shape specimen sandwiched between SHPB input and output bars. Hard steel rings are used to avoid bar indentation

2.3.3.3 Post processing of experimental data (High strain rate)

Post processing of the experimental data was performed by using Microsoft excel. Data acquisition will provide the information about the time and strain of the input and output bars. Deformation of the specimen is provided by strain gauges. The principle of the computation starts from time shifting of incident, reflected and transmitted strains for input and output load

equilibrium, then load versus displacement then stress versus strain, then stress versus plastic strain, then equivalent stress vs equivalent plastic strain. This relationship is required for further constitutive modelling.

- ***Dynamic compression (Cylindrical shape specimen)***

Frequency for data acquisition system was 500 kHz thus data will be recorded at every 2 μ s. Two strain gauges that are fixed diametrically opposed on each bar will record the incident and reflected strain pulse on the input bar and transmitted strain pulse on the output bar. The strain value from strain gauges will be recorded by data acquisition system. Based on this strain values, the strain evolutions in the input bar and output bar can be computed. This strain evolution provides information on incident wave, reflected wave and transmitted wave, as mentioned above. The pulses of the stress wave recorded at the both ends of specimen are given by one-dimensional stress wave theory related to particle velocities. The equations are from the book "Split Hopkinson (Kolsky) Bar Design, Testing and Applications" [31].

There are three assumptions made as follows;

- Specimen must be in equilibrium, i.e. input load and output load must be equal
- Velocity continuity between bars and sample
- Stress wave propagation without dispersion

After time shifting, the equations are as follows;

$$\dot{\varepsilon} = -2 \frac{C_B}{\ell_0} \varepsilon_R \quad (2.13)$$

$$\varepsilon = -2 \frac{C_B}{\ell_0} \int_0^t \varepsilon_R dt \quad (2.14)$$

$$\sigma = \frac{A_B}{A} E_B \varepsilon_T \quad (2.15)$$

where, $\dot{\varepsilon}$ = engineering strain rate, C_B = elastic bar wave speed, L_0 = initial length of the specimen, ε_R = reflected strain pulse, A_B = cross section area of the bar

Engineering strain rate is given by (2.13). After computing the engineering strain rate, engineering strain can be computed by applying (2.14). Then true strain and equivalent strain can be computed by applying (2.8) and (2.9) respectively. Then true stress and equivalent stress was computed by applying (2.6) and (2.7) respectively.

Engineering stress versus engineering strain can be plotted, followed by true stress versus true strain. Then equivalent stress versus equivalent strain can be plotted. Finally elastic part is removed from the equivalent stress versus equivalent strain and to obtain the equivalent plastic strain by applying (2.10).

- ***Dynamic shear compression (Hat shape specimen)***

Dynamic shear compression test configurations are similar to dynamic compression test. The only difference is the usage of the hat shape specimen instead of using cylindrical shape specimen. Frequency of 500 kHz was used for data acquisition system. The strain evolution will provide information on incident, reflected and transmitted strain wave. It is to be noted

that for dynamic shear compression test, only force evolution is presented as a result. Because the force is at equilibrium in the specimen, the total axial load on the specimen can be determined from the transmitted wave, ε_T by

$$F_a = A_b E_b \varepsilon_T \quad (2.16)$$

Where, A_b and E_b are cross sectional area and elastic modulus of Hopkinson bar respectively [11].

2.3.3.4 Microscopic observation

Fractography analyses were performed to observe the micro-mechanisms controlling the fracture as a function of the strain rate, temperature and stress triaxiality when possible.

To that purpose, optical microscope, Olympus GX71, and scanning electron microscope (SEM), Philips XL30ESEM, were used to analyze the specimens after impact.

Microscopic analyses of the specimens were carried out using four different methods. First method (M1) consists in observing without grinding, polishing or etching. Second method (M2) consists in observing after grinding by using sand paper with different successive grain sizes. Third method (M3) consists in observing after grinding with sand paper and polishing with diamond particle fluids. Fourth method (M4) consists in grinding with sand paper, polishing with diamond particle fluids and etching the specimen. The specimens were etched during 10 to 15 second by acid consisting of 10% of hydrochloric acid, 10% of nitric acid, 5% of hydrofluoric acid and 75% of water.

Fig. 2. 18 shows the method to remove dynamic shear compression specimen for Couque type specimen which was stuck together after the test. Roller cutter machine was used to cut the specimen in order to observe the microstructure at the fractured region. The specimen was cut by using roller cutter saw. The specimen was cut and the fractured part was separated without damaging the fractured surface.

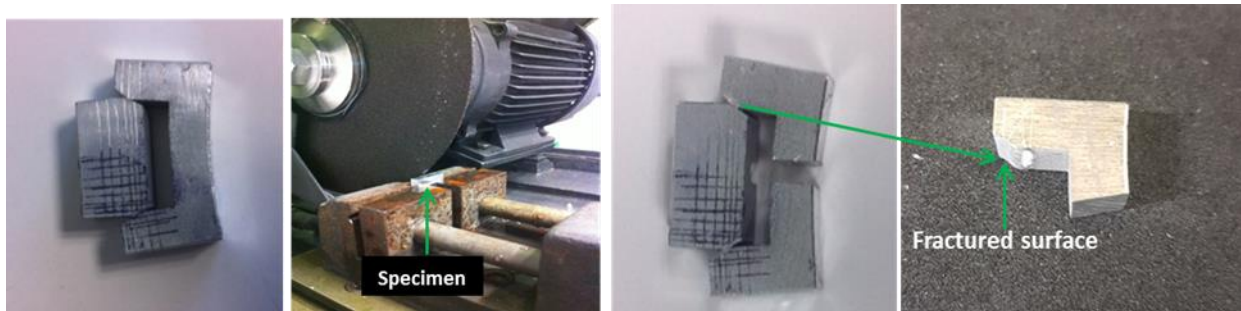


Fig. 2. 18 Specimen cut and separated to observe the fractured surface

2.4 Results and discussion

This section presents the main results obtained from an extensive experimental campaign done on both aluminium alloys over wide strain rate and temperature ranges. The output from the machine as well as mechanical extensometer and DIC system was utilized in order to obtain the stress-strain, force-time relationship for both alloys. The microstructural observations of the specimen done after the tests are discussed.

2.4.1 AA2024

The results obtained for AA2024 aluminium alloy are shown and commented in this section.

2.4.1.1 Response under tension and compression loading

In this section the results of tension and compression will be discussed for both low and high strain rate loading for AA2024.

- *Monotonic loading*
 - Influence of stress triaxiality

In order to study the effect of stress triaxiality, notched specimens were used. The maximum stress triaxiality value is about 0.333, 0.475 and 0.572 for smooth, notch radius of 10 mm and notch radius of 2 mm respectively. Fig. 2. 19 (a) and Fig. 2. 19 (b) show the engineering stress versus engineering strain for tensile test with notched specimens at ambient temperature and at 200°C respectively.

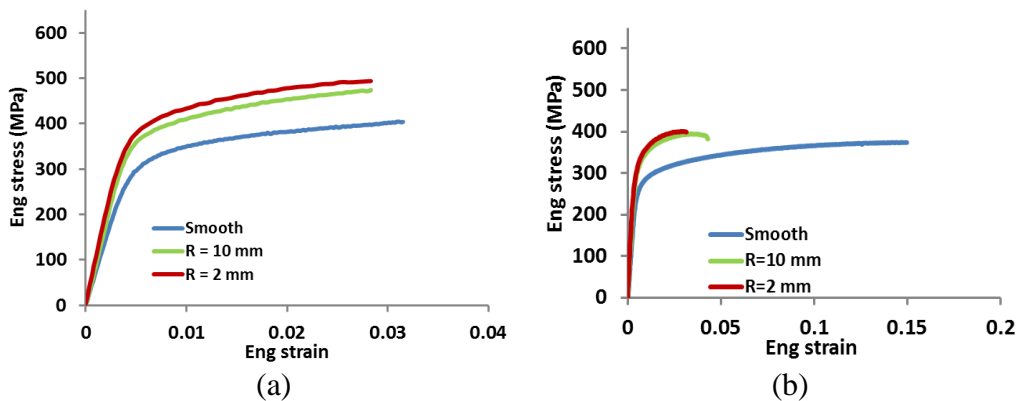


Fig. 2. 19 Engineering stress vs engineering strain on AA2024 notched specimen for quasi static tension loading (a) Ambient temperature (b) 200°C

The initial stress, (Initial stress here is where the curve shows the inelastic behavior), is higher for notch radius of 2 mm at about 390 MPa. The initial stress is about 369 MPa and 330 MPa for notch radius of 10 mm and smooth specimen respectively. At temperature of 200°C the initial stress is 325 MPa, 315 MPa and 295 MPa for notch radius of 2 mm, 10 mm and smooth specimen respectively. The maximum stress and the strain at fracture is given in the Table 2. 8 and Table 2. 9 for ambient temperature and 200°C respectively. Strain for notch specimen is calculated by using the VIC 2D software which is used as a post processing tool for DIC method. The virtual extensometer is embedded in the software and allows us to apply it on the speckle image for measure the strain, see Fig. 2. 15.

Table 2. 8 Stress triaxiality influence on stress and strain at fracture at room temperature

<i>Geometry</i>	<i>Stress triaxiality</i>	<i>Initial stress (MPa)</i>	<i>Max stress (MPa)</i>	<i>Strain at fracture</i>
<i>Smooth</i>	<i>1/3</i>	<i>320</i>	<i>426</i>	<i>0.04</i>
<i>R10</i>	<i>0.475</i>	<i>369</i>	<i>459</i>	<i>0.025</i>
<i>R2</i>	<i>0.572</i>	<i>390</i>	<i>487</i>	<i>0.02</i>

Table 2. 9 Stress triaxiality influence on stress and strain at fracture at 200°C

<i>Geometry</i>	<i>Stress triaxiality</i>	<i>Initial stress (MPa)</i>	<i>Max stress (MPa)</i>	<i>Strain at fracture</i>
<i>Smooth</i>	<i>1/3</i>	<i>295</i>	<i>374</i>	<i>0.175</i>
<i>R10</i>	<i>0.475</i>	<i>315</i>	<i>394</i>	<i>0.043</i>
<i>R2</i>	<i>0.572</i>	<i>325</i>	<i>400</i>	<i>0.032</i>

Fig. 2. 20(a) and Fig. 2. 20(b) show the initial yield and maximum engineering stress versus stress triaxiality for room temperature and 200°C. As expected initial yield and maximum engineering stress are increasing with the increases of stress triaxiality for both at room temperature and 200°C. In the same time, strain at failure is decreasing as shown in Fig. 2. 19 and Tables 2.8-2.9.

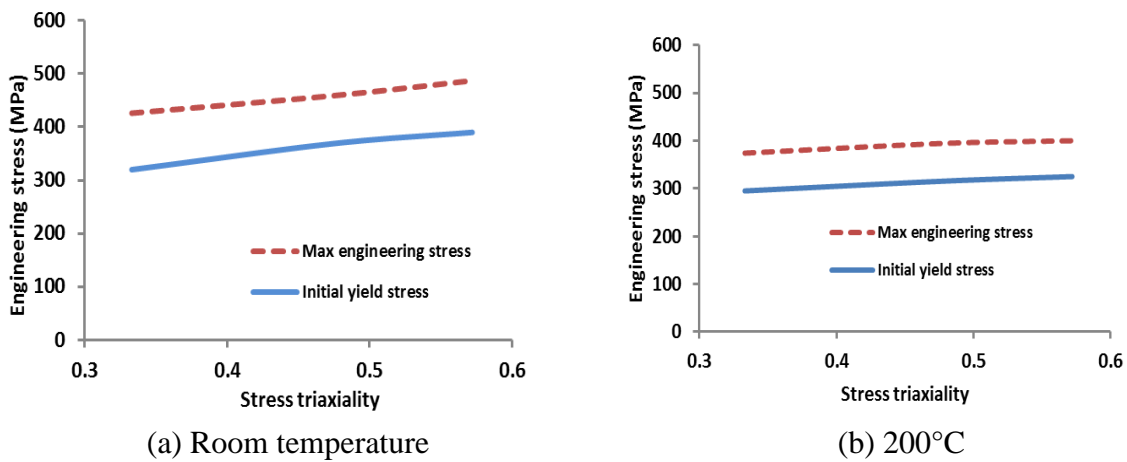


Fig. 2. 20 Engineering stress vs stress triaxiality for initial yields stress and maximum engineering stress for (a) Room temperature (b) 200°C

- Influence of strain rate

Fig. 2. 21(a) and Fig. 2. 21(b) show the different strain rates for tension and compression tests respectively for AA2024. For tension test, strain rates of 10^{-3} and 10^{-1} were superimposed. There is no strain rate effect for AA2024 for the considered quasi static range in tension. Quasi static compression was carried out at two different strain rates which are 10^{-2} and 36 s^{-1} . The results show there is no strain rate effect for this alloy in considered quasi static compression range. Table 2. 10 shows the Young’s modulus, initial yield stress and strain hardening for the corresponding tension and compression test at quasi static range. It is to be noted that the values for strain hardening given in the table are the exponents in Hollomon’s hardening law for a quantitative comparison.

Fig. 2. 22 shows the comparison of quasi static and dynamic compression test. Three different strain rates are considered which are 10^{-2} , 2020 and 4500. The results show that there is slightly strain rate dependence for this alloy especially at higher strain rate. Initial yield stress for quasi static compression is about 340 MPa whereas for dynamic compression is about 360 MPa. Significant strain hardening is visible for both dynamic and quasi static compression up to 0.2 of plastic strain.

Table 2. 10 Strain rate influence on Young's modulus, initial yield stress and strain hardening in quasi static tension and compression loading

AA2024	Strain rate (s ⁻¹)	Young's modulus (GPa)	Initial yield stress (MPa)	Strain hardening
Tension	10 ⁻³	71	360	0.15
	10 ⁻¹	70	370	0.10
Compression	10 ⁻²	irrelevant	340	0.19
	36	irrelevant	300	0.17

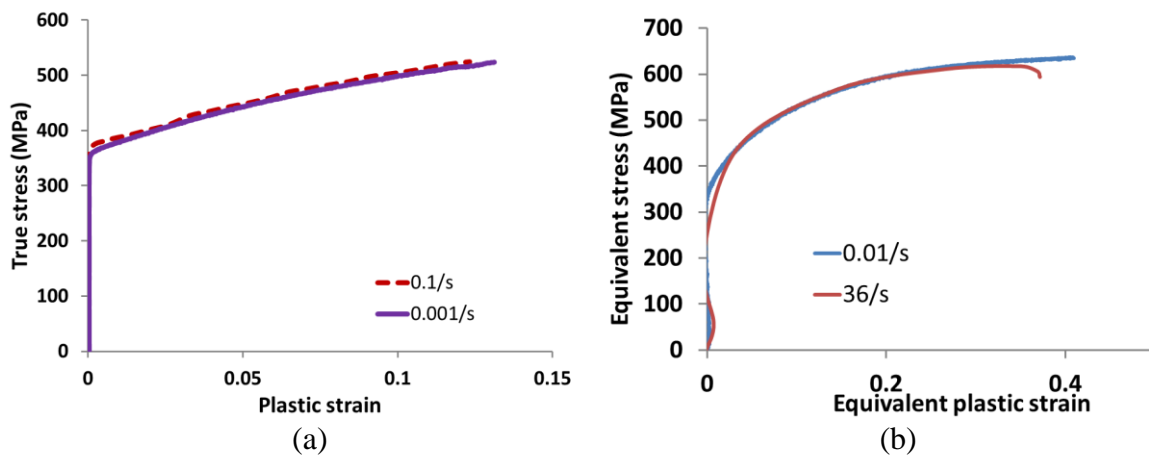


Fig. 2. 21 Flow curve for AA2024 under (a) quasi static tension (b) quasi static compression

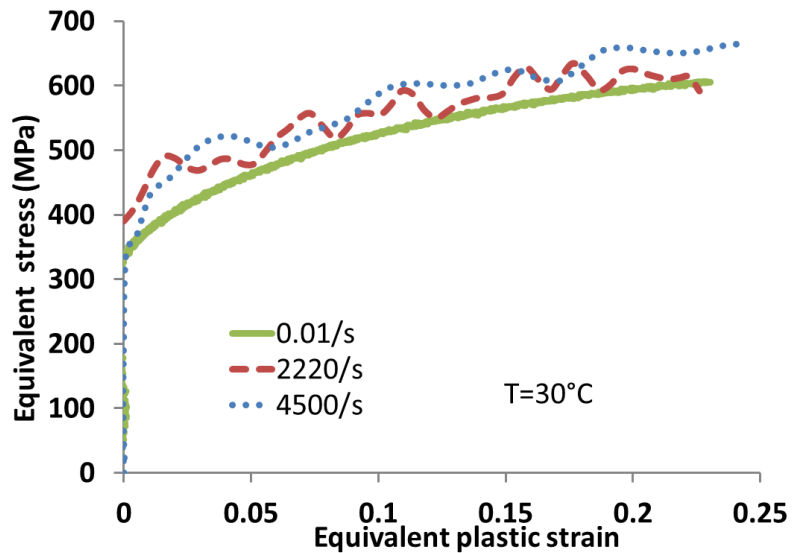


Fig. 2. 22 True stress vs plastic strain for dynamic and quasi static compression for AA2024

Table 2. 11 shows the yield stress at various plastic strains and strain rates.

Table 2. 11 Yield stress at various strain and strain rate

Strain rate (s^{-1})	Plastic strain	0.02	0.04	0.06	0.08	0.1
10^{-2}	Yield stress (MPa)	405	445	478	506	528
2220	Yield stress (MPa)	460	480	500	520	555
4500	Yield stress (MPa)	470	510	520	540	590

Fig. 2. 23 shows the yield stress vs strain rate at different plastic strains. The curve shows that yield stress depends on plastic strain rate.

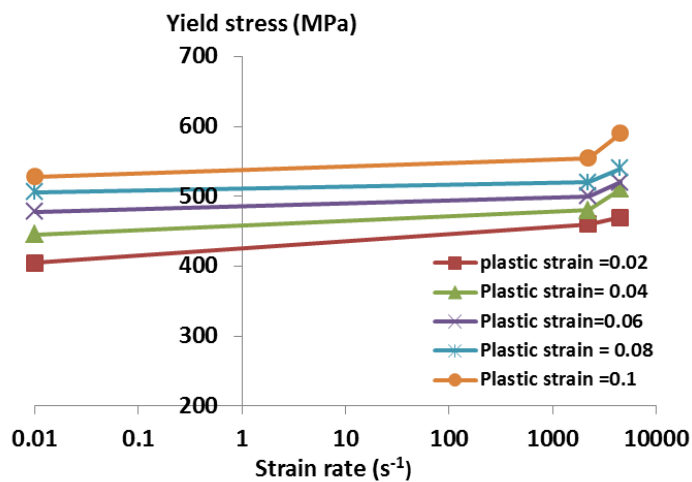


Fig. 2. 23 Yield stress vs strain rate for different plastic strain

- Influence of temperature

Fig. 2. 24 shows a temperature effect on flow curve for AA2024. Tests were carried out from ambient temperature of 30°C to 200°C. The strain rate is constant at $10^{-3} s^{-1}$ for all temperatures. The flow curve shows with the increasing of temperature, initial yield stress is decreasing. Initial yield is 356 MPa, 334 MPa, 308 MPa and 299 MPa for temperature of 30°C, 100°C, 150°C and 200°C respectively. The strain hardening remains quasi unchanged with the increasing of the temperature in the considered range which is up to 200°C.

Table 2. 12 shows the yield stress at various plastic strains and temperatures.

Fig. 2. 25 shows the curve for yield stress vs temperature at different plastic strains. The curve shows that the yield stress significantly depends on temperature. Yield stress is decreasing with the increasing temperature, as expected.

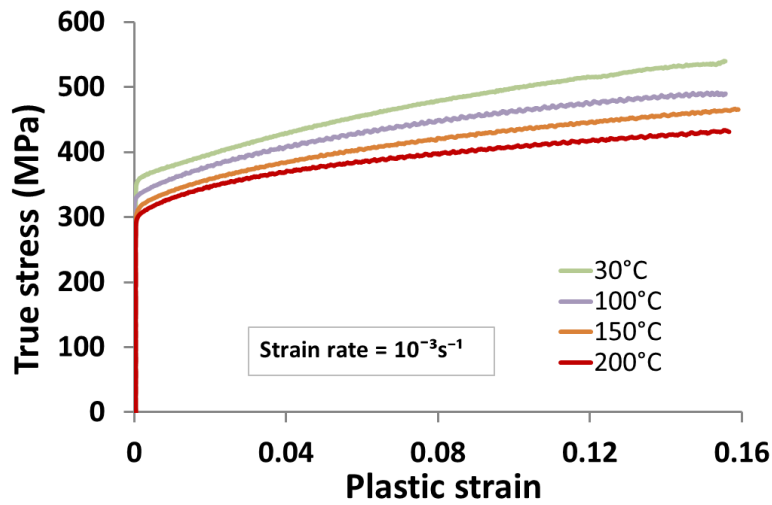


Fig. 2. 24 True stress vs plastic strain for different temperature

Table 2. 12 Yield stress at various strain and temperature

Temperature (°C)	Plastic strain	0.02	0.04	0.06	0.08	0.1
30	Yield stress (MPa)	395	437	463	485	505
100	Yield stress (MPa)	378	406	431	449	464
150	Yield stress (MPa)	360	385	405	420	434
200	Yield stress (MPa)	338	356	374	386	399

Fig. 2. 25 Yield stress vs temperature for different plastic strains

- **Relaxation tests**

Relaxation test results are presented in this section as true stress versus plastic strain.

Fig. 2. 26 (a) and Fig. 2. 26 (b) show the true stress versus plastic strain for tension and compression relaxation test respectively. The results show the viscous stress part for both tension and compression test. Further use concerning this part will be presented in the chapter of analytical modelling.

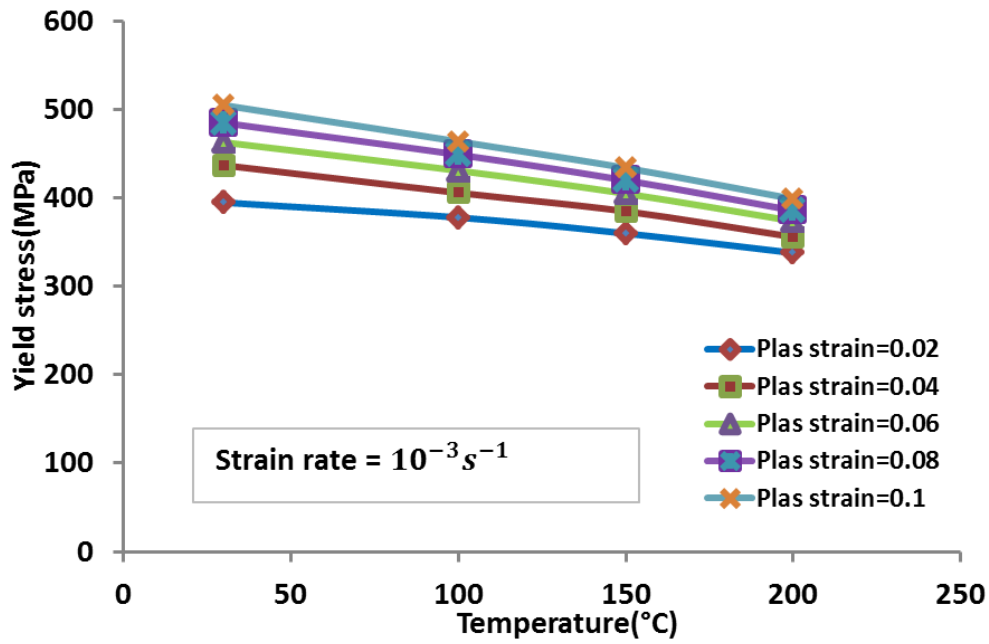


Fig. 2. 25 Yield stress vs temperature for different plastic strains

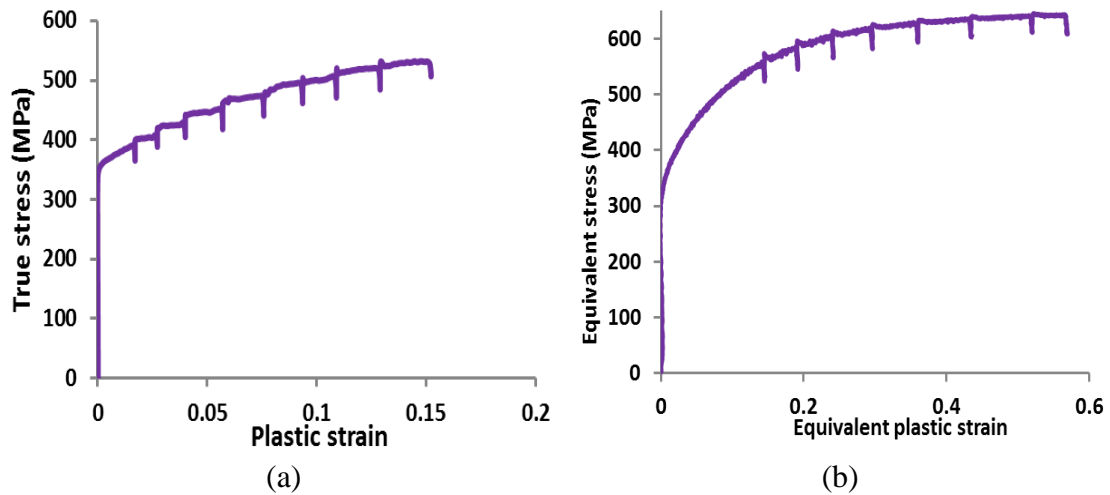


Fig. 2. 26 True stress vs plastic strain for AA2024 under (a) Tension (b) Compression loading

Fig. 2. 27(a) and Fig. 2. 27(b) show the viscous stress vs plastic strain for tension and compression test in quasi static loading. The curve shows that viscous stress is does not depend on plastic strain at the considered strain rate.

Fig. 2. 28 shows the viscous stress vs temperature for quasi static strain rate of $10^{-3} s^{-1}$. The viscous stress is not temperature dependent at this strain rate.

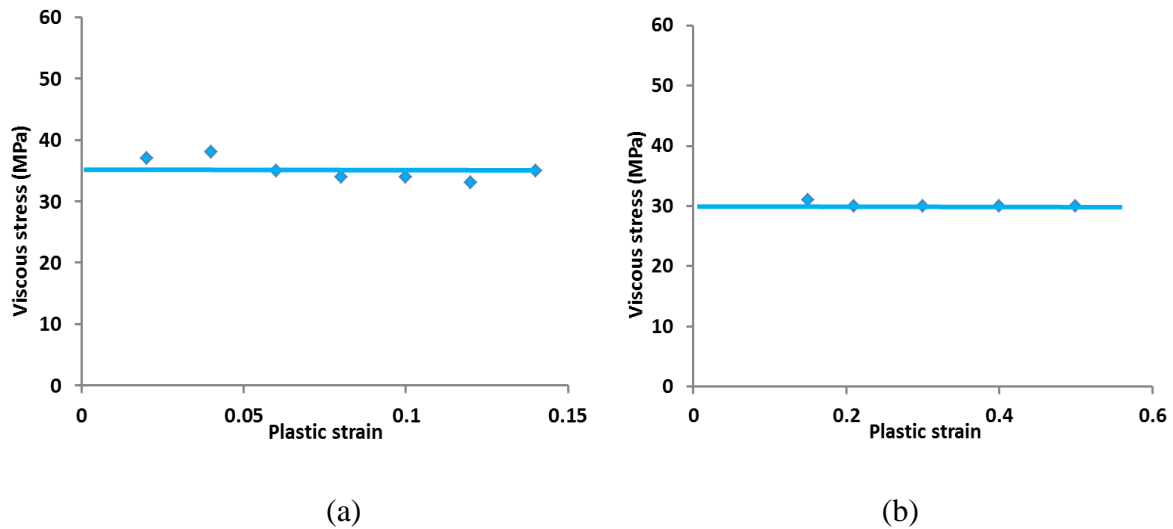


Fig. 2. 27 Viscous stress vs plastic strain

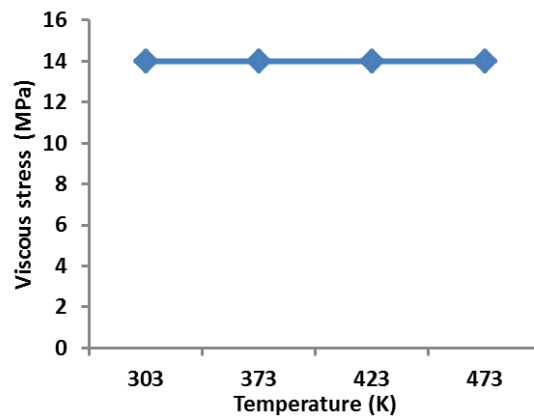


Fig. 2. 28 Viscous stress vs temperature

2.4.1.2 Response under shear-compression loading

- Influence of strain rate

Fig. 2. 29(a) and Fig. 2. 29(b) show force versus time for quasi static and dynamic shear compression respectively for hat shape specimens. Both quasi static and dynamic test show that a larger force was required to deform Couque type specimen. Generally magnitude of force was larger for dynamic compression compared to quasi static compression.

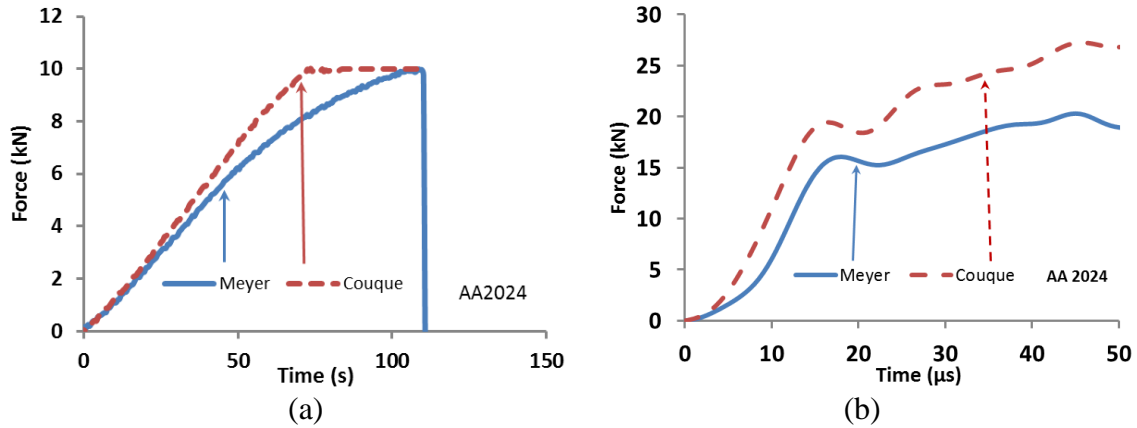


Fig. 2. 29 Force evolution for AA2024 under (a) Quasi static (b) Dynamic shear compression loading

Table 2. 13 shows maximum force at maximum loading time for both shapes under quasi static and dynamic loading. It is to be noted that the quasi static test was conducted by using load cell of 10 kN thus the force does not go beyond this limit.

Table 2. 13 Maximum force for Meyer and Couque shape specimen in quasi static and dynamic compression loading

<i>Strain rate</i>	<i>Geometry</i>	<i>Max force(kN)</i>
<i>Static</i>	<i>Meyer</i>	9.8
	<i>Couque</i>	>10
<i>Dynamic</i>	<i>Meyer</i>	20.3
	<i>Couque</i>	27

2.4.1.3 Fracture analysis

The deformed shape, fractured angle and fractured surface of the specimen will be discussed for AA2024 in this section.

- Influence of stress triaxiality ratio

Fig. 2. 30(a) and Fig. 2. 30(b) show the specimens of the dynamic shear compression after test for Meyer and Couque shape respectively. For Meyer it is fully fractured and compressed up to the edge, see Fig. 2. 30 (a). For the Couque type specimen it is partly fractured and remains stuck together as depicted in Fig. 2. 30 (b). It is to be noted that for Couque type test the specimen has been subject to deflection thus the fractured surface results from a complex loading. This must be taken into account for the microstructural observations. The preparation of the specimens has been achieved by applying method M1.

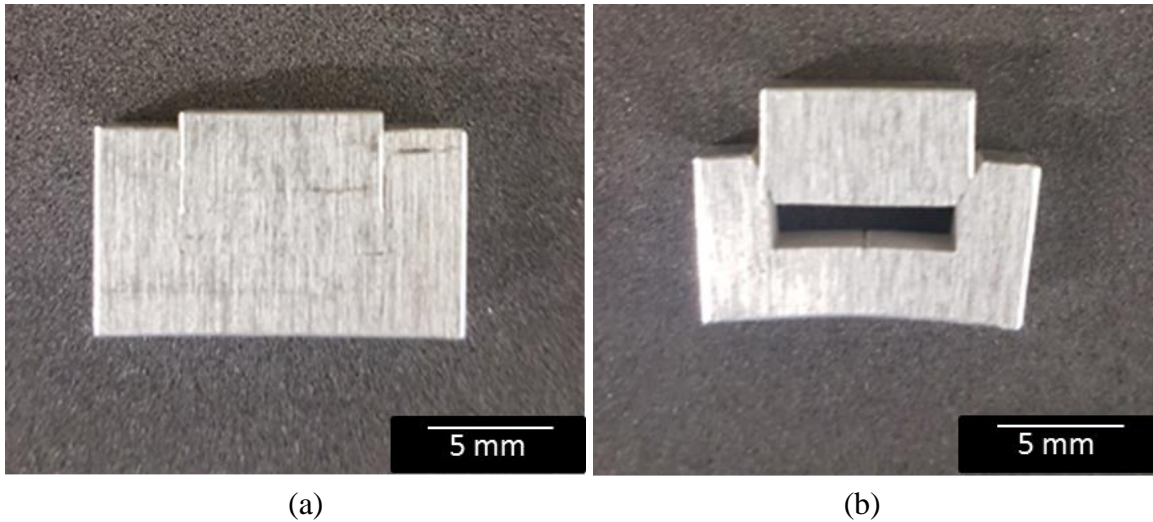


Fig. 2. 30 Specimen after dynamic shear compression test (a) Meyer and (b) Couque

Fig. 2. 31 shows the fractured surface of the Meyer type specimen for AA2024. The region was distinguished into two zones. First zone was the initiation of the fracture and the second zone was the fracture propagation. The microstructure for the both zones shows that the fracture was under shearing induced Mode II, see Fig. 2. 31(c) and Fig. 2. 31(d).

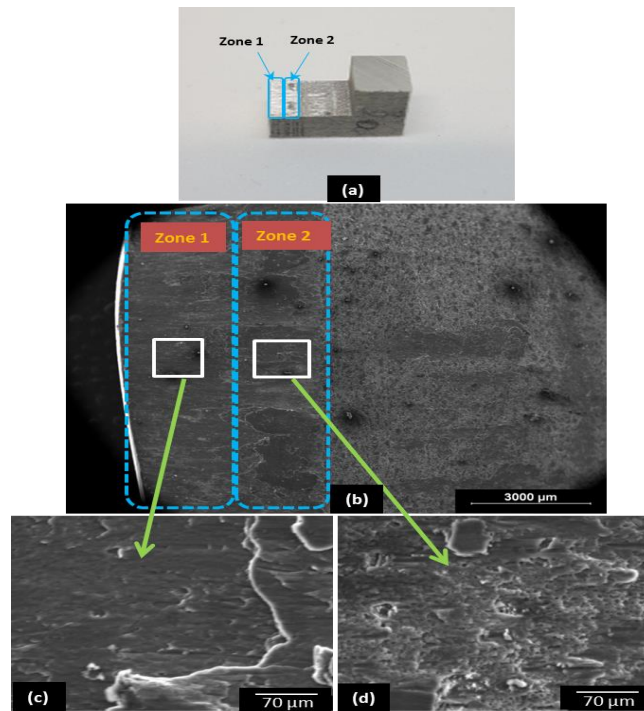


Fig. 2. 31 Meyer type AA2024

Fig. 2. 32 shows the fractured surface of the Couque type specimen for AA2024. The region was distinguished into two zones. First zone was the initiation of the fracture and the second zone was the fracture propagation. The microstructure for the fracture initiation zone shows shearing induced Mode II failure whereas for second region where the fracture arrest was under tension induced Mode I failure, see Fig. 2. 32 (c) and Fig. 2. 32 (d).

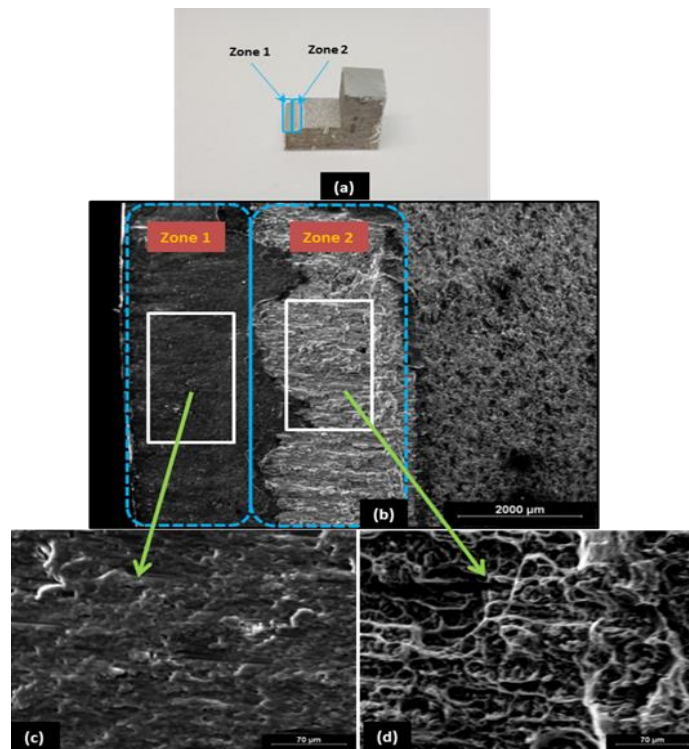


Fig. 2. 32 Couque type AA2024

- Influence of strain rate

Fig. 2. 33 (a) and Fig. 2. 33(b) show the specimen after quasi static compression and dynamic compression respectively for AA2024. Under quasi static loading the specimen remain quasi homogenous whereas under dynamic loading there is slightly barreling effect on specimen despite the lubrication of the specimen sides.

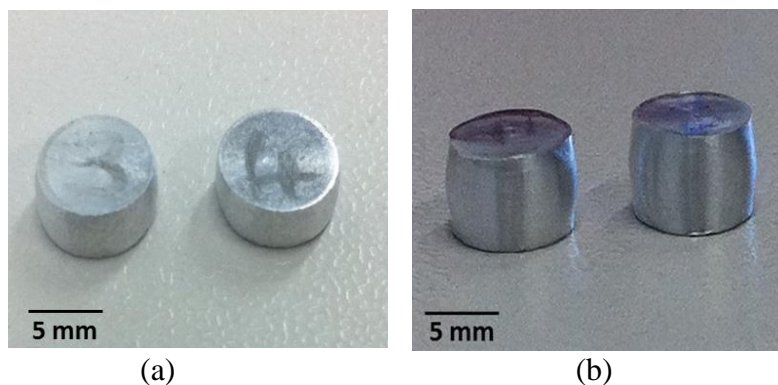
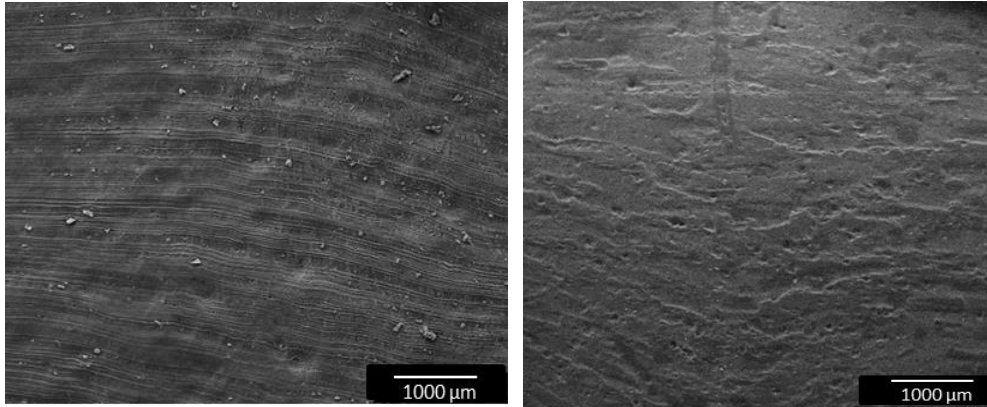


Fig. 2. 33 Specimen of the AA2024 after (a) Quasi static and (b) Dynamic compression

Fig. 2. 34 (a) and Fig. 2. 34 (b) show the microstructure of the specimen after quasi static compression and dynamic compression respectively. The microstructure observation was done by applying method M4, as discussed earlier. Microstructure of AA2024 remains quasi homogenous under both quasi static and dynamic loading.



(a)

(b)

Fig. 2. 34 Microstructure of the AA2024 specimen after (a) Quasi static and (b) Dynamic compression test

Fig. 2. 35 shows the fracture lip zone analysis for Couque shape specimen. The specimen was prepared by applying method M4 and observed under optical microscope. The results show no shear localization for this alloy near fracture lip surface.

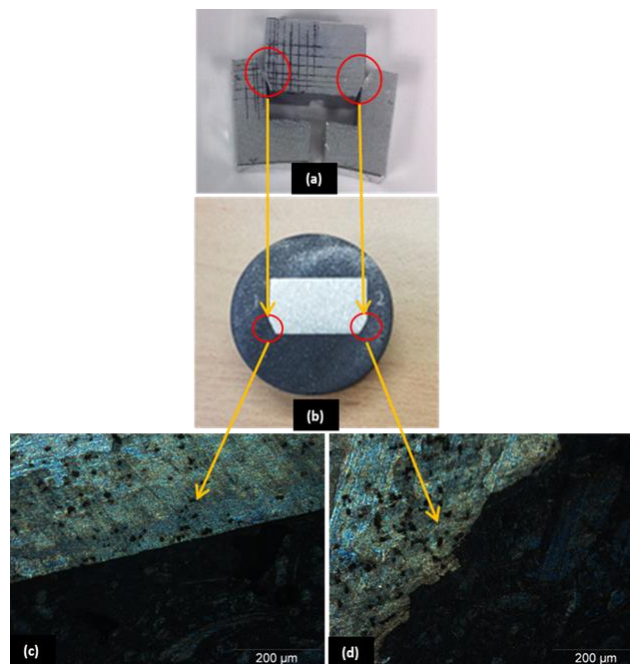


Fig. 2. 35 Fractured lip surface of AA2024

- Influence of temperature

Fig. 2. 36 shows the side view of the fractured specimen of quasi static tension test for AA2024 at different temperatures. At 30°C the fractured was occurred in the specimen thickness at about 30° from the horizontal. The angle of the fractured increase to 35°, 40° and 45° for temperature of 100°C, 150°C and 200°C respectively.

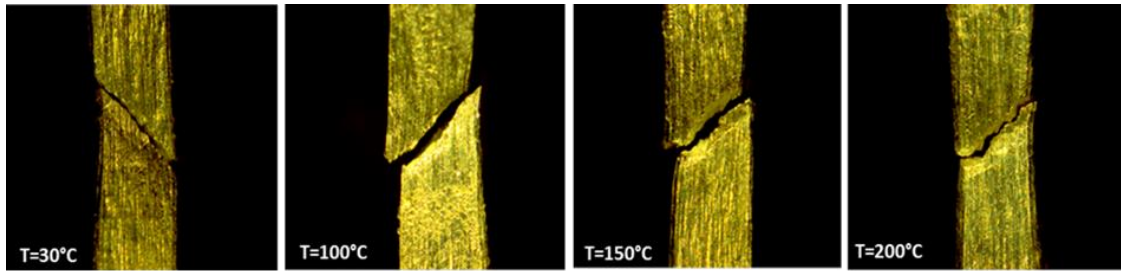


Fig. 2. 36 Fracture of AA2024 at different temperature

Fig. 2. 37 shows the front view of the fractured specimen under quasi static tension test at different temperature, where there is only small necking effect depicted for temperature of 200°C.

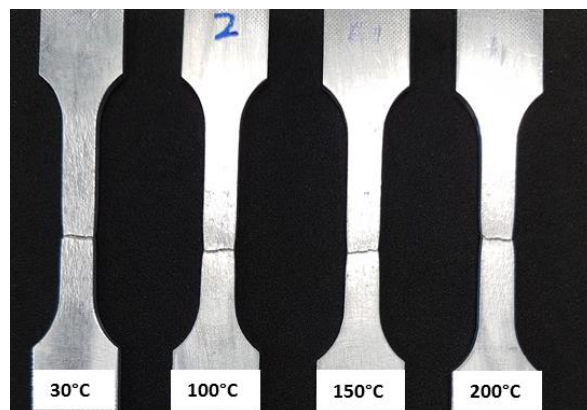


Fig. 2. 37 Front view of fracture for AA2024

Fig. 2. 38 to Fig. 2. 41 shows the microstructure of the tension test at ambient temperature, 100°C, 150°C and 200°C respectively. For ambient temperature the coarse zoom shows the dimple cluster and fine zoom shows there is a small shearing zone that appears along with the dimple cluster. With the increasing of the temperature the microstructure shows the appearance of more dimple cluster and void thus increasing the ductility as expected.

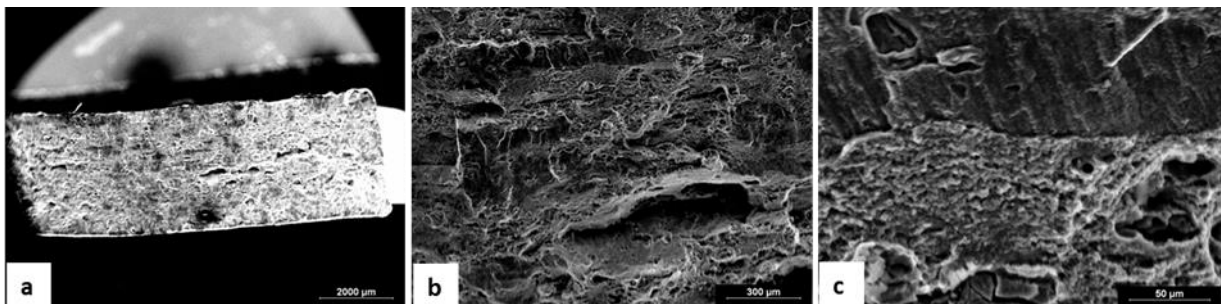


Fig. 2. 38 Fractured surface at T=30°C

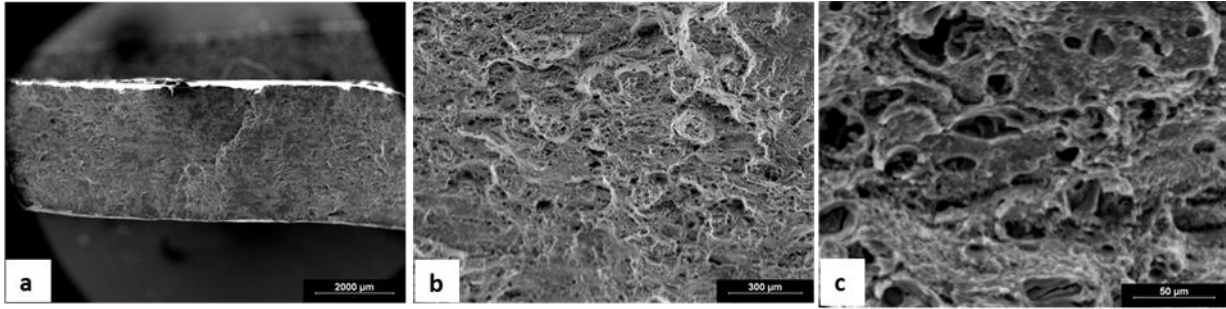


Fig. 2.39 Fractured surface at T=100°C

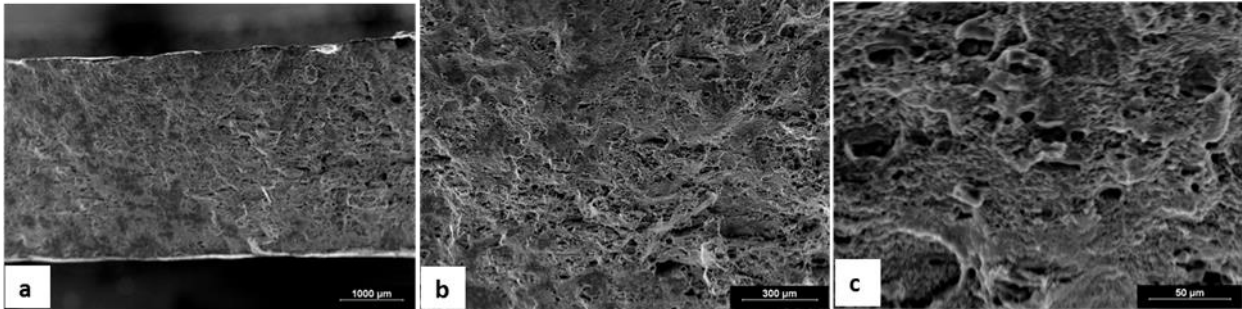


Fig. 2.40 Fractured surface at T=150°C

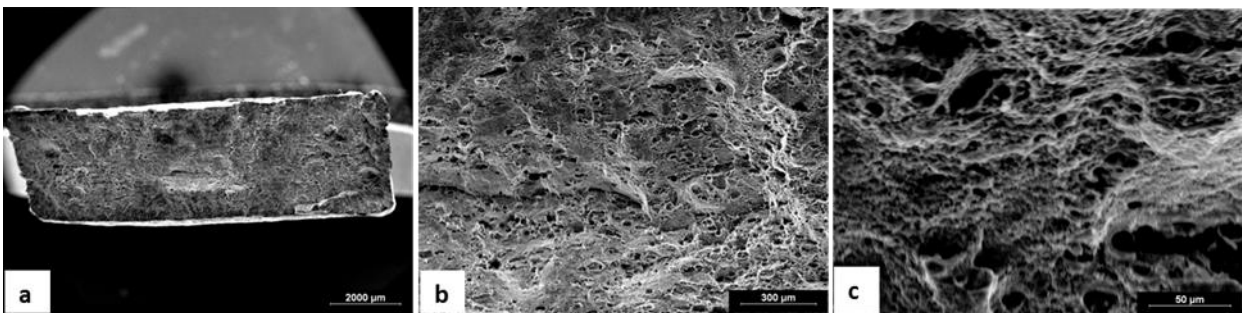


Fig. 2.41 Fractured surface at T=200°C

2.4.1.4 Summary

Two different strain rates were applied in quasi static range for AA2024 in tension, which are 10^{-3} s^{-1} and 10^{-1} s^{-1} . The results show that there is no significant effect of strain rate in considered quasi static range. Significant Strain hardening was depicted up to 0.12 of plastic strain in tension. For quasi static compression test, strain rate of 10^{-2} s^{-1} and 36 s^{-1} were imposed. The results show that there was no significant effect of strain rates on this alloy in the considered range. The amount of strain during which Strain hardening is significant is larger under quasi static compression compared to in quasi static tension which is about 0.2. For the dynamic compression tests, two different strain rates were applied which are 2220 s^{-1} and 4500 s^{-1} . The results show that the alloys behaviour is slightly different but still not very significant to conclude about the strain rate dependence of the material. However the alloy shows the stress is higher in dynamic range compared to quasi static range of strain rates. The flow stress still depicts increasing trend even after 0.2 of plastic strain.

Fig. 2.42 shows superposition of the tension and compression flow curve at different strain rate. Flow curve shows the material behaviour is almost symmetrical where hardening for compression is slightly higher.

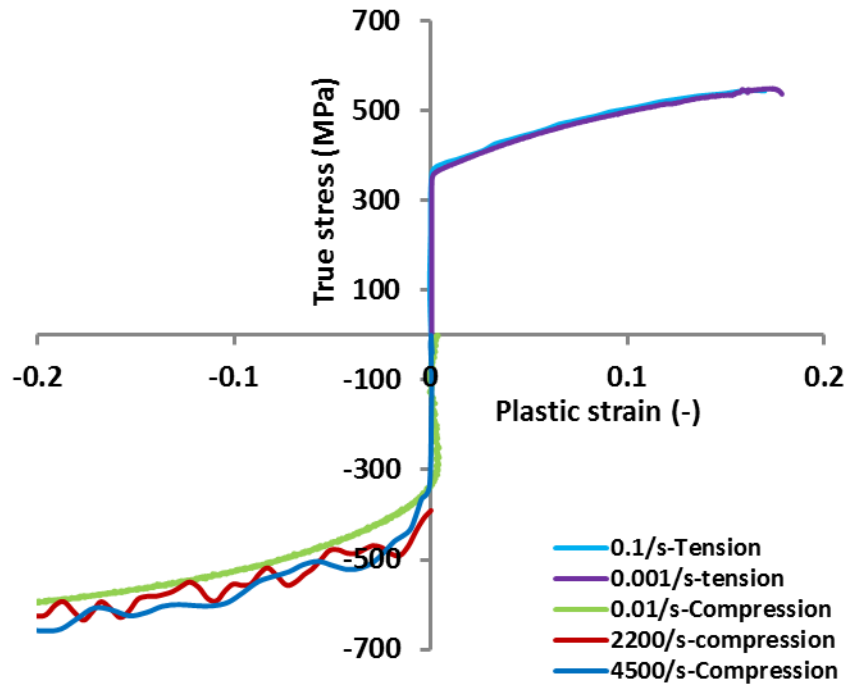


Fig. 2.42 Superposition of flow curve for tension and compression loading for AA2024

The temperature effect on AA2024 shows the gradual decrease in the flow stress with the increasing temperature. However the alloy still depicts strain hardening until temperature of 200°C.

Quasi static compression on hat shape specimen shows that the Couque shape require larger force to deform compared to Meyer shape specimen, as expected. Dynamic shear compression test show the force evolution is larger for Couque compared to Meyer shape specimen.

Fracture occurs at angle of 30° from horizontal plane during the quasi static tension test for AA2024 at ambient temperature. The fractured for 100°C, 150°C and 200°C is 35°, 40° and 45° respectively. Analysis on the fractured surface shows that the ductility of the alloy is increasing with increasing temperature. This can be evidenced by the increasing of the dimple cluster and voids on the fractured surface.

Microstructure of the quasi static and dynamic compression shows the specimen remain quasi homogenous after the test. Dynamic shear compression test shows the fractured surface is purely under shear for Meyer type specimen and combination of shear and possible tension for Couque shape specimen due to appearance of the dimples on the fractured surface. The fracture lip analysis on Couque type specimen does not show any evidence of ASB.

2.4.2 AA7175

The results obtained for AA7175 are shown and commented in this section.

2.4.2.1 Response under tension and compression loading

In this section the results of tension and compression will be discussed for both low and high strain rate loading for AA7175.

- **Monotonic loading**

- Influence of stress triaxiality

Fig. 2. 43(a) and Fig. 2. 43 (b) show the engineering stress versus engineering strain for tensile test with notched specimen at ambient temperature and at 200°C respectively for AA7175. The initial stress is higher for notch radius of 2 mm at about 480 MPa. The initial stress is about 465 MPa and 430 MPa for notch radius of 10 mm and smooth specimen respectively. At temperature of 200°C the initial stress is 340 MPa, 340 MPa and 250 MPa for notch radius of 2 mm, 10 mm and smooth specimen respectively. Table 2. 14 and Table 2. 15 show the influence of stress triaxiality on initial stress, maximum stress and strain at fracture for room temperature and 200°C respectively.

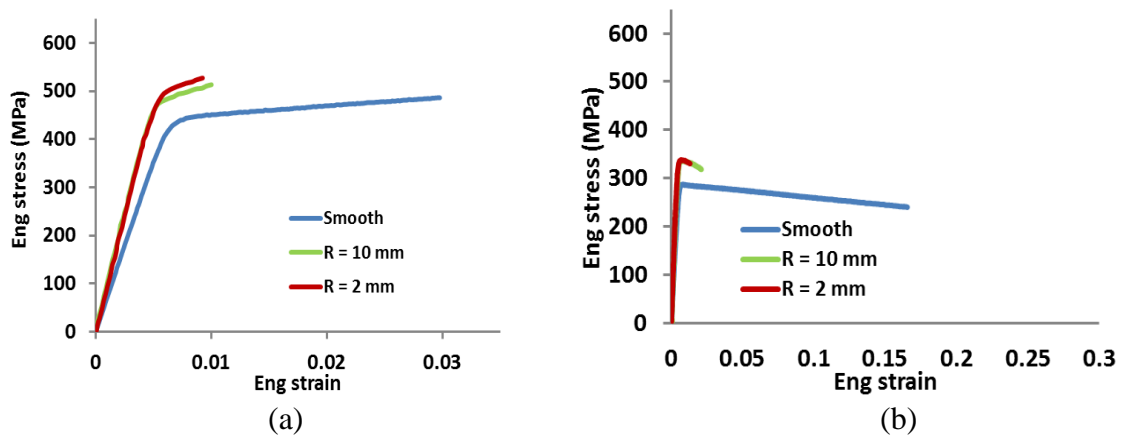


Fig. 2. 43 Engineering stress vs engineering strain on AA7175 notched specimen for quasi static tension loading (a) Ambient temperature (b) 200°C

Table 2. 14 Stress triaxiality influence on stress and strain at fracture at room temperature

<i>Geometry</i>	<i>Stress triaxiality</i>	<i>Initial stress (MPa)</i>	<i>Max stress (MPa)</i>	<i>Strain at fracture</i>
<i>Smooth</i>	<i>1/3</i>	<i>430</i>	<i>504</i>	<i>0.03</i>
<i>R10</i>	<i>0.475</i>	<i>465</i>	<i>522</i>	<i>0.02</i>
<i>R2</i>	<i>0.572</i>	<i>480</i>	<i>554</i>	<i>0.008</i>

Table 2. 15 Stress triaxiality influence on stress and strain at fracture at 200°C

<i>Geometry</i>	<i>Stress triaxiality</i>	<i>Initial stress (MPa)</i>	<i>Max stress (MPa)</i>	<i>Strain at fracture</i>
<i>Smooth</i>	<i>1/3</i>	<i>285</i>	<i>285</i>	<i>0.27</i>
<i>R10</i>	<i>0.475</i>	<i>330</i>	<i>335</i>	<i>0.048</i>
<i>R2</i>	<i>0.572</i>	<i>332</i>	<i>338</i>	<i>0.038</i>

Fig. 2. 44 (a) and Fig. 2. 44 (b) show the initial yield and maximum engineering stress versus stress triaxiality for room temperature and 200°C. Initial yield and maximum engineering stress is increasing with the increases of stress triaxiality for both at room temperature whereas at 200°C the stress triaxiality influence is overcome by thermal softening.

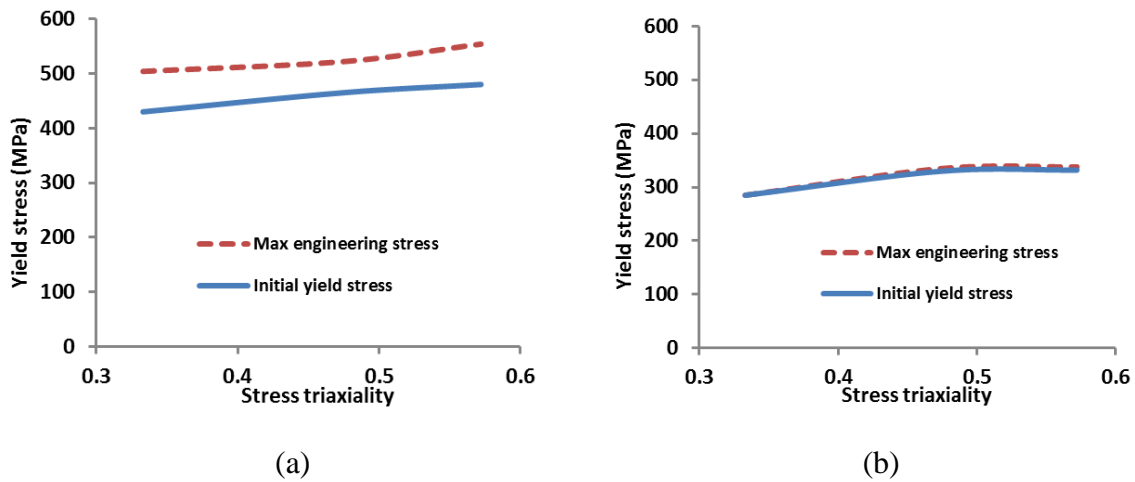


Fig. 2. 44 Engineering stress vs stress triaxiality for initial yields stress and maximum engineering stress for (a) Room temperature (b) 200°C

- Influence of strain rate

Fig. 2. 45(a) and Fig. 2. 45(b) show the results at different strain rates for tension and compression tests respectively. Tension test strain rate of 10^{-3} and 10^{-1} were superimposed. There is slightly strain rate effect for AA7175 for the considered quasi static range in tension. Quasi static compression was carried out at two different strain rates which are 10^{-2} and 36 s^{-1} . The results show there is slight strain rate effect up to plastic strain of 0.1 before depicting plateau. Table shows the young modulus, initial yield stress and strain hardening for tension and compression test in quasi static range. Table 2. 16 shows the strain rate influence on young's modulus, initial yield stress and strain hardening. To be noted that the values for strain hardening presented here is the value of the hardening parameter in Hollomon's equation.

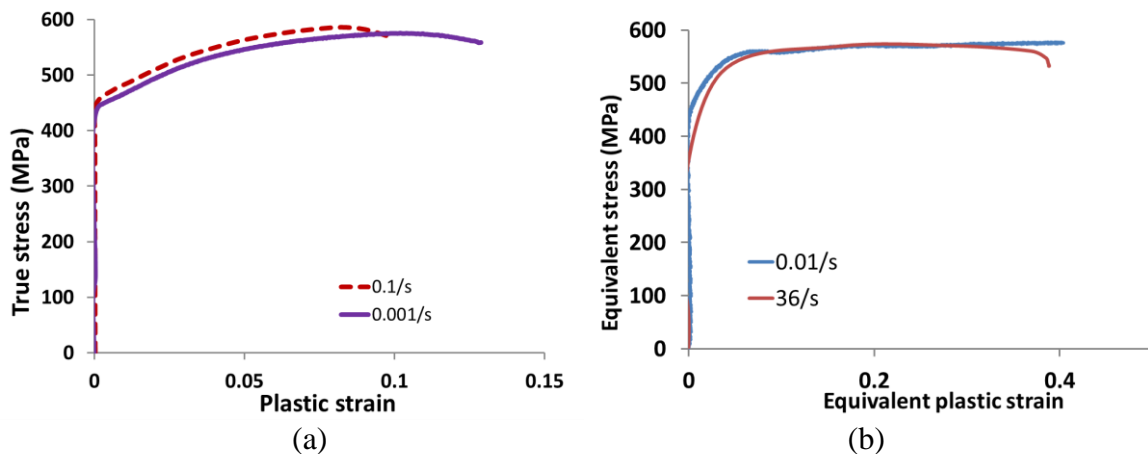


Fig. 2. 45 True stress vs plastic strain for AA7175 under (a) quasi static tension (b) quasi static compression

Fig. 2. 46 shows the comparison of quasi static and dynamic compression tests. Three different strain rates are considered which are 10^{-2} , 2020 and 4500 s^{-1} . The results show that there is slight strain rate dependence for this alloy especially at higher strain rate. However the initial yield stress is about the same for low and high strain rate at about 460 MPa. Strain hardening depicted up to 0.05 for all three curves at different strain rate. The curve at high

strain rate i.e 2020 and 4500 shows a sudden drop in stress which is indicates the occurrence of instability in the form of ASB as shown later.

Table 2. 16 Strain rate influence on Young's modulus, initial yield stress and strain hardening in quasi static tension and compression loading

AA7175	Strain rate (s-1)	Young's modulus (GPa)	Initial yield stress (MPa)	Strain hardening
Tension	10^{-3}	65	445	0.13
	10^{-1}	66	450	0.12
Compression	10^{-2}	irrelevant	440	0.16
	36	irrelevant	390	0.18

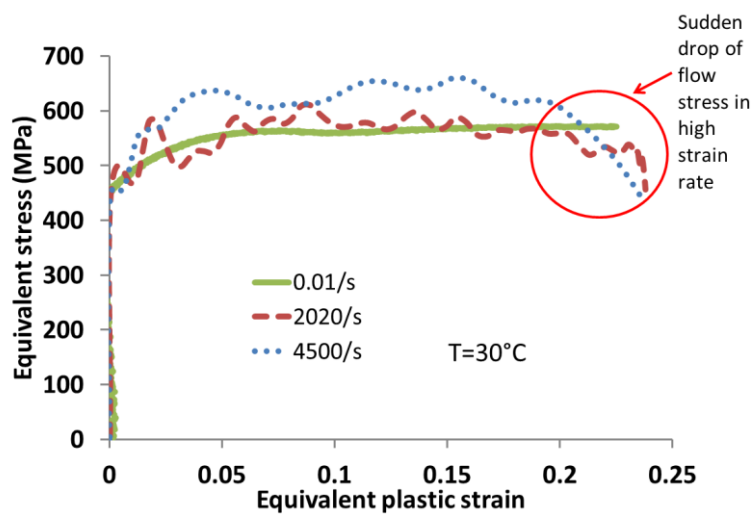


Fig. 2. 46 Equivalent stress vs equivalent plastic strain for dynamic and quasi static compression for AA7175

Table 2. 17 shows the yield stress at various plastic strains and strain rates.

Table 2. 17 Yield stress at various strain and strain rate

Strain rate (s^{-1})	Plastic strain	0.02	0.04	0.06	0.08	0.1
10^{-2}	Yield stress (MPa)	506	540	550	560	560
2220	Yield stress (MPa)	540	560	571	580	582
4500	Yield stress (MPa)	580	620	640	630	625

Fig. 2. 47 shows the yield stress vs strain rate at different plastic strain. The curve shows that yield stress depends on plastic strain.

- Influence of temperature

Fig. 2. 48 shows the flow curve for AA7175 at different temperature. The tests were carried out from ambient temperature of 30°C to 200°C. The initial yield stress is decreasing with the

increasing of temperature. Initial yield stress decreasing from about 430 MPa, 420MPa, 400 MPa and 350 MPa with the temperature of 30°C, 100°C, 150°C and 200°C respectively. For ambient temperature the flow curve depicts strain hardening up to 0.05 and decreases to 0.04 at 100°C. Strain hardening is decreasing to 0.01 for 150°C and at 200°C there is no strain hardening at all. To be noted that the strain hardening value presented here is the plastic strain value up to ultimate strength of material from flow curve.

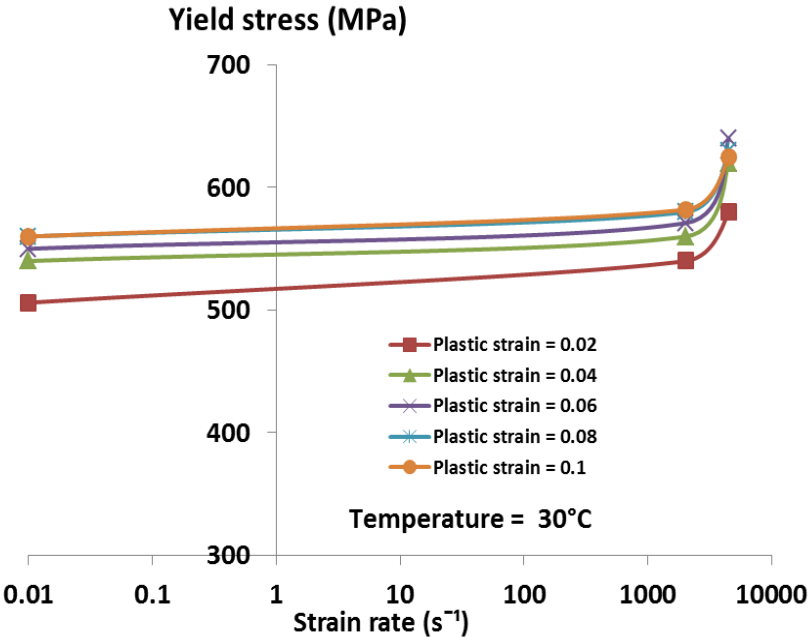


Fig. 2. 47 Yield stress vs strain rate for different plastic strain

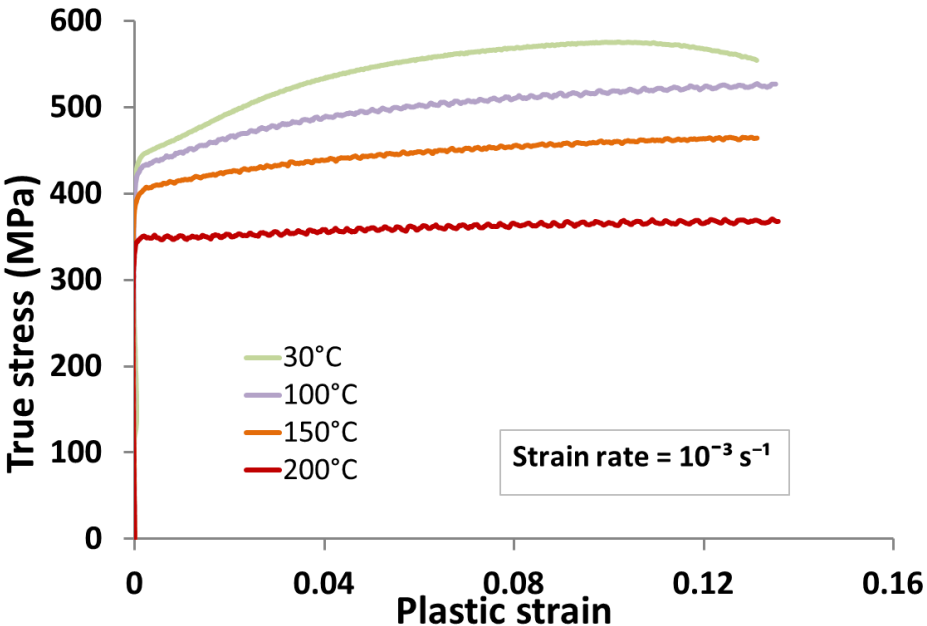


Fig. 2. 48 True stress vs plastic strain for AA7175 at different temperature

Table 2. 18 shows the yield stress at various plastic strains and temperatures.

Table 2. 18 Yield stress at various strain and temperature

Temperature (°C)	Plastic strain	0.02	0.04	0.06	0.08
30	Yield stress (MPa)	496	536	558	567
100	Yield stress (MPa)	463	487	500	509
150	Yield stress (MPa)	425	439	447	455
200	Yield stress (MPa)	351	358	361	364

Fig. 2. 49 shows the curve for yield stress vs temperature at different plastic strain. At lower temperature it shows that the yield stress is dependent on plastic strain, where the stress is increase with the plastic strain. This pattern can be seen up to 150°C. At temperature of 200°C the yield stress become independent of plastic strain where thermal softening overcome the strain hardening.

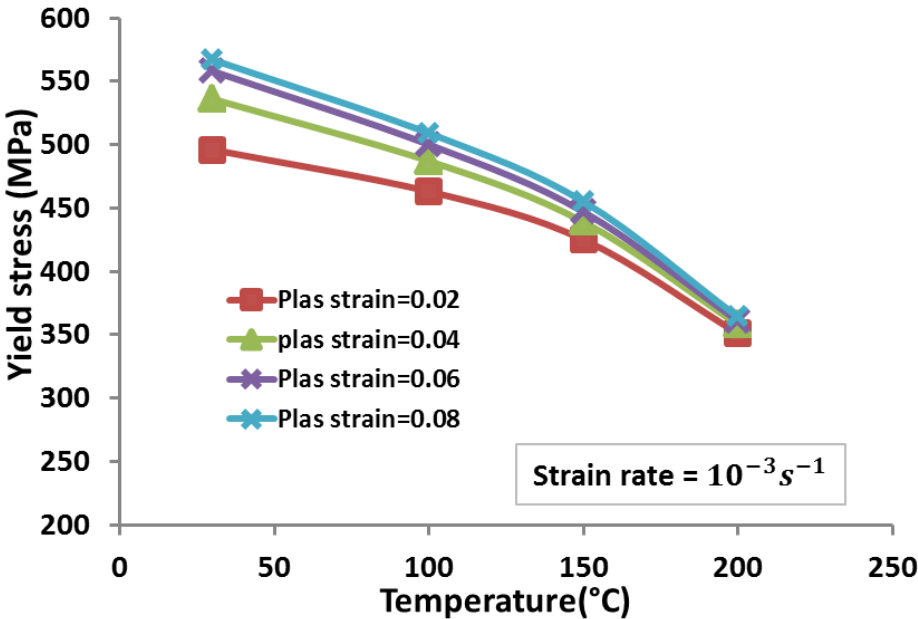


Fig. 2. 49 Yield stress vs temperature for different plastic strain

- Relaxation tests**

Relaxation test results are presented in this section as true stress versus plastic strain. Curve for velocity, force, strain rate and stress evolution are presented in appendix (b) Fig. 2. 50(a) and Fig. 2. 50(b) show the flow curve for tension and compression relaxation test

respectively. The results show the viscous stress part for both tension and compression test. Further discussion concerning this part will be presented in the chapter of analytical modelling.

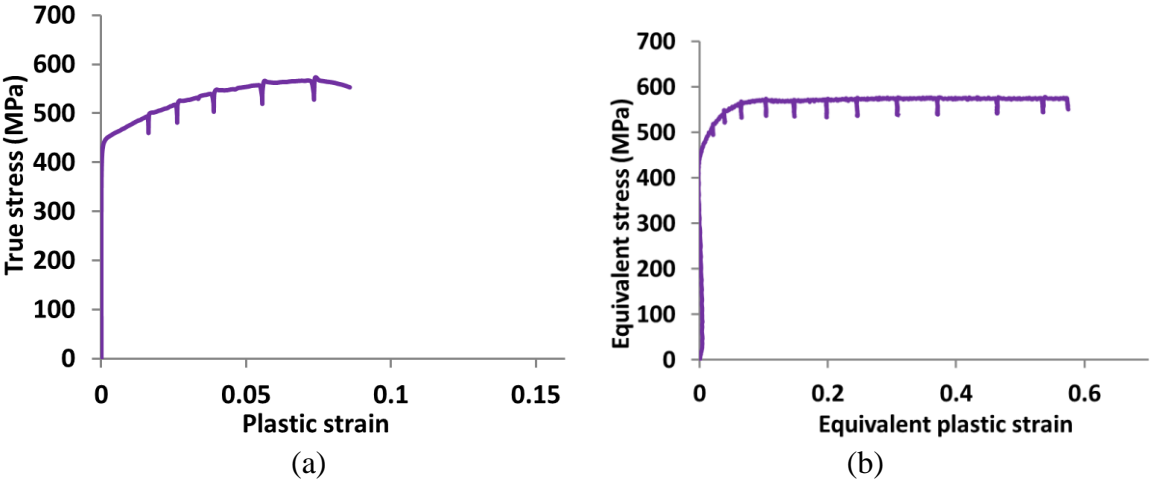


Fig. 2. 50 Flow curve for AA7175 under (a) Tension (b) Compression loading

Fig. 2. 51 (a) and Fig. 2. 51(b) show viscous stress vs plastic strain for tension and compression in quasi static range. The curve shows that the viscous stress is independent of plastic strain. The value for viscous stress for tension and compression are about 26 MPa and 24 MPa respectively.

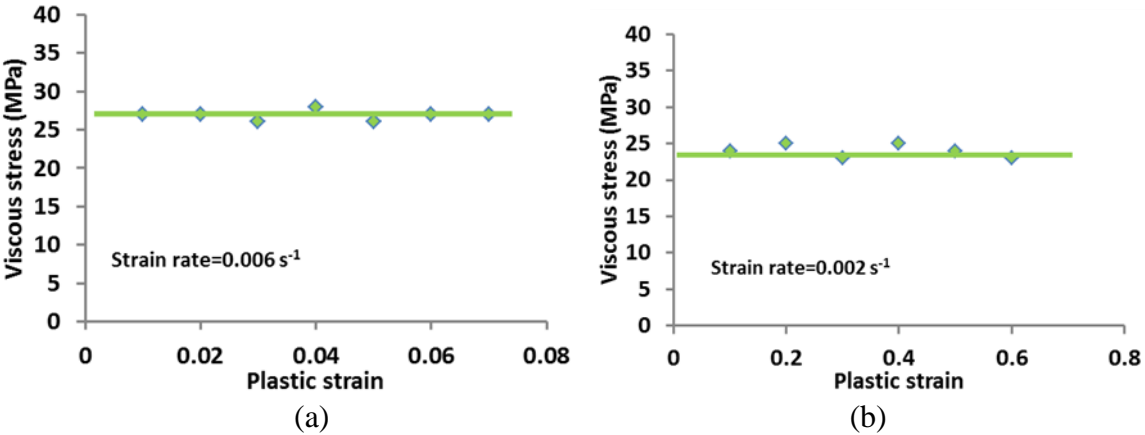


Fig. 2. 51 Viscous stress vs plastic strain

Fig. 2. 52 shows viscous stress vs temperature for quasi static tension test. The curve shows that the viscous stress is temperature independent at the considered temperature range.

2.4.2.2 Response under shear-compression loading

- Influence of strain rate

Fig. 2. 53(a) and Fig. 2. 53(b) show force versus time for quasi static and dynamic shear compression respectively for hat shape specimens on AA7175. Both quasi static and dynamic test show that a larger force was required to deform Couque type specimen. Generally magnitude of force was larger for dynamic compression compared to quasi static

compression. A drop in force is observed for both Meyer and Couque specimens under dynamic loading, as the consequence of a material instability (ASB as shown later).

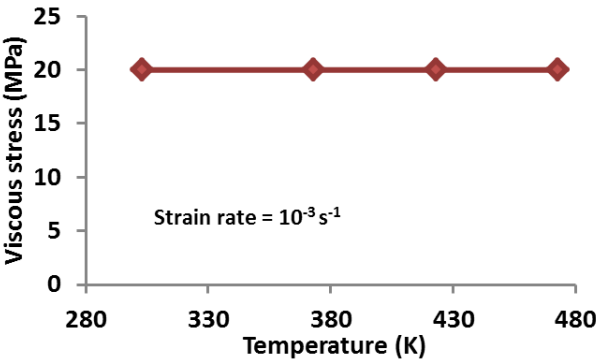


Fig. 2.52 Viscous stress vs temperature

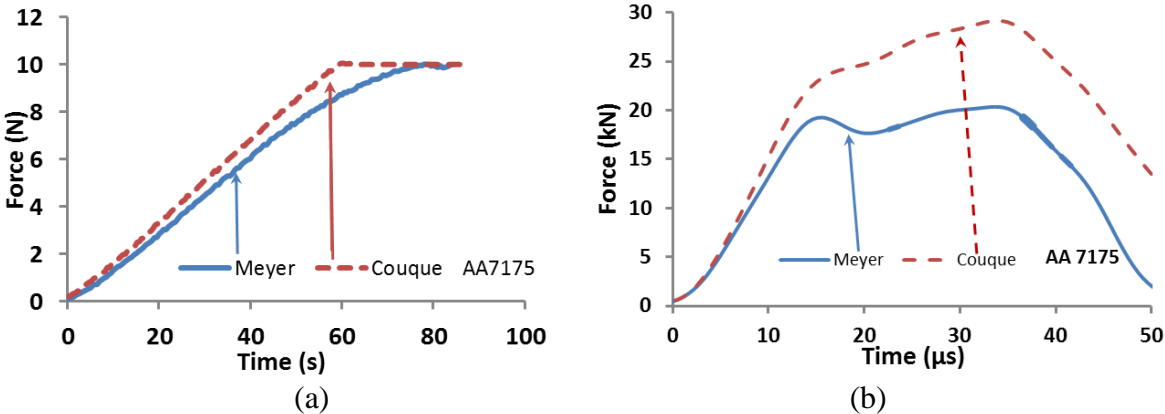


Fig. 2.53 Force evolution for AA7175 under (a) Quasi static (b) Dynamic shear compression loading

Table 2. 19 shows maximum force for Meyer and Couque type specimen under quasi static and dynamic loading.

Table 2. 19 Maximum force for Meyer and Couque shape specimen in quasi static and dynamic compression loading

Strain rate	Geometry	Max force(kN)
Static	Meyer	>10
	Couque	>10
Dynamic	Meyer	20.4
	Couque	29.2

2.4.2.3 Fracture analysis

The deformed shape, fractured angle and fractured surface of the specimens will be discussed for AA7175 in this section.

- Influence of stress triaxiality ratio

Fig. 2. 54(a) and Fig. 2. 54(b) shows the Meyer and Couque type specimens after dynamic shear compression test for AA7175. Meyer type specimen is fully fractured and compressed up to the edge, see Fig. 2. 54(a). For the Couque type specimen it is partly fractured and remains stick together as depicted in Fig. 2. 54(b).

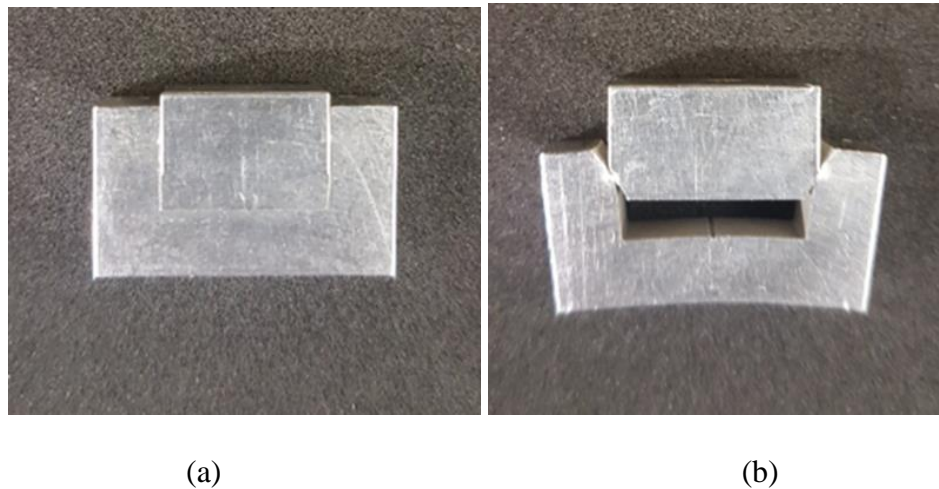


Fig. 2. 54 Specimen after dynamic shear compression test (a) Meyer and (b) Couque

Fig. 2. 55 shows the fractured surface of the Meyer type specimen for AA7175. The region was distinguished into two zones. First zone was the initiation of the fracture and the second zone was the fracture propagation. The microstructure for the both zones shows that the fracture was under shearing induced Mode II, see Fig. 2. 55(c) and Fig. 2. 55(d).

Fig. 2. 56 shows the fractured surface of the Couque type specimen for AA7175. The region was distinguished into three zones. First zone was the initiation of the fracture and the second zone was the fracture propagation. The microstructure for the fracture initiation at zone 1 and 2 show shearing induced Mode II failure with possible friction, see Fig. 2. 56 (c) and Fig. 2. 56(d).

whereas for zone 3, where the fracture arrest was under possible tension induced Mode I failure due to appearance of dimple cluster, see Fig. 2. 56(e).

- Influence of strain rate

Fig. 2. 57(a) and Fig. 2. 57(b) show the specimen after quasi static and dynamic compression respectively for AA7175. Under quasi static loading the specimen shows a single plane of fracture and become oval shape as depict in Fig. 2. 57(a). The specimen shows the cross lines under dynamic compression as depicted in Fig. 2. 57 (b).

Fig. 2. 58(a) and Fig. 2. 58(b) show the microstructure of the specimen after quasi static compression and dynamic compression respectively. The microstructure observation was done by applying method M4, as discussed earlier. Microstructure of AA7175 under quasi static loading shows wide shear localization in the slip line region, see Fig. 2. 58 (a). This wide shear localization is known as weakly heterogeneous deformation [15]. Under dynamic loading thin strong localisation in the form of adiabatic shear band is visible, see Fig. 2. 58

Microstructure of the AA7175 specimen after (a) Quasi static and (b) Dynamic compression test(b).

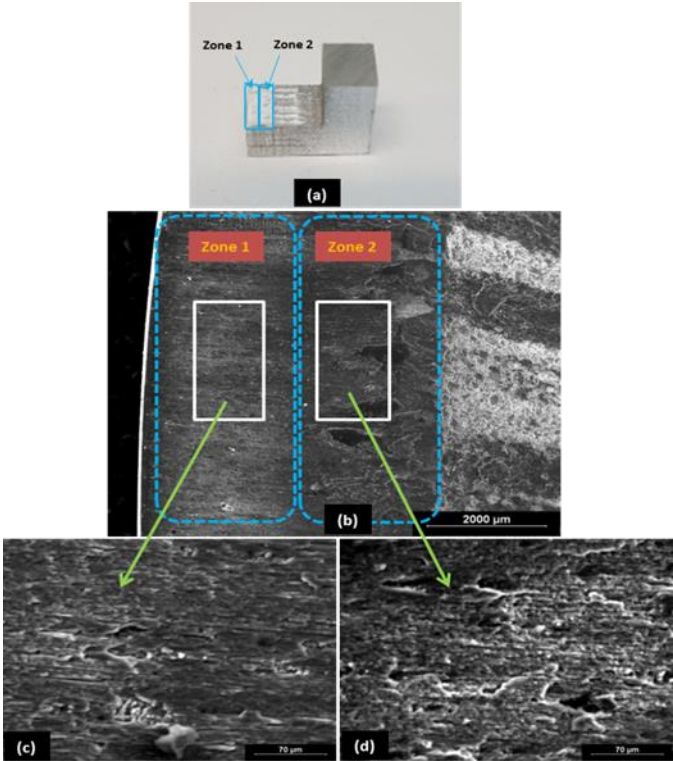


Fig. 2. 55 Meyer type specimen AA7175

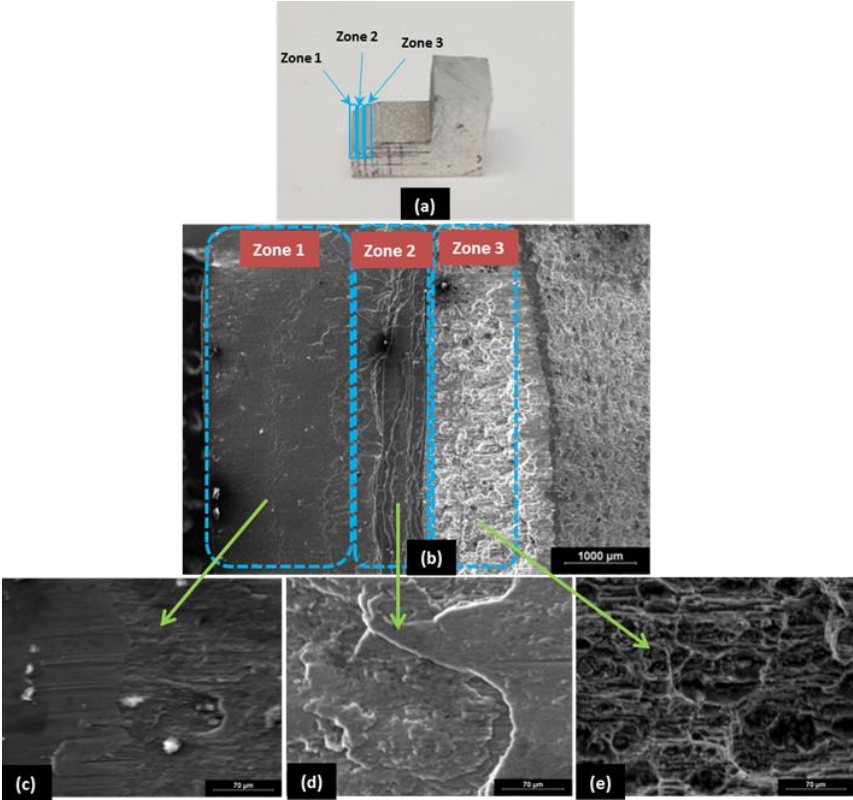


Fig. 2. 56 Couque type specimen AA7175

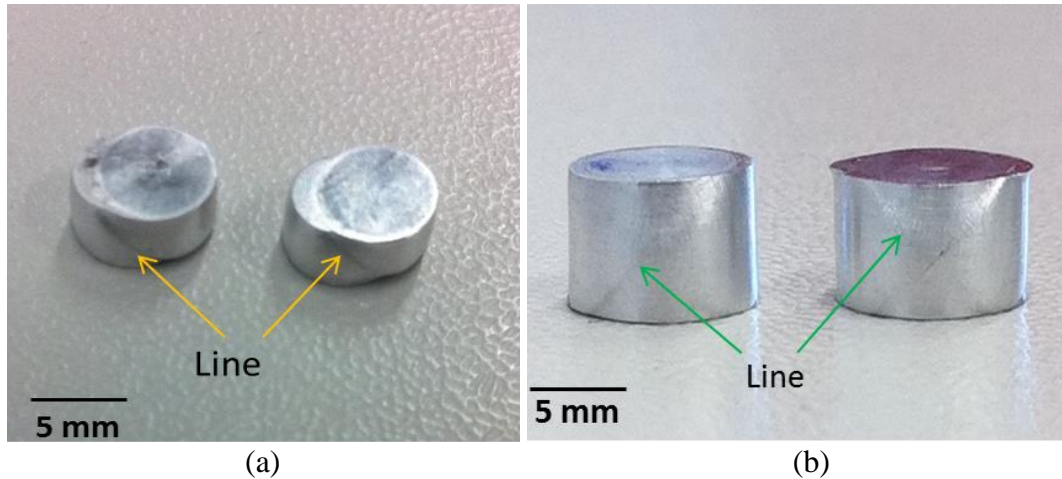


Fig. 2. 57 Specimen of the AA7175 after (a) Quasi static and (b) Dynamic compression

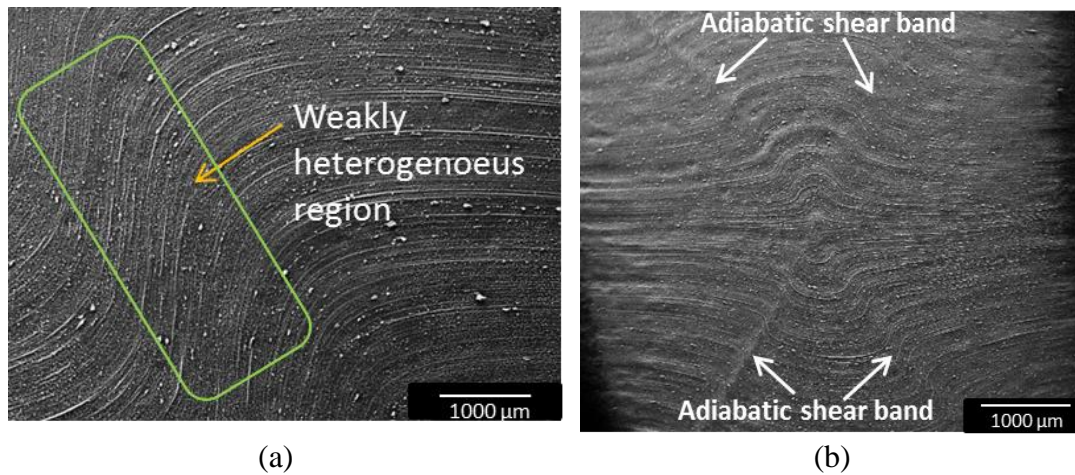


Fig. 2. 58 Microstructure of the AA7175 specimen after (a) Quasi static and (b) Dynamic compression test

Fig. 2. 59 shows the fractured surface of dynamic shear compression specimen for Couque shape. The specimen was prepared by applying method M4. The specimen was observed at the lip of the fractured region by using optical microscope. Fractured lip region for AA7175 shows the evidence of ASB as depicted in Fig. 2. 59(c) and Fig. 2. 59(d).

- Influence of temperature

Fig. 2. 60 shows the side view of the fractured specimen of the quasi static tension test for AA7175 at different temperature. The fracture angle is about 30° for temperature of 30°C and 100°C. For temperature 150°C the fractured angle is about 45°. At temperature of 200°C a necking with tortuous crack occur as depicted. Fig. 2. 61 shows the front view of the fractured specimen under quasi static tension at different temperature for AA7175. Necking is depicted at temperature of 150°C and 200°C for this alloy.

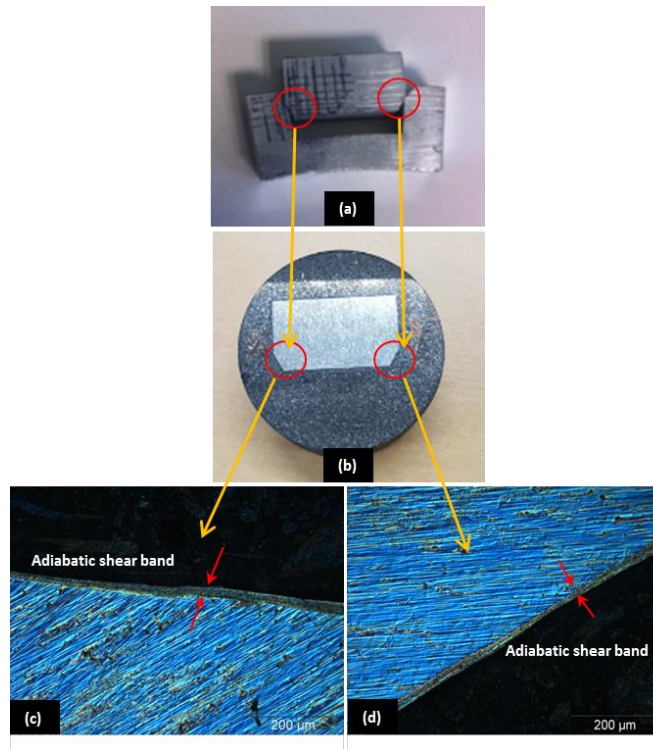


Fig. 2. 59 Fractured lip specimen for AA7175

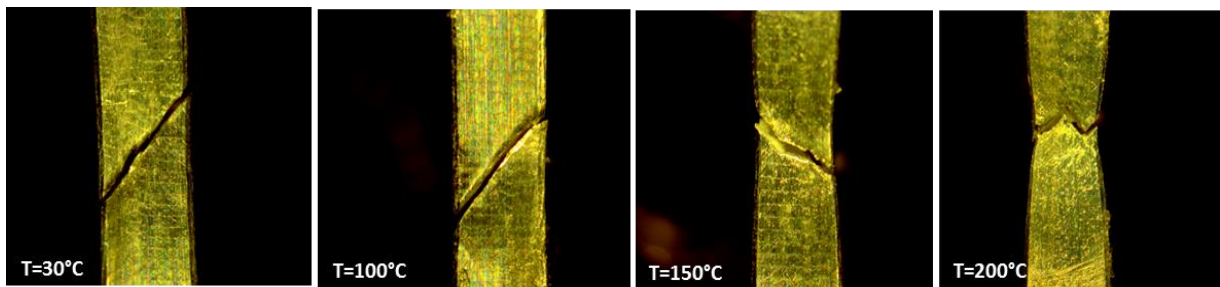


Fig. 2. 60 Fracture of AA7175 at different temperature

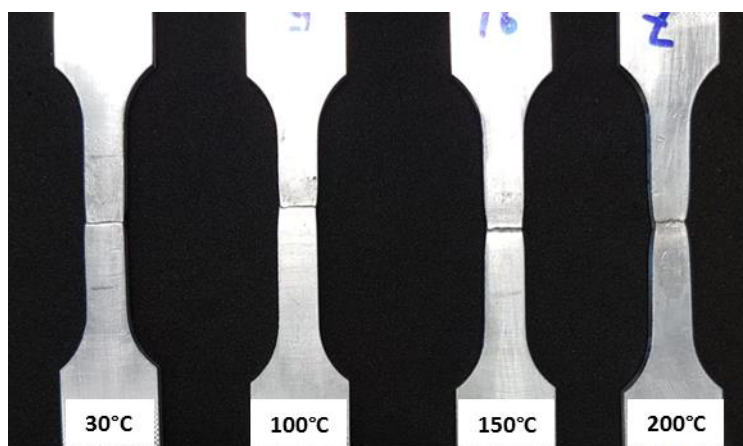


Fig. 2. 61 Front view of fracture for AA7175

Fig. 2. 62 to Fig. 2. 65 shows the microstructure at fractured surface for AA7175 after quasi static tension test at ambient temperature, 100°C, 150°C and 200°C respectively. At ambient

temperature the microstructure shows flat surface with dispersed. The small dimples can be seen at fine zoom as indicated by arrow on Fig. 2. 62 Fractured surface at T=30°C (c). At temperature of 100°C the dimples become larger as depicted in Fig. 2. 63 (c) where the material ductility is increasing. Fig. 2. 64 shows the fractured surface of alloy at 150°C. The coarse zoom shows more dimple clusters in the fractured surface, see Fig. 2. 64 (b). Fine zoom shows the large voids, see Fig. 2. 64 (c). At temperature of 200°C, the coarse zoom shows the fractured surface with a lot of dimples, see Fig. 2. 65 (b). Fine zoom at 200°C shows the coalescence of voids and the alloy looks torn and pulled with the appearance of striation thus makes the material very ductile, see Fig. 2. 65 (c).

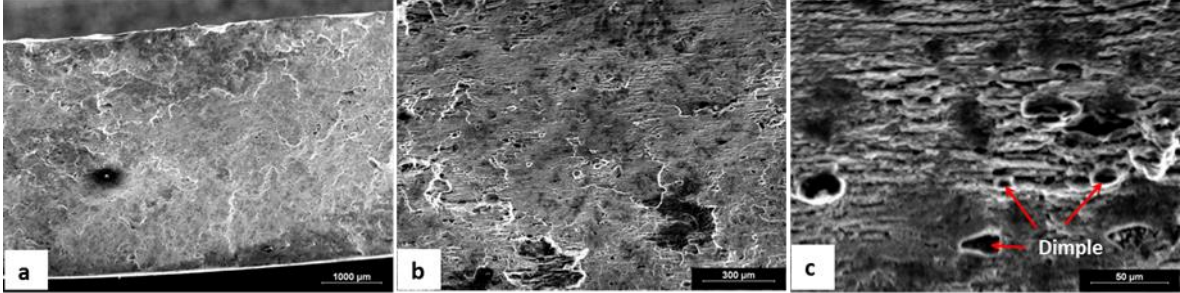


Fig. 2. 62 Fractured surface at T=30°C

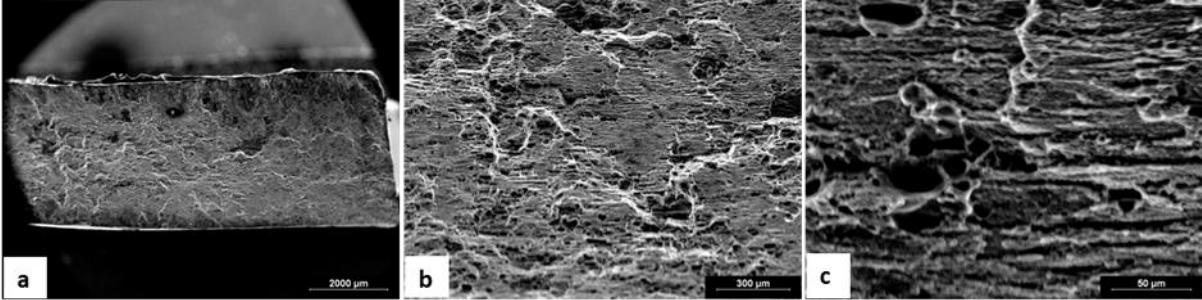


Fig. 2. 63 Fractured surface at T=100°C

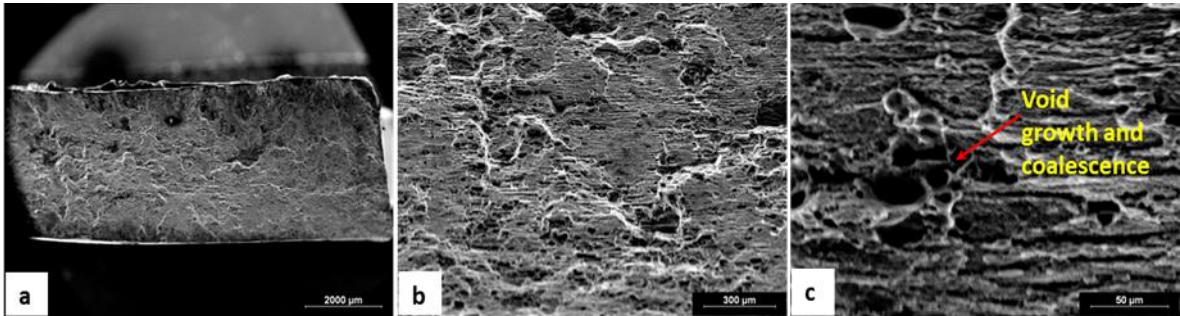


Fig. 2. 64 Fractured surface at T=150°C

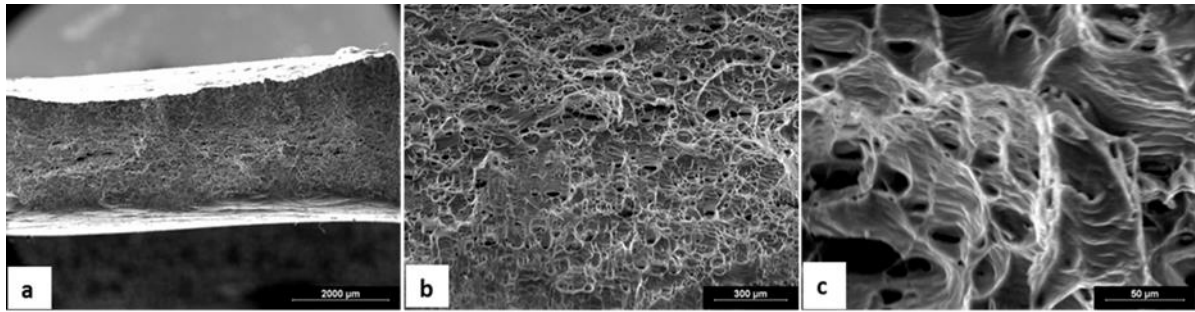


Fig. 2.65 Fractured surface at T=200°C

2.4.2.4 Summary

Strain rates of 10^{-3} s^{-1} and 10^{-1} s^{-1} were applied to AA7175 for quasi static tension test. The results show that there is no significant effect of strain rates on this alloy at the considered strain rate range. Strain hardening was depicted up to about 6% of the plastic strain for both in quasi static tension and compression. Above 6% the curve for tension depicts necking whereas for quasi static compression the curve becomes a plateau until the test was stopped at 25%.

For dynamic compression test, two different strain rates were applied which are 2020 s^{-1} and 4500 s^{-1} . The results show that there was no significant difference for both strain rates in the considered dynamic range. However the flow curve shows a significant difference between quasi static and dynamic test. The flow curve is slightly higher at high strain rate compression. For dynamic compression test, AA7175 shows a sudden drop in stress at plastic strain of 20% for both considered strain rates.

Fig. 2.66 shows the superposition of the tension and compression flow curve at different strain rates. The flow curve shows that the initial yield stress under compression loading is higher than tension loading but both depict almost the same strain hardening.

The temperature effect on AA7175 is quite critical. At ambient temperature the flow curve shows strain hardening up to 6% of plastic strain during quasi static tension test. The Initial yield stress was about 450 MPa. With the increasing of temperature the initial yield stress were decreasing to 430 MPa, 390MPa and 350MPa at temperature of 100°C, 150°C and 200°C respectively. The strain hardening decreases dramatically at 100°C to 150°C. At temperature of 200°C there is no strain hardening at all.

Quasi static compression tests on hat shape specimen reveal that the Couque shape specimen required more force to deform compared to Meyer shape specimen, as expected. Dynamic shear compression test shows that the force evolution is larger for Couque shape specimen compared to Meyer shape specimen.

For quasi static tension test, the specimen fractured at angle of 30° , 35° , 45° and tortuous crack for temperature of 30°C, 100°C, 150°C and 200°C respectively. The necking before fracture is occurring at temperature of 150°C and 200°C. Observation of the microstructure on the fractured surface shows that the specimen ductility is increasing with the increase of the temperature as the number and size of void increase, and that the micro-mechanisms of damage seem to be in the form of shear decohesion below 100°C and voiding above that due to void growth and coalescence.

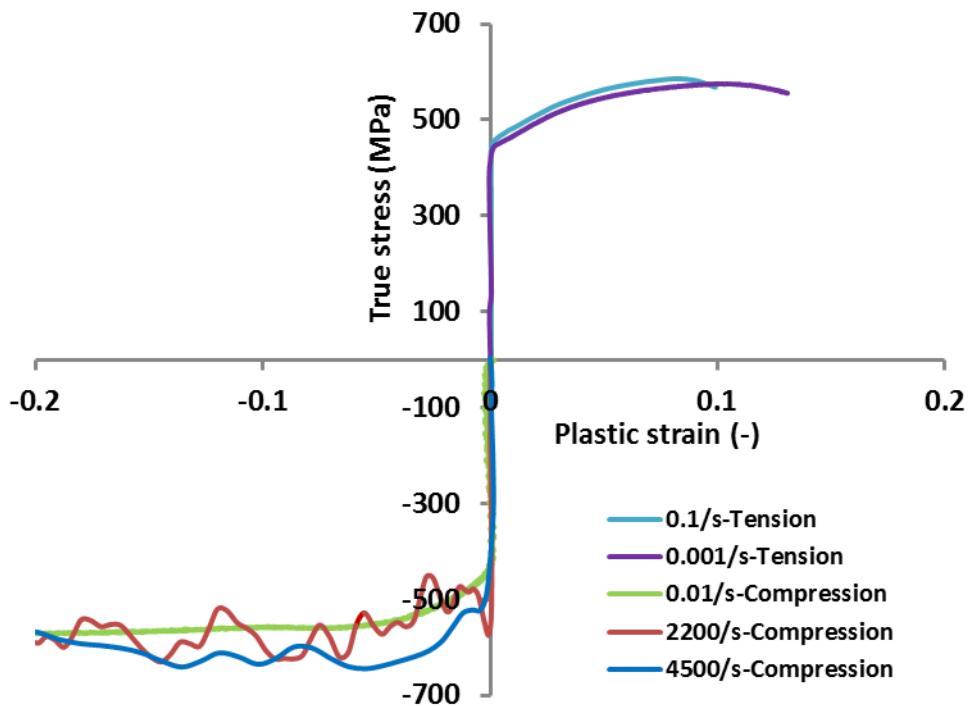


Fig. 2. 66 Superposition of flow curve for tension and compression loading for AA7175

Microstructure of the dynamic compression specimen shows the formation of adiabatic shear band. The adiabatic shear band appears across the specimen, see Fig. 2. 58 Microstructure of the AA7175 specimen after (a) Quasi static and (b) Dynamic compression test(b), which explains the drop in stress observed on the stress-strain curves. Dynamic shear compression test on Meyer shape specimen shows the failure is under pure shear mode whereas for Couque shape specimen it was under combination of shear and tension mode. The fracture lip analysis on the Couque shape specimen shows the evidence of the shear band, see Fig. 2. 59(c) and Fig. 2. 59(d).

2.4.3 AA2024 vs AA7175

This section will discuss comparison of both alloys in term of strain hardening, strain rate hardening, thermal softening and fracture.

2.4.3.1 Regarding strain hardening

Fig. 2. 67(a) and Fig. 2. 67(b) show a comparison of flow stress in quasi static tension and compression for both alloys. From quasi static tension test at ambient temperature, initial yield stresses for AA2024 and AA7175 are 340 MPa and 450 MPa respectively. The initial yield stress decreases gradually for AA2024 whereas dramatically decreases for AA7175. Strain hardening can be seen for AA2024 at ambient temperature in tension test up to 12% whereas for AA7175 only about 6% of plastic strain. For quasi static compression test strain hardening is depicted up to 20% for 2024 and 6% for AA7175.

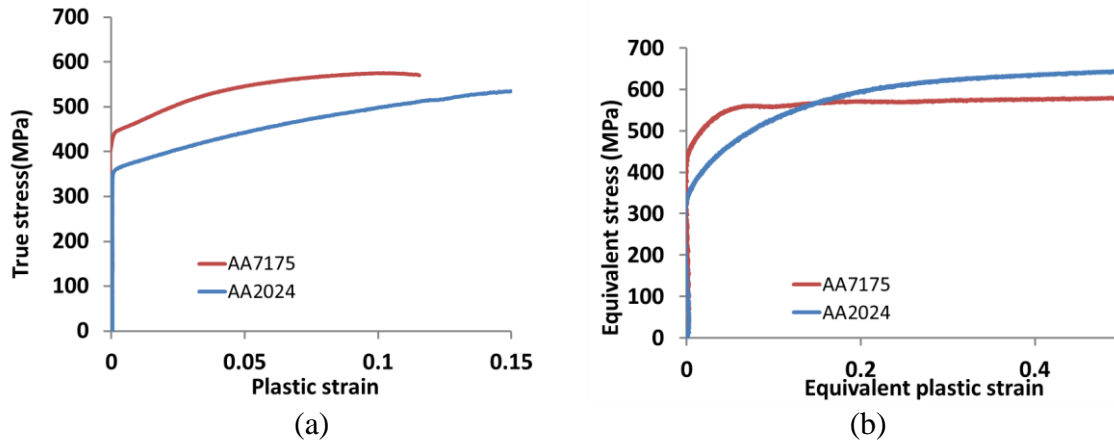


Fig. 2. 67 Comparison of flow stress for AA2024 and AA7175 in (a) Quasi static tension and (b) Quasi static compression

2.4.3.2 Regarding strain rate hardening

For higher strain rate, dynamic compression test was conducted for both alloys where strain rate of 2200 s^{-1} and 4500 s^{-1} were obtained. Flow curve does not show any significant effect of strain rate hardening for both alloys. However when comparing with quasi static range of strain rate, both alloys show that there is a slightly strain rate influence on flow curve. For AA7175 the flow curve in dynamic test shows the sudden drop in stress at plastic strain of 0.2 whereas for AA2024 the flow curve shows stress keeps on increasing at this plastic strain.

2.4.3.3 Regarding thermal softening

Fig. 2. 68 (a), (b) (c) and (d) show the comparison for both alloys at temperature of 30°C , 100°C , 150°C and 200°C respectively under tension loading. AA7175 seems more susceptible at high temperature compared to AA2024. This is due to dramatic decrease in initial yield and strain hardening for AA7175 after 150°C .

2.4.3.4 Regarding fracture

Quasi static tension test shows the fracture occurred at angle of 30° , 35° , 40° and 45° for temperature of 30°C , 100°C , 150°C and 200°C respectively for AA2024. For AA7175 the fracture occurred at angle of 30° , 35° , 45° and tortuous crack of fracture for 30°C , 100°C , 150°C and 200°C respectively. Both alloys show necking before fracture. Microstructure of both alloys in quasi static tension test, shows the void is increasing and become larger with the increase of the temperature thus increasing the ductility. For AA7175 there seems to be a critical temperature (around 100°C) below which the damage micro-mechanisms are mostly controlled by shear decohesion and above which they are mostly controlled by voiding where void growth and coalescence can be seen.

Microstructure of dynamic compression test specimen shows formation of the adiabatic shear band for AA7175 whereas AA2024 remains quasi homogeneous. Dynamic shear compression shows that for both alloys failure is due to shear induced Mode II, for Meyer shape and combination of shearing induced Mode II and tension induced Mode I failure for Couque shape specimen. The fracture lip analysis for Couque shaped specimen shows the formation of ASB for AA7175 whereas there is no evidence of shear band for AA2024.

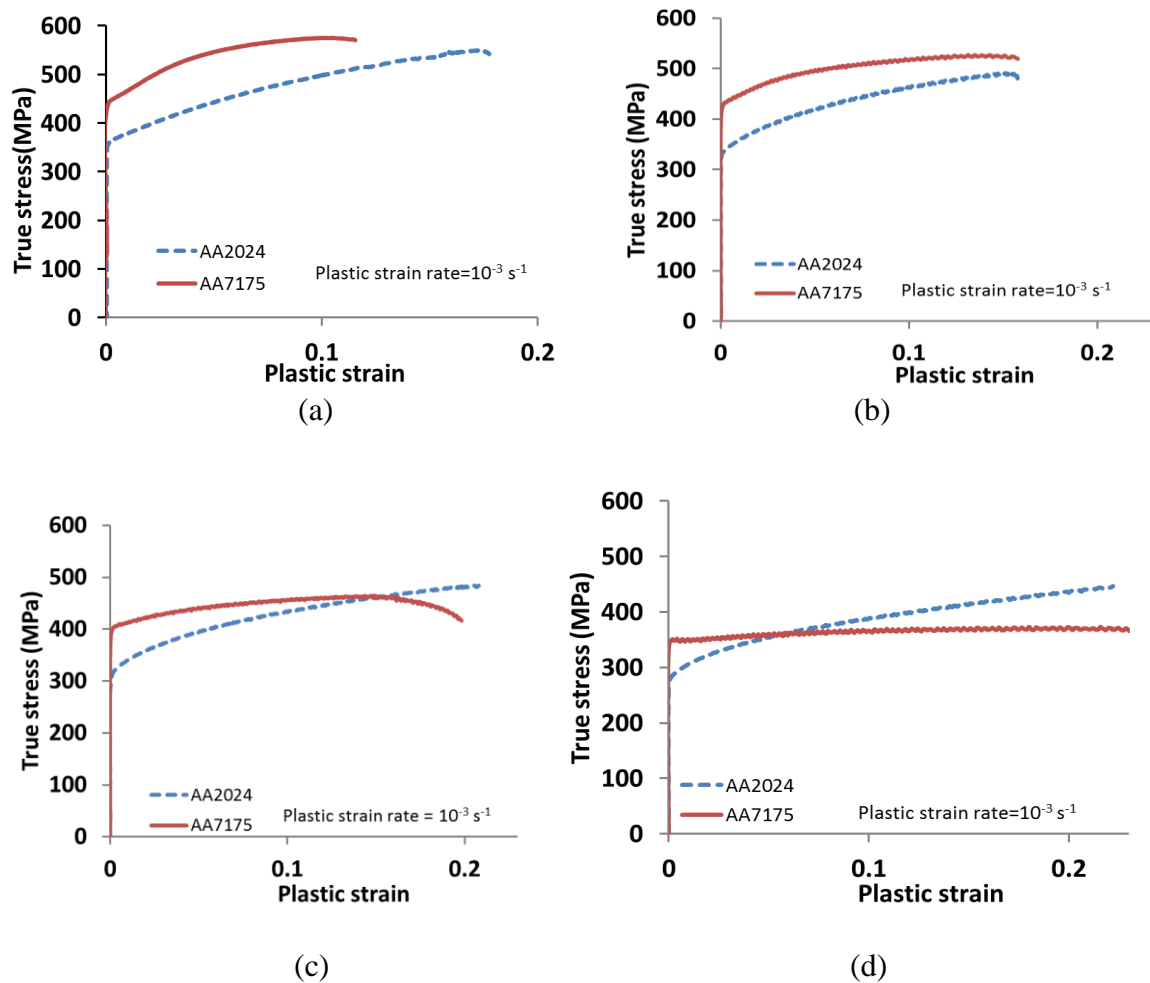


Fig. 2. 68 True stress vs plastic strain for AA2024 and AA7175 at (a) 30°C (b)100°C (c)150°C (d) 200°C

2.5 Conclusion

In the current work, characterization of two types of aluminium alloys which are AA2024 and AA7175 has been studied by carrying out a large number of experiments at different strain rates and temperatures. For the quasi static strain rate considered, both alloys do not show significant effect. Both alloys do not show the significant effect at higher strain rate considered which are 2200 s^{-1} and 4500 s^{-1} as well. However the comparison with quasi static and dynamic range of strain rate reveals the strain rate sensitivity of both alloys where the flow curve is slightly increasing with the increase-of the strain rate at the considered range. Dynamic compression flow curve shows the sudden drop in the stress at plastic strain of 0.2 for AA7175 whereas AA2024 the stress keeps on increasing. The microstructural observation of the dynamic compression specimen reveals the formation of the ASB for AA7175 whereas for AA2024 the microstructure remains quasi homogeneous. This phenomenon explains the sudden drop of the stress in flow curve for AA7175.

AA2024 shows gradual decrease in flow curve at elevated temperature whereas AA7175 shows more drastic decreases in flow stress, especially after 150°C. Fractured of AA7175 depicting cup and cone type failure at 200°C whereas for AA2024 the fracture occurs at 45°. The microstructure of the tension specimen for both alloys depicts increase of voids and coalescence of voids. After the temperature of 150°C the AA7175 depicts larger voids

compared to AA2024. Fractured AA2024 only depicts a small necking effect on the specimens. For AA7175 necking effect can be seen at temperature of 200°C. For AA7175 there seems to be a critical temperature (around 100°C) below which the damage micro-mechanisms are mostly controlled by shear decohesion and above which they are mostly controlled by voiding. This is due to the fact that the void is growing and at 200 °C coalescence of voids can be seen as depicted in Fig. 2. 65 (c).

Analysis on engineering stress flow curve for notched specimen at ambient temperature and 200°C show that the stress increases and the strain at failure decreases with the decreasing of the notch radius, where smaller notch radius indicates higher stress triaxiality. AA2024 shows very small effect of stress triaxiality for specimen with notch radius of 10 mm and 2 mm corresponding to stress triaxiality ratios of 0.475 and 0.572. AA7175 shows the stress for specimen with notch of 10 mm and 2 mm is same due to thermal softening.

Microstructure of the A2024 remains quasi homogeneous after both quasi static and dynamic compression test whereas AA7175 depicts zones of weakly heterogeneous deformation for quasi static compression and ASB for dynamic compression. Dynamic shear compression specimen shows shear Induced Mode II failure for both alloys on Meyer shape specimens and combination of shear induced Mode II and tension induced Mode I for Couque shape. For dynamic shear compression test, Couque shape specimen evidenced an ASB for AA7175 whereas there was no evidence of ASB on AA2024.

2.6 References

- [1] T. Dursun and C. Soutis, "Recent developments in advanced aircraft aluminium alloys," *Mater. Des.*, vol. 56, pp. 862–871, 2014.
- [2] Starke E.A. Jr and Staley J.T., "Application of modern aluminium alloys to aircraft," *Pergamon*, vol. 32, pp. 131–172, 1996.
- [3] E. Roux, P. Longère, O. Cherrier, T. Millot, D. Capdeville, and J. Petit, "Analysis of ASB assisted failure in a high strength steel under high loading rate," *Mater. Des.*, vol. 75, pp. 149–159, 2015.
- [4] J. A. Van Stone, R.H., Cox, T.B., Low, J.R., Psioda, "Microstructural aspects of fracture by dimple rupture," *Int. Met. Rev.*, vol. 30, pp. 157–179, 1985.
- [5] M. N. . Garrison, W M, "Ductile fracture," *J. Phys. Chem. Solids*, vol. 48, pp. 1035–1074, 1987.
- [6] P. Longère, S. Bhogaraju, and D. Craciun, "Void collapse/growth in solid materials under overall shear loading," *Mech. Res. Commun.*, vol. 69, pp. 1–7, 2015.
- [7] A. L. Gurson, "Continuum Theory of Ductile Rupture by Void Nucleation and Growth: Part I—Yield Criteria and Flow Rules for Porous Ductile Media," *J. Eng. Mater. Technol.*, vol. 99, no. 1, p. 2, 1977.
- [8] Y. Bao, "Prediction of ductile crack formation in Prediction of ductile crack formation in uncracked bodies," Massachusetts Institute of Technology, 2003.

- [9] M. Achouri, G. Germain, P. Dal Santo, and D. Saidane, "Experimental characterization and numerical modeling of micromechanical damage under different stress states," *Mater. Des.*, vol. 50, pp. 207–222, 2013.
- [10] Y. Bao and T. Wierzbicki, "On fracture locus in the equivalent strain and stress triaxiality space," *Int. J. Mech. Sci.*, vol. 46, no. 1, pp. 81–98, 2004.
- [11] J. Peirs, P. Verleysen, J. Degrieck, and F. Coghe, "The use of hat-shaped specimens to study the high strain rate shear behaviour of Ti-6Al-4V," *Int. J. Impact Eng.*, vol. 37, no. 6, pp. 703–714, 2010.
- [12] Y. B. Bradley Dodd, *Introduction to Adiabatic shear localization*, Revised Ed. Imperial College Press, 2015.
- [13] C. Zener and J. H. Hollomon, "Effect of strain rate upon plastic flow of steel," *J. Appl. Phys.*, vol. 15, no. 1, pp. 22–32, 1944.
- [14] J. Dorneval, Richard & Pierre Ansart, "Adiabatic Shearing: Influence of Predeformation.. Journal de Physique (Paris), Colloque. 46. 299-306.," *J. Phys. Paris*, vol. 46, pp. 299–306, 1985.
- [15] A. Marchand and J. Duffy, "an Experimental-Study of the Formation Process of Adiabatic Shear Bands in a Structural-Steel," *J. Mech. Phys. Solids*, vol. 36, no. 3, p. 251-, 1988.
- [16] C. Mazeau, L. Beylat, P. Longere, and P. F. Louvigne, "On the quantitative evaluation of adiabatic shear banding sensitivity of various titanium alloys," *J. Phys. IV JP*, vol. 7, pp. 429–434, 1997.
- [17] S. -C. Liao and J. Duffy, "Adiabatic shear bands in a Ti-6Al-4V titanium alloy," *J.Mech.Phys.Solids*, vol. 46, no. 11, pp. 2201–2231, 1998.
- [18] C. Froustey, I. Panteleev, E. Lyapunova, and O. Naimarkb, "Defect induced shear instability and ASB failure in metals," vol. 2, pp. 1959–1966, 2016.
- [19] X. Wu, L. Li, W. Liu, S. Li, L. Zhang, and H. He, "Development of adiabatic shearing bands in 7003-T4 aluminium alloy under high strain rate impacting," *Mater. Sci. Eng. A*, vol. 732, no. March, pp. 91–98, 2018.
- [20] J. D. Seidt and A. Gilat, "Plastic deformation of 2024-T351 aluminium plate over a wide range of loading conditions," *Int. J. Solids Struct.*, vol. 50, no. 10, pp. 1781–1790, 2013.
- [21] G. Chen, L. Lu, C. Ren, and X. Ge, "Temperature dependent negative to positive strain rate sensitivity and compression behavior for 2024-T351 aluminium alloy," *J. Alloys Compd.*, vol. 765, pp. 569–585, 2018.
- [22] N. J. Edwards, W. Song, S. J. Cimpoeeru, D. Ruan, G. Lu, and N. Herzig, "Mechanical and microstructural properties of 2024-T351 aluminium using a hat-shaped specimen at high strain rates," *Mater. Sci. Eng. A*, vol. 720, no. February, pp. 203–213, 2018.
- [23] G. Z. Quan, K. W. Liu, J. Zhou, and B. Chen, "Dynamic softening behaviors of 7075

- aluminium alloy," *Trans. Nonferrous Met. Soc. China (English Ed.)*, vol. 19, no. SUPPL. 3, pp. s537–s541, 2009.
- [24] J. H. Kim, D. H. Kim, and S. I. Moon, "Determination of Dynamic Fracture Toughness Using Strain Measurement," *Key Eng. Mater.*, vol. 261–263, pp. 313–318, 2004.
- [25] P. W. Bridgman, *Studies in large plastic flow and fracture*. New York: McGraw-hill, 1952.
- [26] Y. Bai, X. Teng, and T. Wierzbicki, "On the Application of Stress Triaxiality Formula for Plane Strain Fracture Testing," *J. Eng. Mater. Technol.*, vol. 131, no. 2, p. 021002, 2009.
- [27] M. S. Meyer LW, *Critical adiabatic shear strength of low alloy steel under compressive loading*. Marcel Decker Inc, New York, 1986.
- [28] H. Couque, "A hydrodynamic hat shape specimen to investigate pressure and strain rate dependence on adiabatic shear band formation," *J. Phys. IV*, vol. 110, pp. 423–428, 2003.
- [29] H. Kolsky, "An investigation of the mechanical properties of materials at very high rates of loading," *Proc. Phys. Soc.*, vol. 62, pp. 676–700, 1949.
- [30] M. A. Kaiser, "Advancements in the Split Hopkinson Bar Test," Virginia Polytechnic Institute and State University, Blacksburg Virginia, 1998.
- [31] B. S. Weinong W. Chen, *Split Hopkinson(Kolsky) Bar*. Springer, 2011.

3. Crack arrest capabilities of AA2024 and AA7175 aluminium alloys under impact loading

Abstract. This chapter presents the experimental investigation of the crack arrest capability under impact loading of two types of aluminium alloys that are mainly used in the field of aeronautics, viz. AA2024 and AA7175. Impact tests were carried out by using gas launcher on the edge of double notched plates made of the aluminium alloys. A range of impact speeds was applied from 100 m.s^{-1} to 230 m.s^{-1} . The two alloys show different crack arrest capabilities and failure modes under impact loading. Further analysis on fractured surface reveals that the failure occurs under combination of opening Mode I and shearing Mode II for AA2024 and predominant shearing Mode II for AA7175. Nano-indentation tests were done in a zone containing the tip of the crack to measure the micro hardness field of the surface. Under high loading rate there is evidence of adiabatic shear banding formation for AA7175 which leads to premature failure of the material whereas on the other hand there is no evidence of adiabatic shear band on AA2024.

Table of contents

3.1	Introduction	62
3.2	Experimental procedure	64
3.2.1	Materials under consideration	64
3.2.2	Impact tests	64
3.2.3	High speed frame recording	67
3.2.4	Microscopic examination	68
3.2.5	Nano indentation test.....	68
3.3	Results and analysis	70
3.3.1	KW impact test results	70
3.3.2	Kinematic analysis of the crack propagation and arrest.....	72
	Low impact speed (< critical impact speed).....	72
	High impact speed (> critical impact speed)	74
3.3.3	Failure analysis of the impacted plates	78
3.3.3.1	Crack propagation analysis	79
3.3.3.2	Internal crack surface analysis	82
3.3.3.3	Fully fractured surface analysis	84

3.3.3.4	Crack lips analysis	87
3.3.4	Nano-hardness of crack tip surface	88
3.4	Summary	90
3.5	Concluding remarks	94
3.7	References	95

3.1 Introduction

In the design of aeronautical structures, the damage tolerance study takes an important part. According to Federal Aviation Requirement (FAR) and Joint Aviation Requirement (JAR), the aim of damage tolerance is to reduce the effect of failure due to manufacturing defects and service-induced damage that can cause cracks. Damage tolerance is defined as sustainability of structures weakened by defects until the repairing process takes place. In this context, we are here interested in experimentally investigating the crack arrest capability of aeronautical structural materials, viz. AA2024 and AA7175 aluminium alloys, under dynamic overloading as notably encountered during incidents like bird strike, bird ingestion, hail storm, tools fell down during repairing and maintenance process, etc. Crack arrest is indeed of major interest in order to assess the serviceability of crack-containing structures.

In their pioneering works, Kalthoff and Winkler [1] have experimentally studied the failure of impacted double notched plates made of high strength (maraging and Cr-Mo) steels. Depending on the impact speed magnitude and notch dimensions, cracks initiating from the notch tips propagate either at an angle close to 70° wrt the notch direction (low speed, blunt notches, tension mode) or in the direction of the notch direction (high speed, sharp notches, shear mode), see Fig. 3. 1 Kalthoff and Bürgel [2] have carried out the same experiments on double notched plates made of high strength Cr-Mo steel and AA7075 aluminium alloy. They evidenced that for the hard steel, the crack propagation is controlled by tension mode below a critical impact speed and by shear mode above this critical speed – as for the previous work, see above. They however evidenced no critical impact speed for the aluminium alloy which systematically fails under shear mode. This absence of critical impact speed has also been shown by Roux et al. [3] for the ARMOX500T armor steel which is seen to fail under shear mode whatever the impact speed – it is to be noted that the plate geometry and impact conditions used by the authors are slightly different than the ones used by Kalthoff and co-workers. By using single notched plates made of high strength C-300 (maraging) steel, Zhou et al. [4] have shown that when a shear mode-controlled crack arrests inside the structure it may ultimately propagate following an angle with the notch direction, i.e. under tension mode, like in Fig. 3. 2 For their experiments with plates made of Ti-6Al-4V titanium alloy, the only failure mode observed is shear. They conclude that the difference in failure mode is more likely due to the material properties than the specimen geometry. Failure under shear

mode has also been shown in Longère and Dragon [5] on impacted double notched plates made of Ti-6Al-4V titanium alloy.

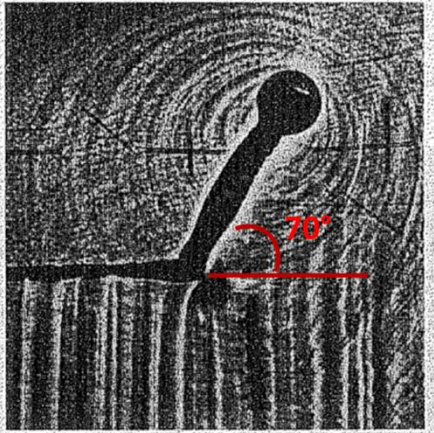


Fig. 3. 1 Mode I crack tip 70° wrt notch direction after [1]

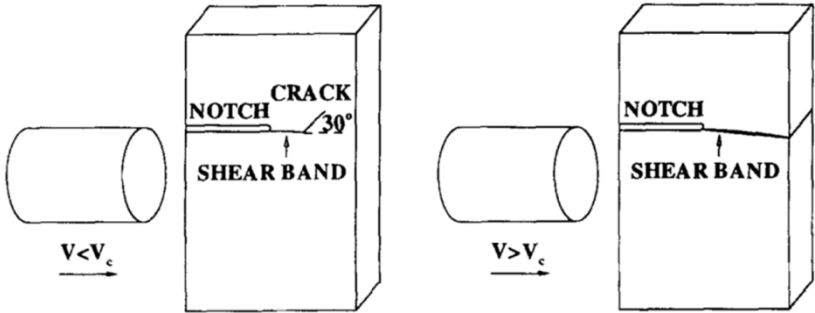


Fig. 3. 2 Asymmetric impact configuration and failure modes after [4]

Tension mode of failure is commonly associated to brittle-like failure whereas shear mode of failure is generally seen to proceed from shear localization in the form of adiabatic shear bands, see Kalthoff and Winkler [1], Kalthoff and Bürgel [2], Roux et al. [3], and Zhou et al. [4]. Yet, in the work by Longère and Dragon [5] no shear band was observed.

Adiabatic shear banding (ASB) is a shear localization process which develops under high loading rate as the result of the competition between hardening and softening mechanism, see e.g. Bai and Dodd [6]. It is the precursor of the ultimate failure. A review of selected constitutive and numerical models aiming at reproducing the ASB-assisted failure can be found in Longère [7]. Failure under ASB in high strength steels and titanium alloys has been evidenced for a long time, see e.g. Zener and Hollomon [8], Dormeval and Ansart [9], Marchand and Duffy [10], Mazeau et al. [11], Liao and Duffy [12]. Evidence of failure under ASB of aluminium alloys seems more recent. For example, Gao et al. [13] and Liang et al. [14] have shown that impacted structures made of AA2519 aluminium alloys may fail under ASB. On the other hand, Yang et al. [15], [16] and Mondal et al. [17] have evidenced ASB as responsible for the failure of impacted structures made of AA7075 aluminium alloys.

The present work aims at experimentally investigating the crack arrest capability under impact loading of two types of aluminium alloys that are mainly used in the field of aeronautics, viz. AA2024 and AA7175. To that purpose, impact tests were carried out using gas launcher on the edge of double notched plates made of the aluminium alloys. A range of impact speeds was applied between 100 m.s^{-1} and 230 m.s^{-1} . The fractured surfaces were observed using optical and scanning electron (SEM) microscopy in view of determining the failure mechanisms. Nano-indentation tests were also carried out in a zone containing the tip of the crack to measure the micro hardness field of the surface. This experimental study allows for comparing the crack arrest capability of the two aluminium alloys under consideration.

The present chapter consists of three main parts. Section 3.2 details the experimental procedure. Section 3.3 presents the results and analysis which are summarized in Section 3.4. Section 3.5 is devoted to the concluding remarks.

3.2 Experimental procedure

In this Section are presented the experimental and observation devices.

3.2.1 Materials under consideration

AA2024 and AA7175 aluminum alloys have been presented and characterised in the previous chapter. From the tension tests which were conducted for both alloys at room temperature and strain rate of 10^{-3} s^{-1} , the yield strength of AA2024 and AA7175 is 342 MPa and 436 MPa respectively.

3.2.2 Impact tests

Kalthoff and Winkler (KW) type impact tests, see Kalthoff and Winkler [1], were carried out by using 6 m-length and 40 mm-inner diameter gas launcher tube using STIMPACT impact facility – the facility consists of 3 gas launchers with complementary performances with inner diameter of 40, 60 and 120 mm, respectively, see Fig. 3. 3, Fig. 3. 4 and Fig. 3. 5. for the experimental set-up. The 20 mm-diameter projectile made of hard steel is placed inside a 40 mm-outer diameter cylinder made of foam, see Fig. 3. 6, whose function is to reduce the friction inside the gas launcher tube. The distance between specimen and launcher is 40 cm.

The target is a $40 \times 82 \times 6 \text{ mm}^3$ -double notched plate made of the material to test, see Fig. 3. 3(c), Fig. 3. 4 and Fig. 3. 5. The 20 mm-length and $300\mu\text{m}$ -width notches were machined by electric discharge machining (EDM). Lines were engraved on the plate side in view of further digital image analysis, see Roux et al. [3].

The schematic view of the specimen and complete system of data acquisition is shown in Fig. 3. 4. Table 3. 1 reports the pressure values and corresponding projectile speeds for 40 mm inner diameter gas launcher.

In the present study, the projectile speed range was from 100 m.s⁻¹ until 230 m.s⁻¹.

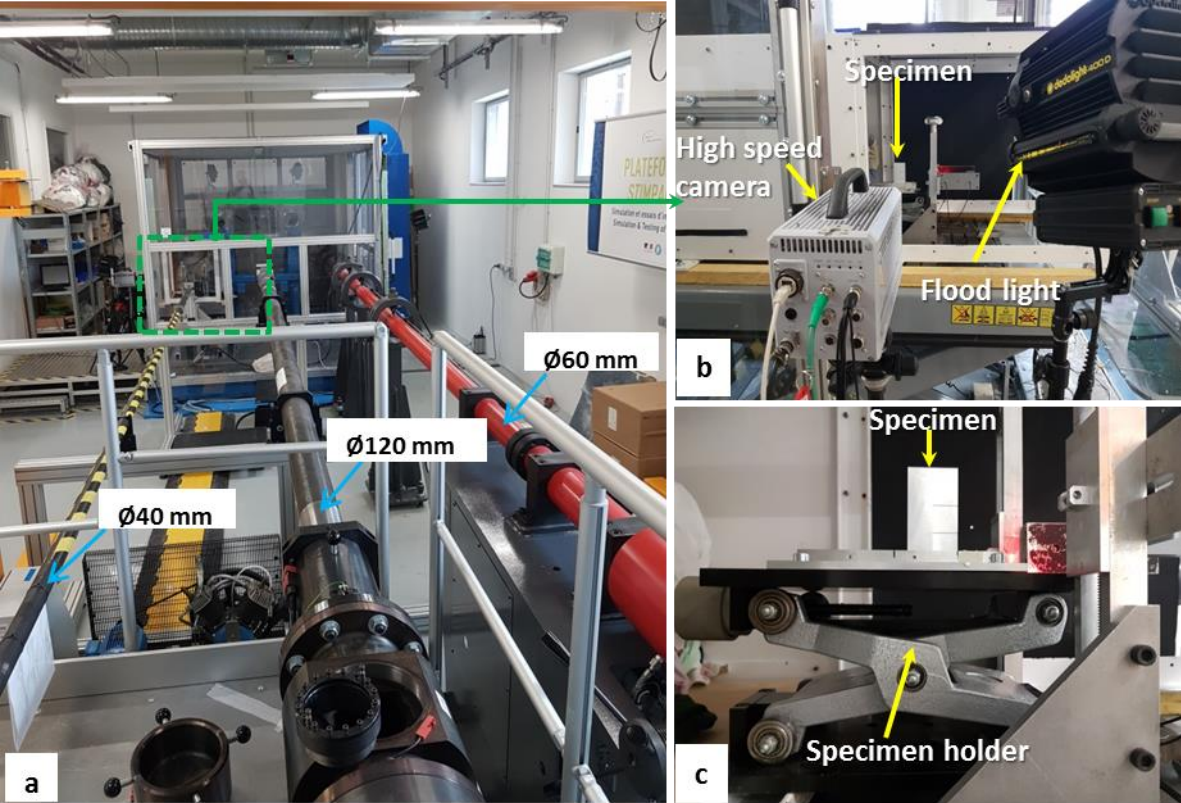


Fig. 3. 3 (a) STIMPACT facility showing the 3 gas guns; (b) Experimental set up; (c) Specimen and its holder

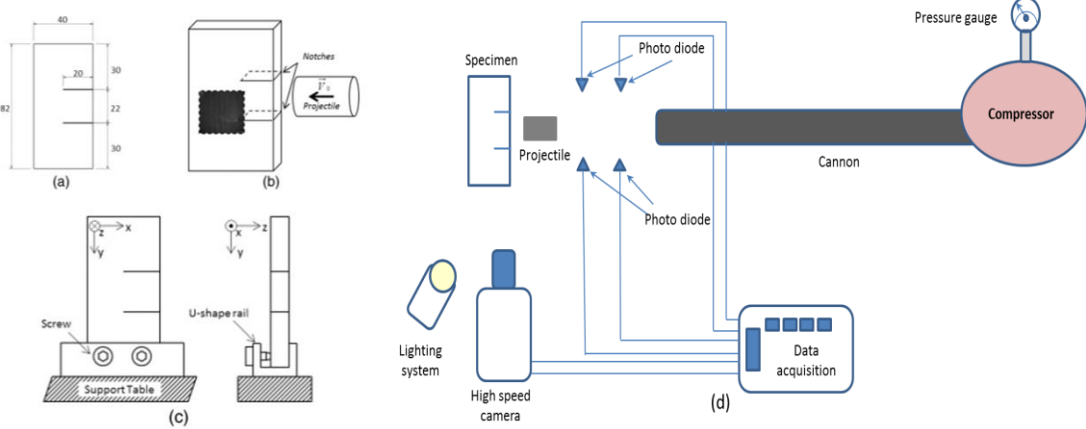


Fig. 3. 4 Schematic view of the impact tests (a) Specimen dimensions (b) Projectile-specimen interaction (c) Plate on its holder [3], (d) Data acquisition system

The projectile was set to impact the region in between the two notches by using laser alignment method. Laser alignment is a method consisting in directing a laser point from the end of gas launcher tube to the target point on the specimen. The projectile will hit the target at that particular point as set by the laser pointer. The projectile will travel along the tube and its speed will be measured by 2 pairs of photodiodes, 2 emitters and 2 receivers see Fig. 3. 5. As the projectile cuts the photodiodes beam, the changes in the signal recorded by the high data acquisition system allows to determine the speed of the projectile. The signals of the photodiodes were used to trigger the high speed camera.

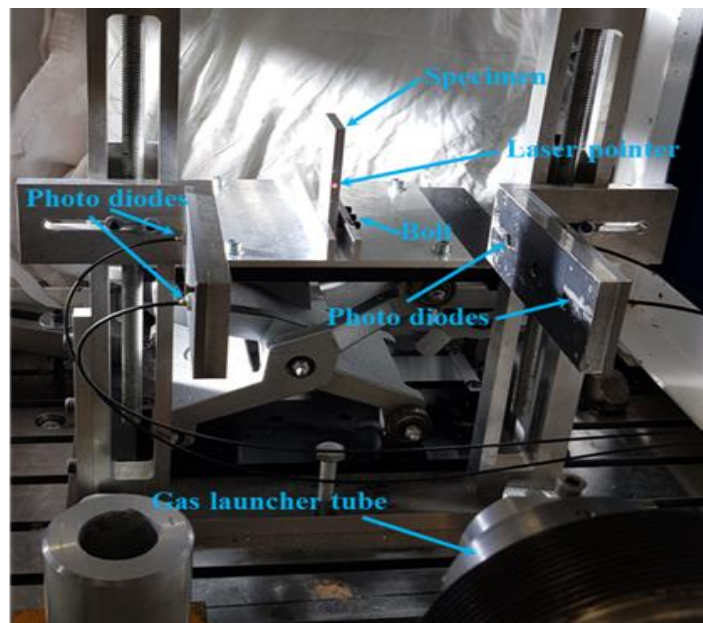


Fig. 3. 5 Specimen alignment and projectile speed measurement



Fig. 3. 6 Steel projectile inside foam housing

Table 3. 1 Pressure and resulting projectile speed for 40 mm-inner diameter gas launcher

Pressure (bar)	Mass of projectile and foam (g)	Projectile speed (m.s ⁻¹)
1.4	80.5	100
1.5	80.5	111
1.6	80.5	120
1.8	80.5	133
3.0	80.5	164
9.2	80.5	230

3.2.3 High speed frame recording

A high speed camera was used to capture the image during the interaction between the projectile and the plate and follow the crack propagation and arrest.

The Photron SA5 camera was set to capture image at 10^5 frames per second (fps) at 320×192 pixel² spatial resolution. Lighting was provided by Dedolight HMI floodlight with power of 400W.

The following steps explain the calibration of the distance between two points of the recorded image. For the present explanation, the image was captured at time 0.43942 s. The yellow cursor was placed at the upper part of notch tip and green cursor placed at the beginning of the notch, see Fig. 3. 7. The pixel distance for horizontal axis will be the same value which is 0051. The value for horizontal axis is 0110 for the yellow cursor and 0207 for green cursor. So the differences in the horizontal distance are 97 pixels.

Knowing that the length of the notch is 20 mm, the ratio of distance in pixel is converted to millimeter and applied as input value in distance calibration window in Photron software. Once the calibration is done, the distance between any two points in Photron windows can be determined. By applying this technique, the speed of the projectile just before impacting the plate can also be determined.

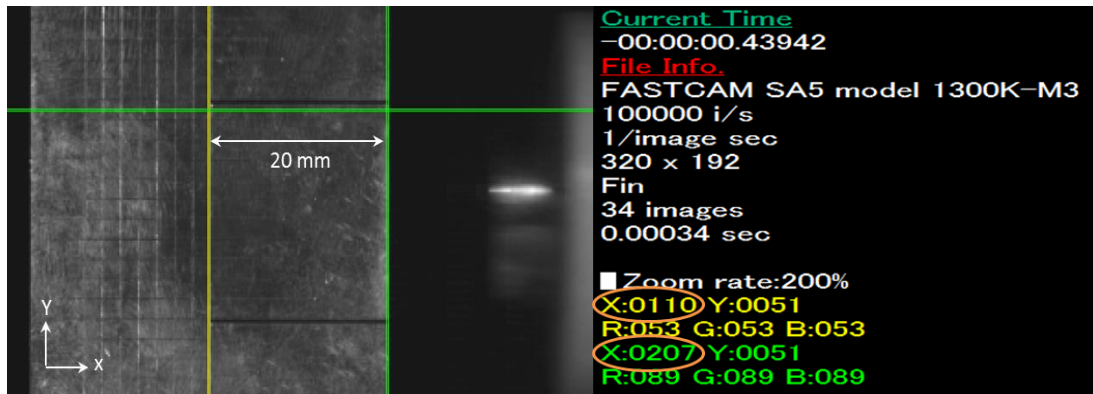


Fig. 3. 7 Distance calibration in Photron software

3.2.4 Microscopic examination

Fractography analyses were performed to observe the micro-mechanisms controlling the crack propagation and arrest.

To that purpose, optical microscope, Olympus GX71, and scanning electron microscope (SEM), Philips XL30ESEM, were used to analyse the specimens after impact. The surface of the fully fractured region was also observed using SEM to investigate the mechanisms that cause failure. For the specimens which were fractured into three parts, the lips of the cracks were observed by using optical microscope in order to identify the existence/absence of band of shear localization.

Microscopic analyses of the specimens were carried out using four different methods. First method (M1) consists in observing without grinding, polishing or etching. Second method (M2) consists in observing after grinding by using sand paper with different successive grain sizes. Third method (M3) consists in observing after grinding with sand paper and polishing with diamond particle fluids. Fourth method (M4) consists in grinding with sand paper, polishing with diamond particle fluids and etching the specimen. The specimens were etched during 10 to 15 second by acid consisting of 10% of hydrochloric acid, 10% of nitric acid, 5% of hydrofluoric acid and 75% of water.

3.2.5 Nano indentation test

Nano indentation tests were carried out to determine the nano-hardness field around the crack tip in view of identifying potential local microstructural changes.

Fig. 3. 8 shows the nano-indentation apparatus which is available at the Laboratory. The model of this machine is NHT2 and made by CSM Instruments. This model uses compact platform type known as CPX.

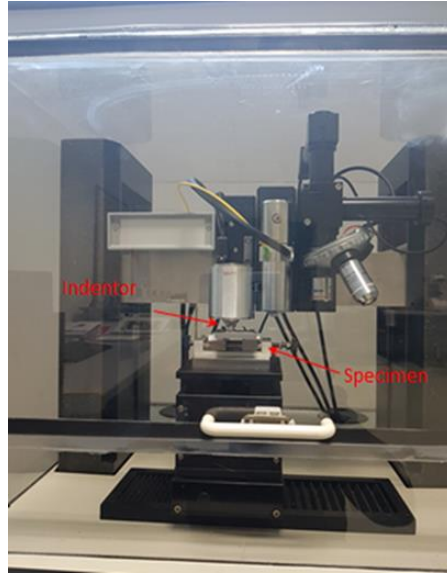


Fig. 3. 8 Nano indentation test apparatus

Berkovich three sided pyramid type diamond indenter was used to perform the indentation, see Fig. 3. 9. A regular map of indentation tests was done around the crack tip. Indentation force is 300 mN and the depth of indent is 2 μ m. 400 indentations within the square zone were made for determining the nano-hardness field. Distance between each indentation is 100 μ m. The indentation begins at the tip of crack, covering an area of 2x2 mm². Indentation hardness given in MPa can be converted by using (3.1)

$$HV = \frac{H(MPa)}{10.8} \quad (3.1)$$

where HV is Vickers hardness and H is nano-hardness. It is to be noted that the formula given here is an estimate and may be varying according to the type of the materials. Furthermore nano-indentation and micro-indentation have different depths of the indenter which may lead to different hardness values due to influence of the dislocation and interaction between crystals. Nano-indentation is suitable for measuring the surface hardness whereas the micro-indentation is suitable for measuring the hardness of the bulk material. The surface of the specimen was prepared by applying method M3 before nano-indentation process carried out.

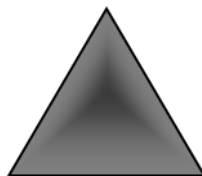


Fig. 3. 9 Berkovich three side pyramid-type indenter

The principle of the nano indentation tests is depicted in Fig. 3. 10. The impacted specimen is indented at the tip of the crack over an area of $2 \times 2 \text{ mm}^2$. The nano-hardness mapping is obtained from the data analysis and visualization software Gwyddion 2.47.

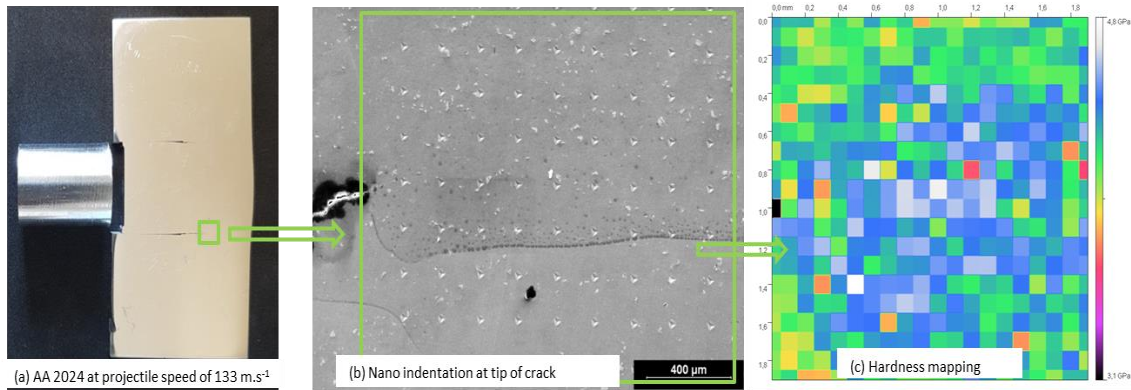


Fig. 3. 10 Principle of the nano indentation tests in a region containing the crack tip (here for AA 2024 - 133 m.s^{-1})

3.3 Results and analysis

The failure analysis is performed in this Section. The chronology of the interaction between the plate and the projectile is in particular discussed.

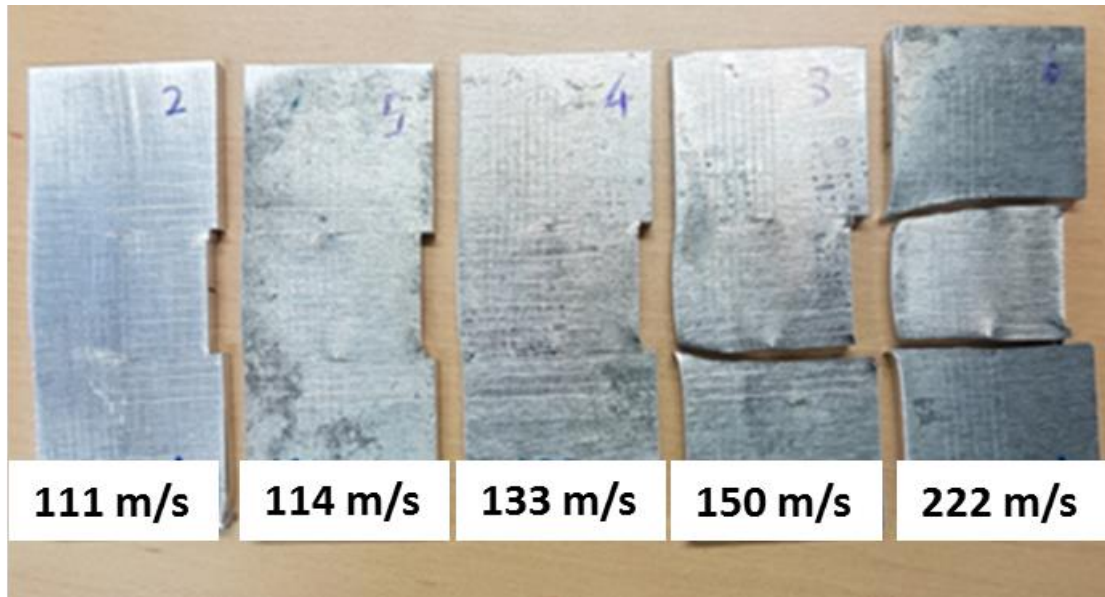
3.3.1 KW impact test results

The pictures of the post-mortem specimens after different projectile speeds are shown in Fig. 3. 11. It is shown that the fracture occurs at different speeds leading to different failure states. The plate ultimately fractures in three parts as the result of the symmetric development of cracks initiated from both notches and propagating in a direction quasi collinear to the notch direction – the fracture of the plate in two parts is probably due to unstable crack propagation which may be magnified by possible slight misalignment between the projectile trajectory and the normal of the plate edge. Each test was carried out once for each configuration

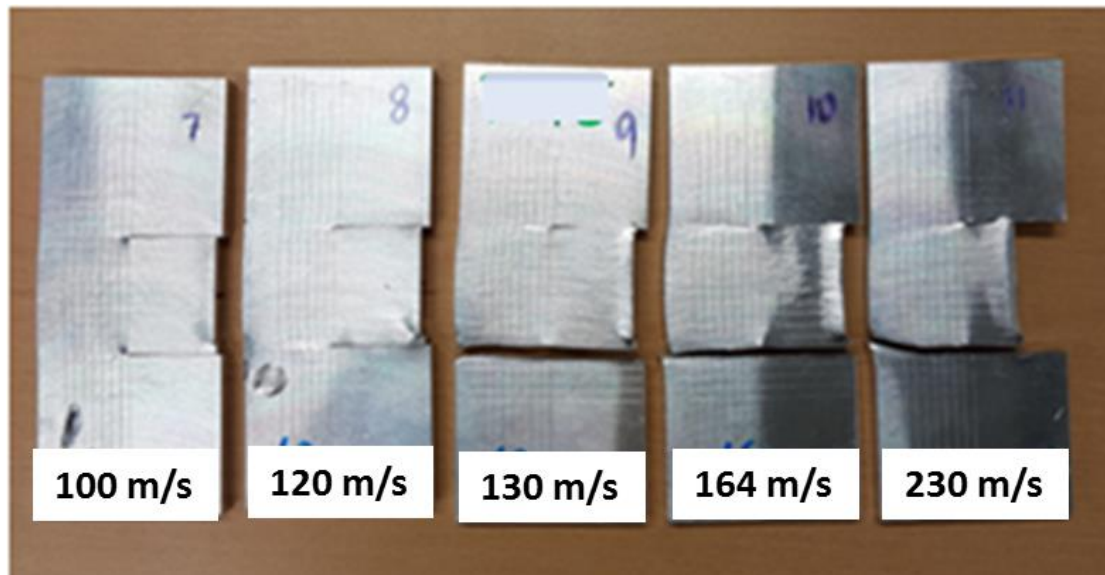
For both alloys, the different types of damage involved by the projectile impact speed are reported in Table 3. 2 and Table 3. 3 in terms of speed and speed range, respectively. In the range from 100 to 120 m.s^{-1} , no significant damage is observed for both alloys. For the range of 121 to 140 m.s^{-1} AA 7175 is subject to partial fracture. For the range of 141 to 160 m.s^{-1} and 161 to 180 m.s^{-1} both alloys are subject to partial fracture. For the range of 181 to 230 m.s^{-1} , AA 2124 was fully fractured at upper and lower notches whereas AA 7175 was only partially fractured.

For AA2024, at impact speed of 111 m.s^{-1} , 114 m.s^{-1} and 133 m.s^{-1} , the crack arrests inside the structure. From 150 m.s^{-1} , the specimen is split in two or three parts.

For AA7175 the crack propagates and arrests inside the structure at impact speed of 100 m.s^{-1} and 120 m.s^{-1} . At impact speed of 130 m.s^{-1} the plate fully fractures. The critical impact speed at complete fracture is higher for AA2024 (close to 150 m.s^{-1}) and lower for AA7175 (close to 130 m.s^{-1}).



(a) AA 2024



(b) AA 7175

Fig. 3. 11 Post-mortem specimens after impact at various speeds

Table 3. 2 Failure of specimen at different speeds

Speed(m.s ⁻¹)	100	111	114	120	130	133	150	164	222	230
Material										
AA 2024		N	N			N	PF		FF	
AA 7175	N			N	PF			PF		PF

N-No damage PF-Partial Fracture FF- Fully Fracture

Table 3. 3 Failure of specimen at different ranges of speeds

Speed range(m.s ⁻¹)	100-120	121-140	141-160	161-180	181-230
Material					
AA 2024	N	N	PF	PF	FF
AA 7175	N	PF	PF	PF	PF

N-No damage PF-Partial Fracture...FF-Fully Fracture

3.3.2 Kinematic analysis of the crack propagation and arrest

In this section, an example is presented for low speed where the crack arrests inside the material and for higher speed where the specimen is split into three parts. High-speed frame post-processing was performed to analyze the crack propagation and arrest during the plate-projectile interaction. The speed of the projectile estimated from the frames post-processing is seen to be close to the value measured using the photo diodes, see Fig. 3. 5.

The Photron software allows for importing the video of the plate-projectile interaction that was recorded earlier by using Photron high speed camera. The imported image calibrated by measuring the known distance between two points as explained earlier in the subsection 3.2.3. Once the calibration process is performed, calculations can be done by applying linear equation formula to estimate the speed of the crack tip and ASB propagation.

Due to insufficiently high frame rate and spatial resolution of the camera used, digital image analysis using the lines engraved on the plate side was not possible.

Low impact speed (< critical impact speed)

The plate-projectile interaction observed through the frames recorded by the high speed camera at one frame every 10 μs can be decomposed into different steps. Examples of chronology are given for AA2024 and AA7175 in Fig. 3. 12 and Fig. 3. 13 respectively.

According to Fig. 3. 12 for AA2024,

- between t=0 and t=30μs: a compression wave propagates throughout the part of the plate impacted by the projectile leading to the formation of a shear wave at both notch tips; notches are open and cracks initiate symmetrically (i) from the upper part of lower notch tip and (ii) from the lower part of upper notch tip.
- between t=30μs and t=120μs: due to Poisson-like effect the compression of the part of the plate impacted by the projectile leads progressively to the closure of the gap

between notch lips; for the upper notch, the lower lip thus hits the upper lip yielding the propagation of a compression wave in the part of the plate above the upper notch; the compression wave propagates towards the upper free edge of the plate; the symmetric phenomenon occurs for the lower notch; meanwhile, cracks initiated from the notch tips slightly propagate under predominant shear Mode II, i.e. along a direction close to the notch direction.

- between $120\mu\text{s}$ and $t=150\mu\text{s}$: the gap closure-induced compression waves reflecting from upper and lower free edges of the plate in the form of tension waves cause a re-opening of the gap between notch lips and tension stresses on crack lips; cracks propagate or arrest under combined shear Mode II and opening Mode I.
- beyond $t=150\mu\text{s}$: notches undergo cyclic gap closures and openings as cracks undergo cyclic compression and tension superposed on shear.

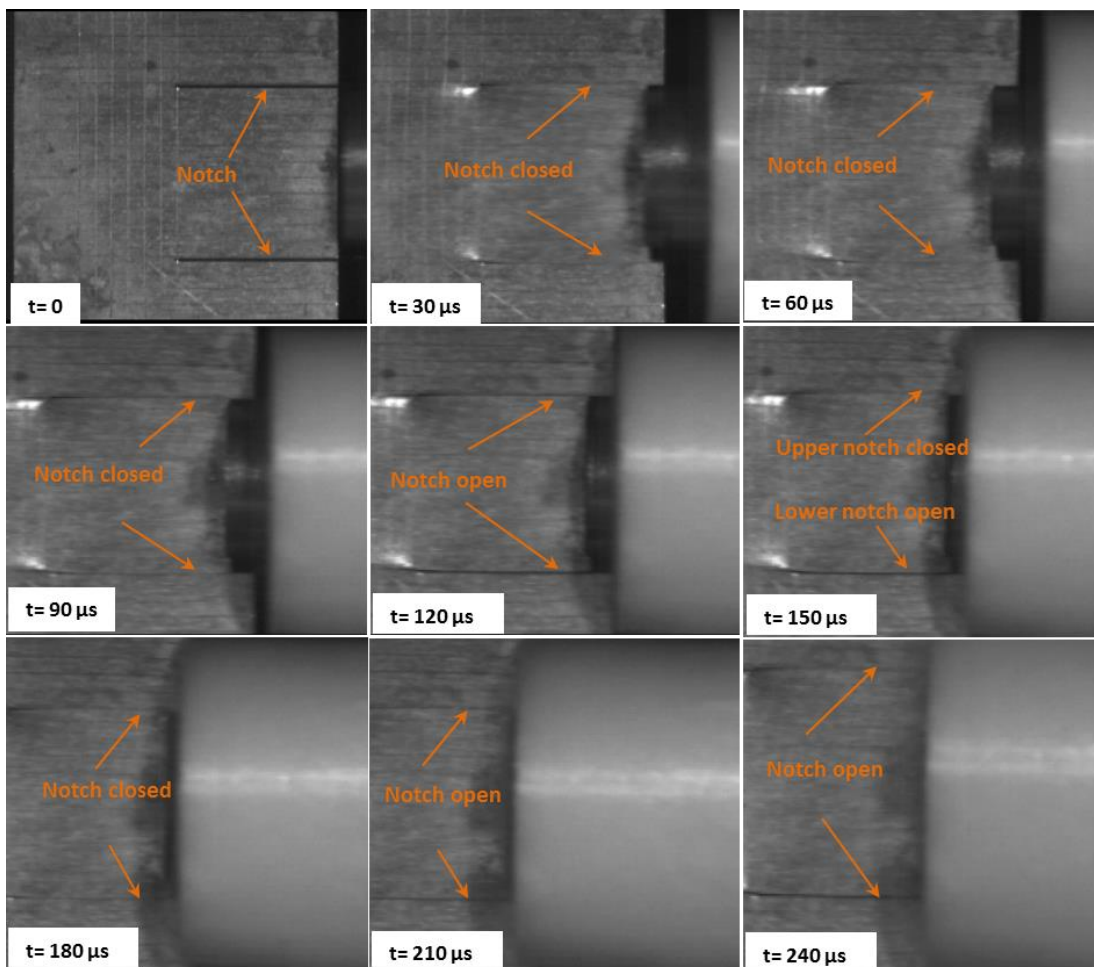


Fig. 3. 12 Kinematics of the plate-specimen interaction. AA2024 - $114\ \text{ms}^{-1}$

The same scenario, which is depicted in Fig. 3. 14, is observed in Fig. 3. 13 for AA7175. Fig. 3. 14(a) schematically depicts the projectile and plate before interaction. In Fig. 3. 14(b), it is shown that compression wave was generated inside the impacted part of the plate. This compression wave was transformed into a predominant shear wave at the notch tip. Due to Poisson effect-induced gap closure, a compression wave is generated which reflects as tension wave from the free edge of the plate, see Fig. 3. 14(c) [5].

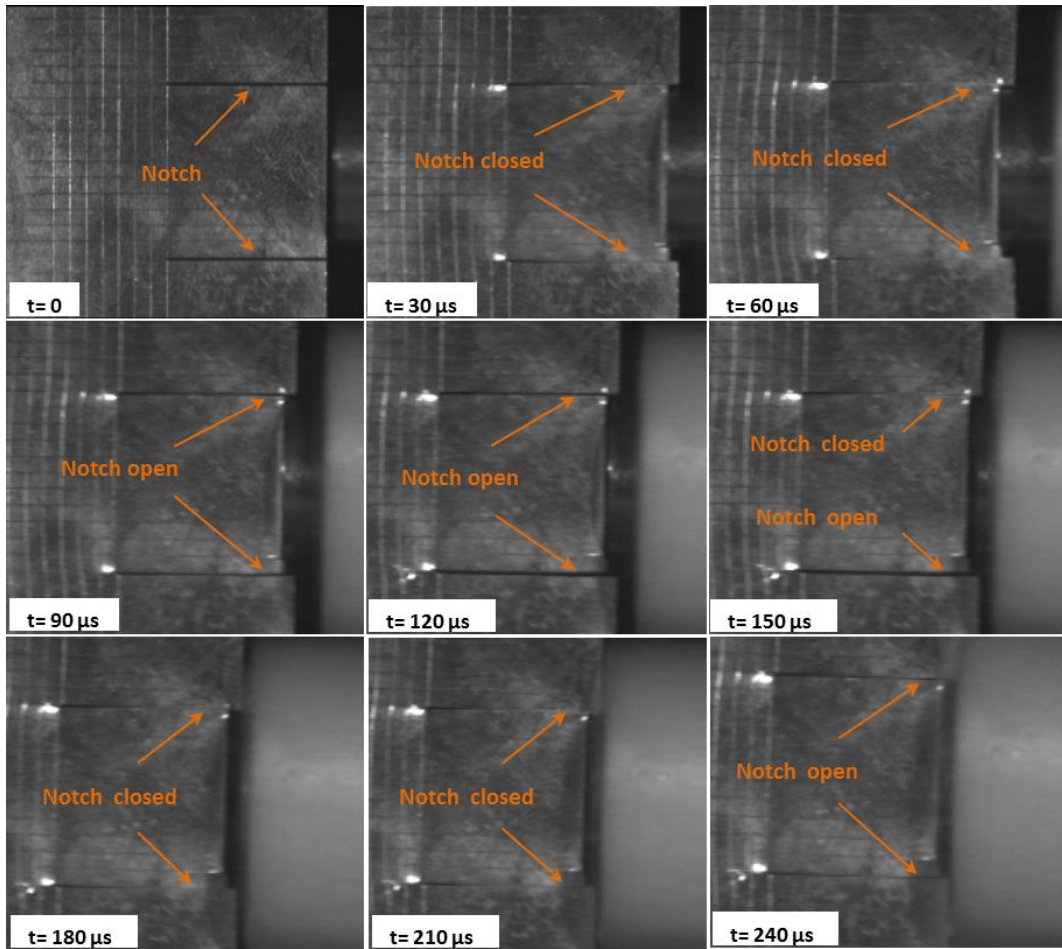


Fig. 3. 13 Kinematics of the plate-specimen interaction. AA7175 - 100 ms^{-1}

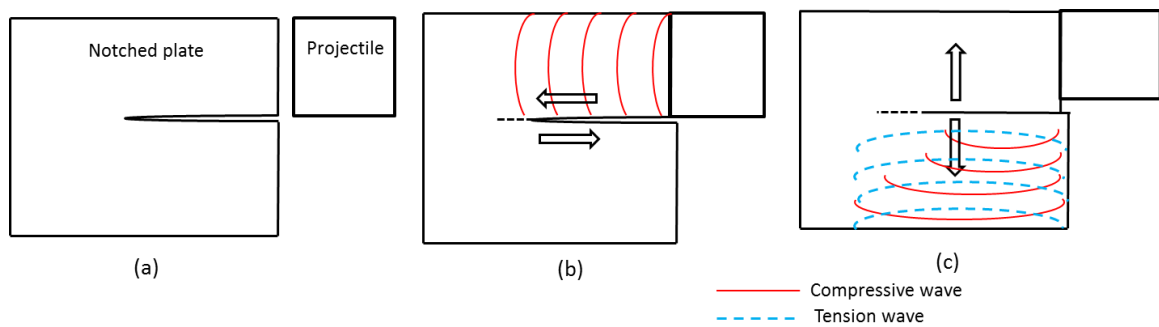


Fig. 3. 14 Principle of wave interactions. (a) Configuration before impact accounting for symmetry. (b) Compression wave induced in the specimen part impacted by the projectile resulting in shear wave at the notch tip (c) Tension wave resulting from the reflection

High impact speed (> critical impact speed)

For impact speeds greater than the critical impact speed, specimens are fully fractured into three parts (or two parts). Considering the lower part of the specimen, further observation can be done.

Fig. 3. 15 depicts the chronology for AA2024 plate at impact speed of $222\text{m}\cdot\text{s}^{-1}$ with one frame every $10\ \mu\text{s}$. The following steps can be observed:

- between $t=0$ and $t=17.4\mu\text{s}$: a compression wave propagates throughout the part of the plate impacted by the projectile leading to the formation of a shear wave at the notch tips; the crack initiates.
- between $t=17.4\ \mu\text{s}$ and $t=37.4\mu\text{s}$: due to Poisson-like effect the compression of the part of the plate impacted by the projectile leads progressively to the closure of the gap between notch lips. For the lower notch the upper lip thus hits the lower lip yielding the propagation of a compression wave of the part of the plate above the lower notch; the compression wave propagates towards the lower free edge of the plate.
- between $t=37.4\ \mu\text{s}$ to $t=47.4\ \mu\text{s}$ the crack propagates and measures $6.4\ \text{mm}$
- the crack reaches the length of 16.2 at $t=57.4\ \mu\text{s}$

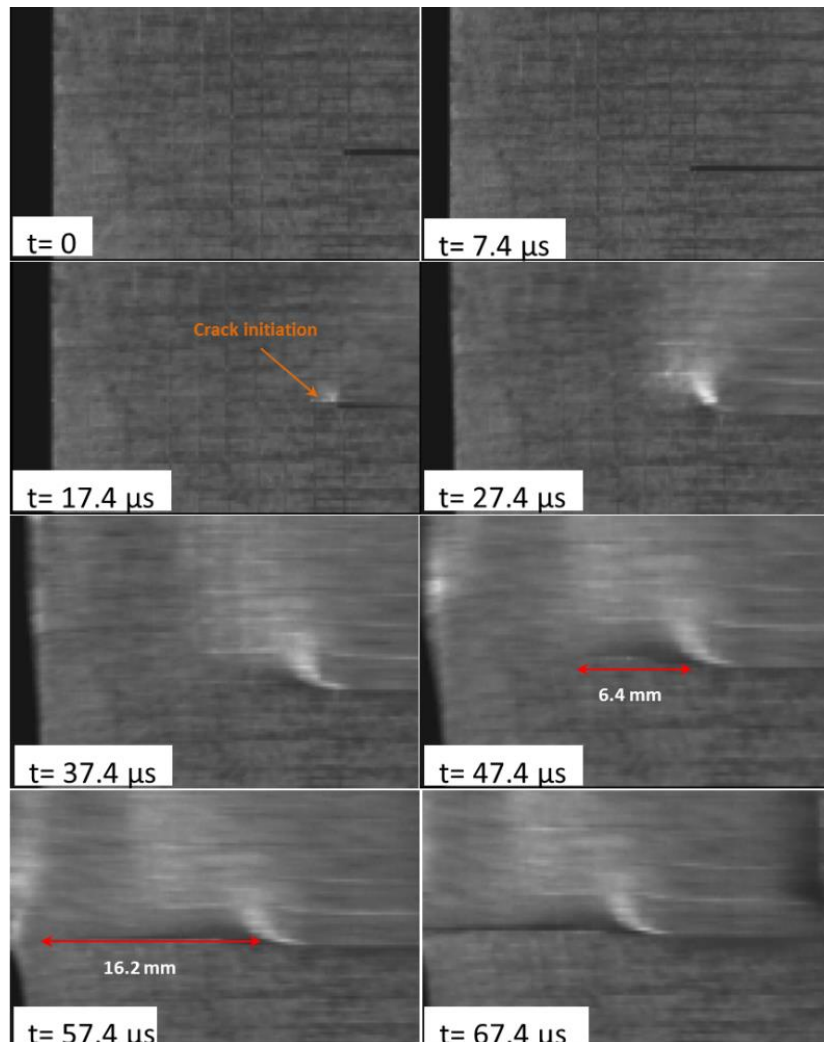


Fig. 3. 15 Lower part of the AA 2024 plate during impact at $222\ \text{ms}^{-1}$

Coarse estimate of the crack tip speed value can be done by applying linear motion equation,

$$v = \frac{\Delta d}{\Delta t} \quad (3.2)$$

where v , d and t are speed, displacement and time respectively.

Fig. 3. 16 shows the evolution of crack length and crack tip speed for AA 2024.

- At $t=47.4\mu\text{s}$ crack length is 6.4 mm and at $t=57.4\mu\text{s}$ crack length is 16.2 mm.
- At $t=47.4\mu\text{s}$ crack tip speed is $640\text{ m}\cdot\text{s}^{-1}$ and at $t=57.4\mu\text{s}$ crack speed is $980\text{ m}\cdot\text{s}^{-1}$.

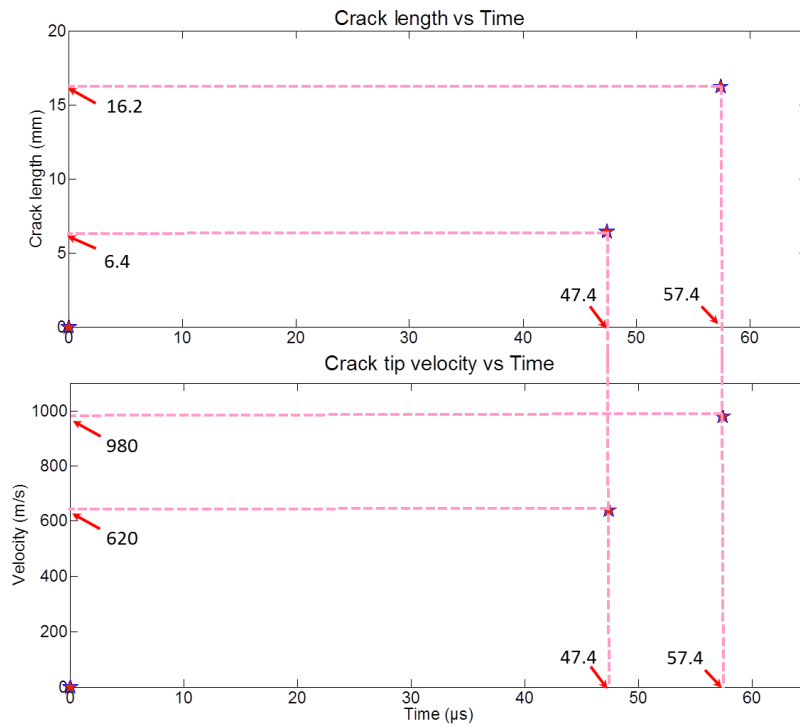


Fig. 3. 16 Crack length and crack tip speed for AA 2024

Fig. 3. 17 depicts the chronology for AA7175 plate at impact speed of $230\text{ m}\cdot\text{s}^{-1}$ with one frame every $10\mu\text{s}$. The same observation as discussed for AA 2024 in Fig. 3. 15 was observed except for the formation of white band as precursor of the crack and which does not exist for AA 2024.

- At $t=55.6\mu\text{s}$ a white band appears at notch tip and propagates about 5.2 mm. This white band further propagates to the left collinearly to the notch direction then with an angle of 15° upwards.
- the total length of this white band is about 12.4 mm at $t=65.6\mu\text{s}$.
- between $t=75.6\mu\text{s}$ and $85.6\mu\text{s}$ the crack is indeed propagating but cannot be seen clearly not only due to less resolution but also due to the possible Poisson-like effect where the compression of the part of the plate impacted by the projectile leads progressively to the closure of the gap between notch lips.

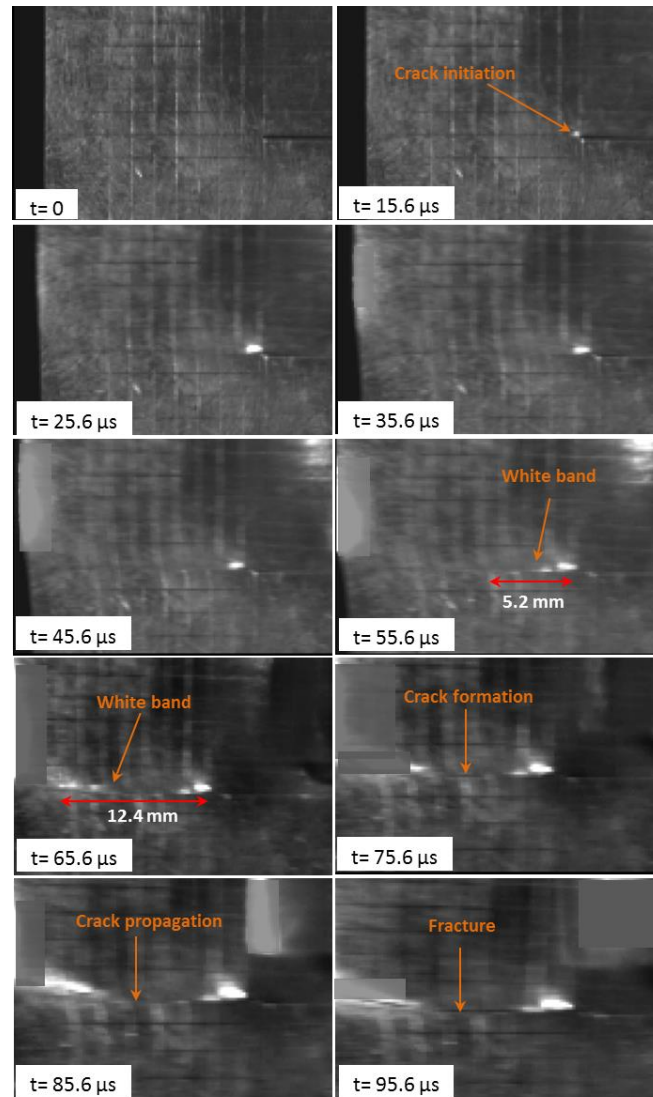


Fig. 3. 17 Lower part of the AA 7175 plate during impact at 230 m.s⁻¹

The average speed of the white band propagation in AA 7175 for the duration of 10 μ s can be estimated by applying (3.2). Fig. 3. 18 shows the white band length and its speed evolutions.

- At t=55.6 μ s the length of white band is 5.2 mm and the speed of the white band is 520 m.s⁻¹
- At t=65.6 μ s the length of white band is 7.2 mm and its speed is 720 m.s⁻¹
-

Fig. 3. 19 shows the evolution of crack length and crack tip speed.

- At t= 76 μ s the crack length is about 6 mm and its speed is 600 m.s⁻¹.
- At t= 86 μ s is estimated about 800 m.s⁻¹ respectively.

For comparison, studies by Roux et al. [3] shows that the crack tip speed and white band speed reaches 260 m.s⁻¹ and 650 m.s⁻¹ respectively for impacted speed of 156 m.s⁻¹ on high strength ARMOX500T steel. It is reminded that the values of white band and crack speeds, while being approximate, give information allowing for comparing both AA2024 and

AA7175. The maximum values of crack speed and white band speed are reported in Table 3.5. From the crack propagation analysis for the specimen at speeds below the critical speed and above critical speed, there are some issues that need to be considered concerning the compressive wave during the impact. The impact of the projectile onto the plate edge will generate a compressive wave which has two effects: first, the transformation of the wave into predominant shear wave at notch tip see Fig. 3. 14(b), and second, the propagation of a tension wave in the direction perpendicular to the impact axis, see Fig. 3. 14 (c). According to Longère and Dragon [5], this scenario may repeat several times depending on loading intensity, projectile speed and length. This may explain the crack bifurcation observed in AA7075 by Kalthoff and Bürgel [2], see Fig. 3. 11 of the paper and Fig. 3. 17 of the present manuscript.

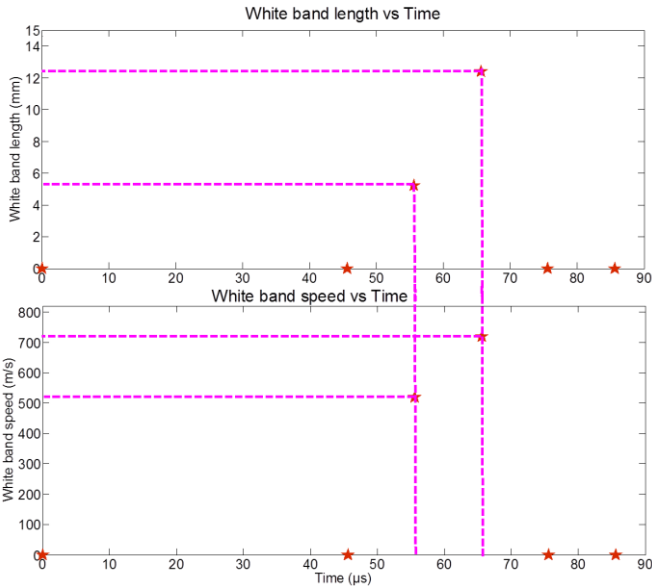


Fig. 3. 18 White band length and white band speed for AA 7175

3.3.3 Failure analysis of the impacted plates

In this study fractography analyses were done on four different regions around the cracks: first was on the crack itself, second was inside the crack surface, third was on fully fractured surface and fourth was on the lip of the fully fractured surface. Fractography analysis were performed by applying four different condition of specimen based on the requirement. The specimen was analyzed in raw or original condition (M1), grinding with sand paper (M2), grinding with sand paper and polishing with diamond particle fluid (M3) and also etching with acid solution (M4), see subsection 3.2.4. Analysis was done by using optical microscope and SEM.

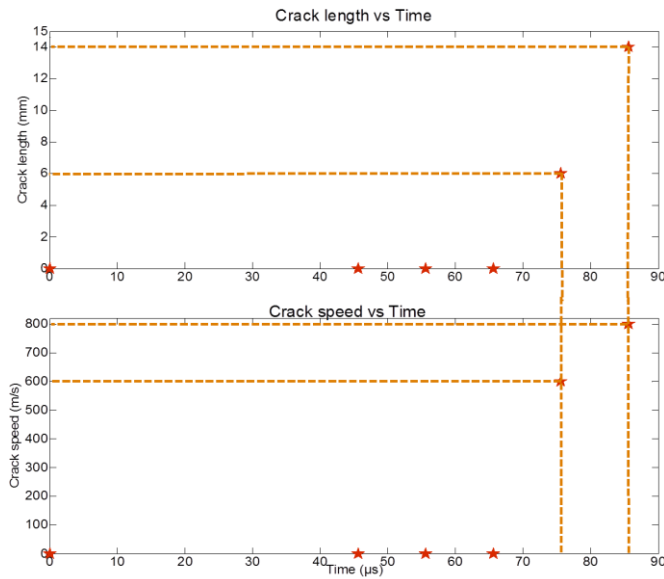


Fig. 3. 19 Crack length and crack speed for AA 7175

3.3.3.1 Crack propagation analysis

Crack propagation analysis was done on the specimen after being polished by sand paper and diamond liquid with particle size of 1 μm (M2). This is due to the fact that original surface was rough and not suitable for SEM observations. Crack propagation analysis was done on specimen impacted below critical speed where the crack arrests inside the plate. In the following, a ‘macro-crack’ stands for a crack with open lips whereas a ‘meso-crack’ stands for a crack with closed lips where matter cohesion remains.

Analysis on AA2024

The analysis was done on cracks of AA2024 specimens considering two different impact speeds in the speed range considered, see Fig. 3. 20 and Fig. 3. 21.

For impact speed of 111 m.s⁻¹, lower notch crack is longer than upper notch, see Fig. 3. 20 (a-c). Lower notch crack length is 7 mm and upper notch crack length is 2 mm, see Fig. 3. 20 (a). The depth of the impacted indentation is about 4 mm, see Fig. 3. 20(a). The cracks are composed of a succession of macro-cracks (in minority) and meso-cracks (in majority), see Fig. 3. 20 (c-d).

For impact speed of 133 m.s⁻¹, upper notch crack and lower notch crack length is 5 mm and 9 mm respectively, see Fig. 3. 21(a-c). Impacted indentation depth is 9 mm, see Fig. 3. 21 (a). The cracks are composed of a succession of macro-cracks (in majority) and meso-cracks (in minority), see Fig. 3. 21 (c-d).

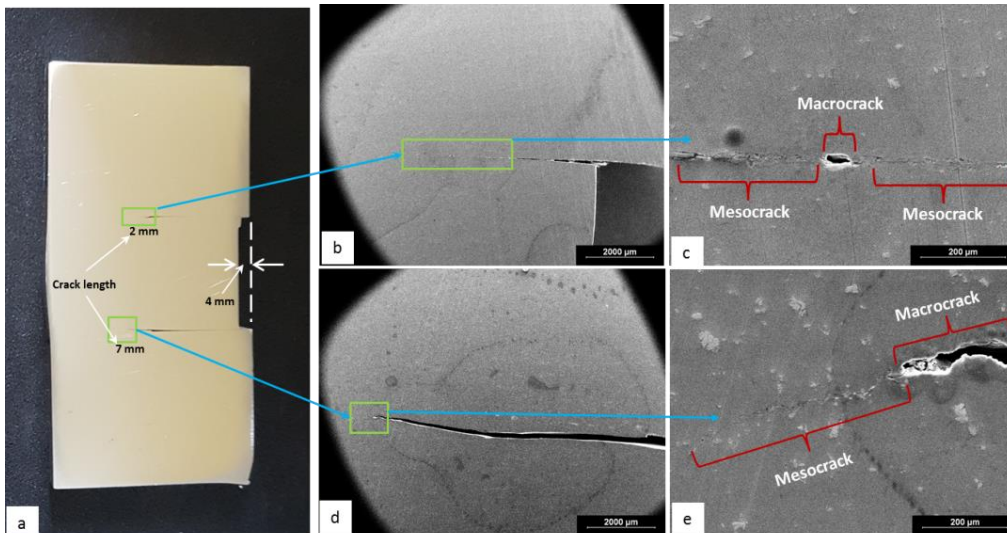


Fig. 3. 20 Post-mortem AA 2024 specimen after impact at 111 m.s^{-1}

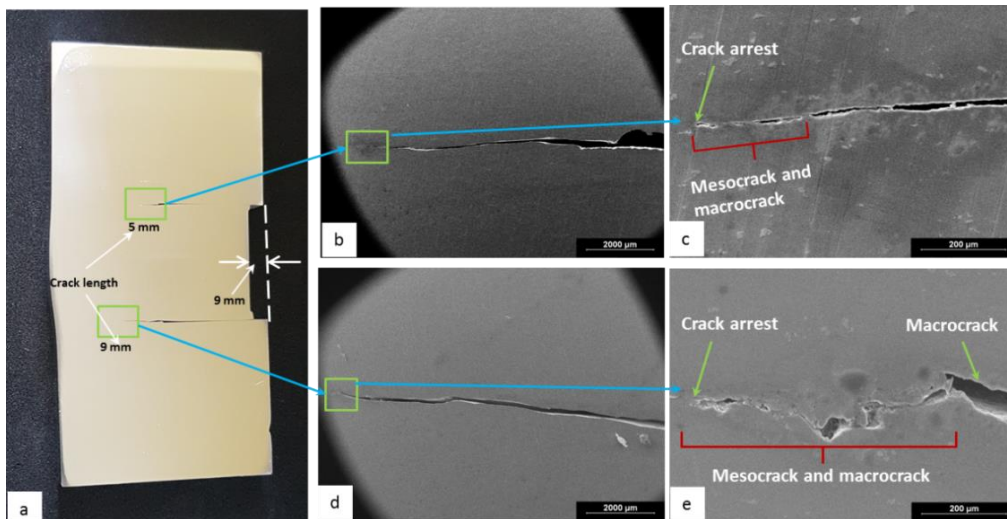


Fig. 3. 21 Post-mortem AA 2024 specimen after impact at 133 m.s^{-1}

Analysis on AA7175

Fig. 3. 22 shows specimen AA 7175 after impact at speed of 100 m.s^{-1} . Crack lengths of upper and lower notch are 1 mm and 4 mm respectively, see Fig. 3. 22 (a). The indentation after impact is 2 mm, see Fig. 3. 22 (a). Fig. 3. 22 (b) and Fig. 3. 22 (c) show the propagation of the cracks along the notch tip for lower and upper notch respectively. Meso-crack appears along with macro-crack at both notches as shown in Fig. 3. 22 (c) and Fig. 3. 22 (e).

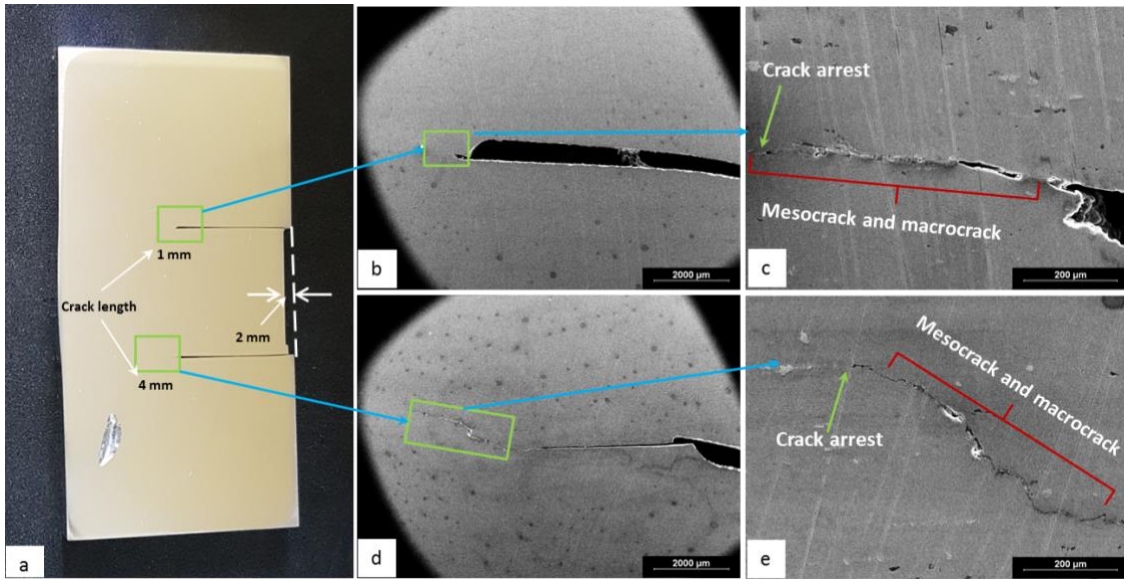


Fig. 3. 22 Post-mortem AA 7175 specimen after impact at 100 m.s^{-1}

Fig. 3. 23(a) shows the specimen AA 7175 after impact at speed of 120 m.s^{-1} with crack length for both upper and lower notches of 2 mm and 7 mm respectively. The indentation depth is 3 mm, see Fig. 3. 23(a). Crack propagation is depicted in Fig. 3. 23(b) and Fig. 3. 23(d) for upper and lower notch respectively. There are meso-cracks and macro-cracks appearing in both crack tips, see Fig. 3. 23(c) and Fig. 3. 23(e).

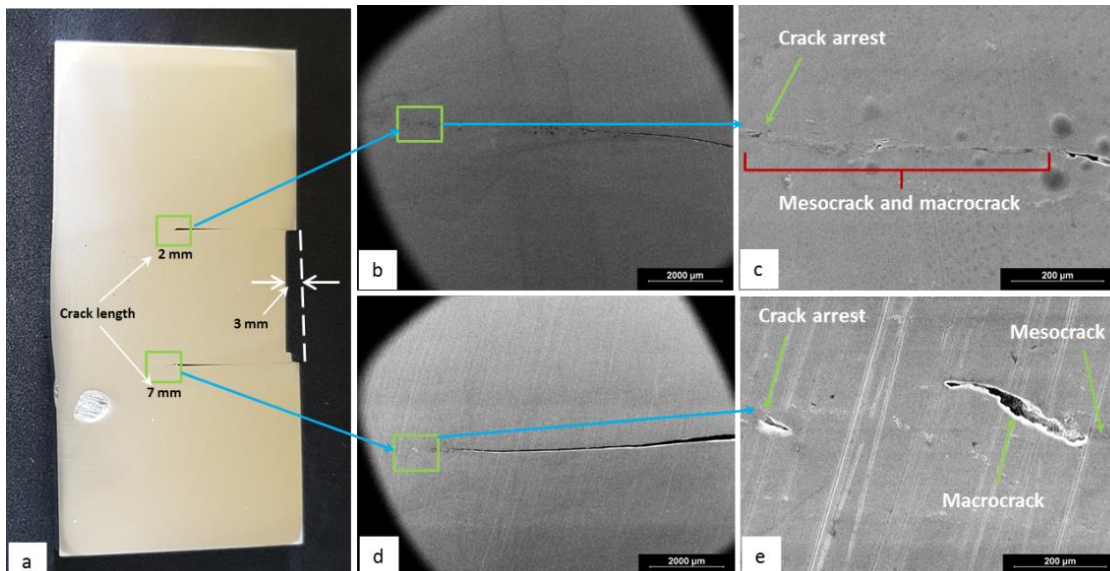


Fig. 3. 23 Post-mortem AA 7175 specimen after impact at 120 m.s^{-1}

It is expected that macro-cracks develop in the wake of meso-cracks by a progressive opening of the latter. In the present work, the succession of meso-and macro-cracks seems to show that the plate is subject to a complex loading, e.g. a combination of shear and tension loading.

3.3.3.2 Internal crack surface analysis

Specimen used to analyze the surface inside the crack was grinded by sand paper (M2), in order to remove the impurities on the surface and make the surface flat.

Analysis on AA2024

Fig. 3. 24 (a) shows the crack propagation for AA2024 KW specimen impacted at speed of 114 m.s^{-1} . The upper part of the crack was chosen for analyze because of its longer crack length. Total length of crack is about 7 mm.

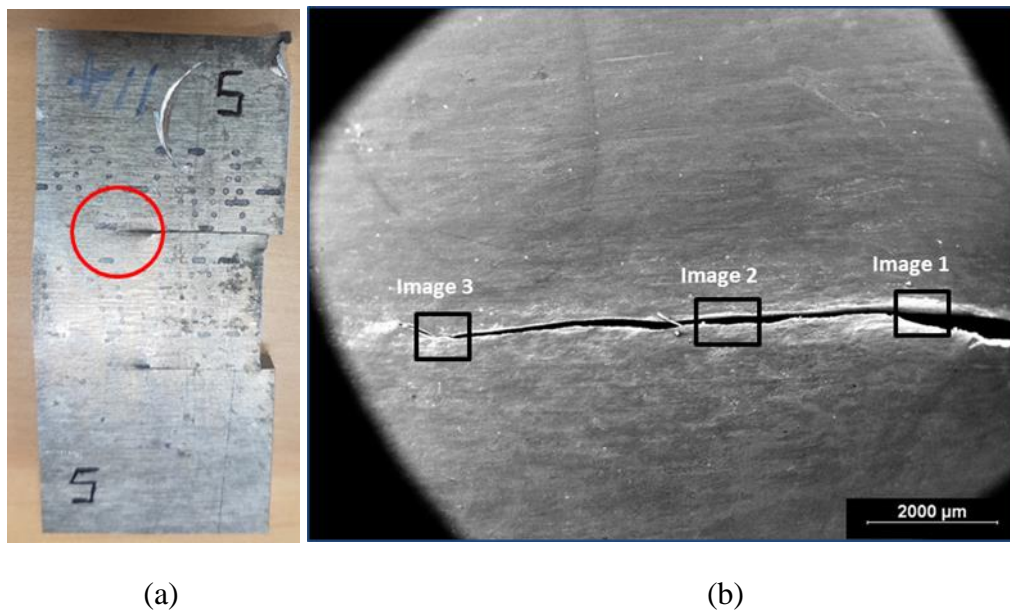


Fig. 3. 24 (a) Post impacted AA 2024 double notch plate at 114 m.s^{-1} (b) Macroscopic view of crack after surface polishing

The crack was analyzed at 3 zones as shown in Fig. 3. 24(b). Fig. 3. 25 shows the detail of microstructure of the three zones. Image 1, Fig. 3. 25 shows that the initiation of crack from the notch tip is characterized by flat shear and elongated dimples. The beginning of crack propagation proceeds by predominant shear Mode II due to the surface is characterized by flat shear and elongated dimple, see image 2, Fig. 3. 25. Image 3, Fig. 3. 25 shows crack bifurcation characterized by changes in the loading mode. It is worth noting that the crack bifurcates upwards, i.e. according to clockwise rotation. The microstructure inside the bifurcation zone depicts the combination of flat shear and dimple cluster, as a consequence of the combination of tension loading in opening Mode I and shear loading induced Mode II.

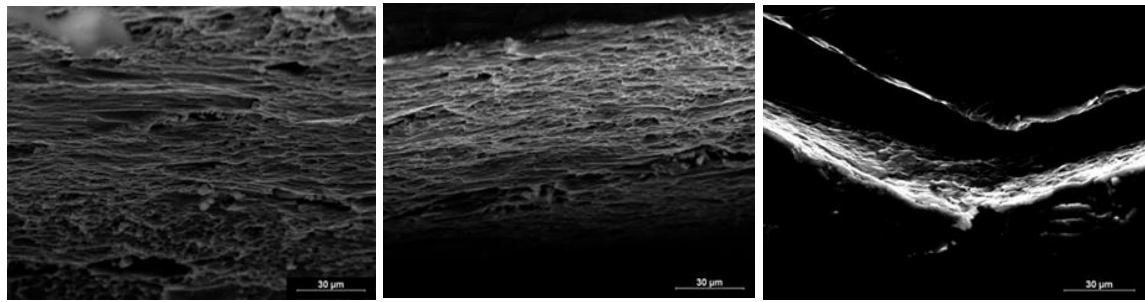


Image 1

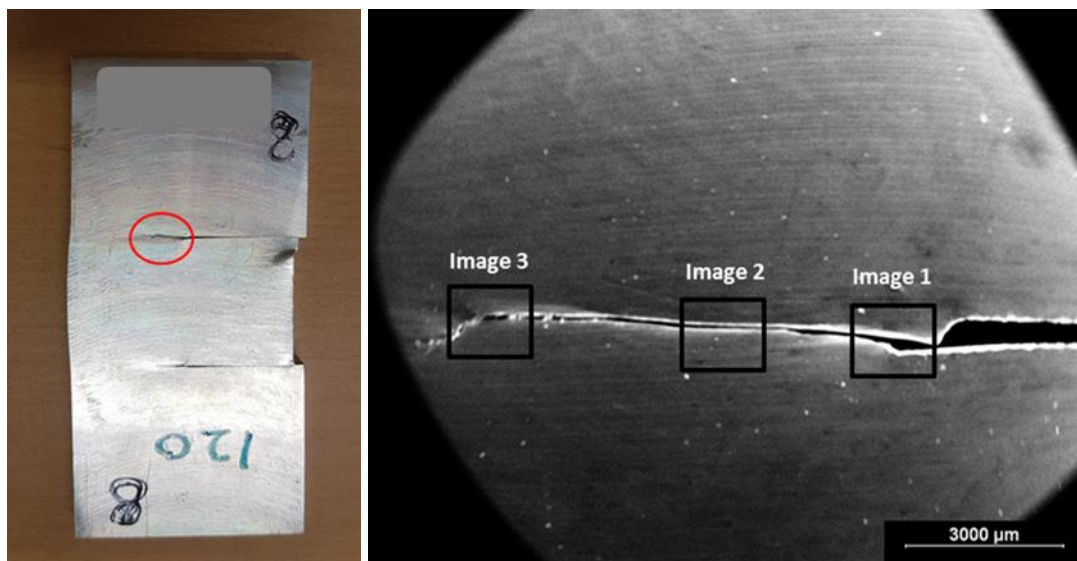
Image 2

Image 3

Fig. 3. 25 Microstructure of crack for AA 2024 after impact speed of 114 m.s^{-1}

Analysis on AA7175

Fig. 3. 26(a) shows the crack arrest inside the AA7175 specimen for the impact speed of 120 m.s^{-1} . Fig. 3. 26(b) shows the macroscopic view of the crack. The total length of the crack is close to 8 mm.



(a)

(b)

Fig. 3. 26 (a) Post impacted AA 7175 double notch plate at 120 m.s^{-1} (b) Macroscopic view of crack after surface polishing

Fig. 3. 27 shows three images of microstructure inside the crack zone at three different locations for AA7175 at impacted speed of 120 m.s^{-1} . The initiation of the crack from the notch tip is characterized by flat shear surface dominated by shearing induced Mode II failure, see image 1, Fig. 3. 27. Image 2, Fig. 3. 27 reveals that the crack propagation seems to proceed with predominant shearing induced Mode II due to existence of flat shear surface. Image 3, Fig. 3. 27 shows the change in loading direction at crack bifurcation zone, where the

microstructure is flat shear surface and mode II failure still seems predominant. It is worth noting that the crack bifurcates downwards, i.e. according to anti-clockwise rotation.

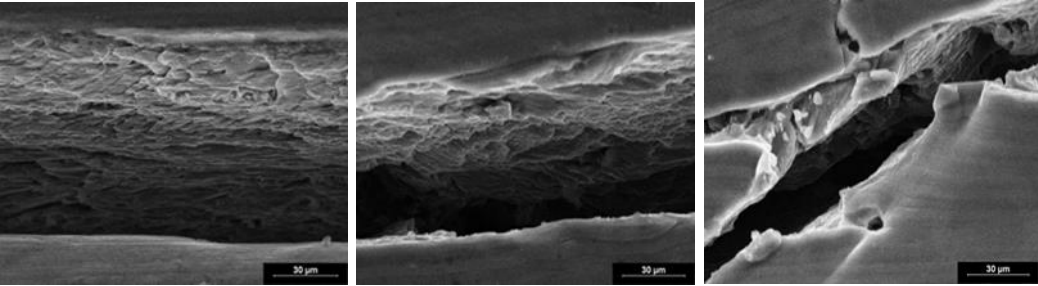


Image 1

Image 2

Image 3

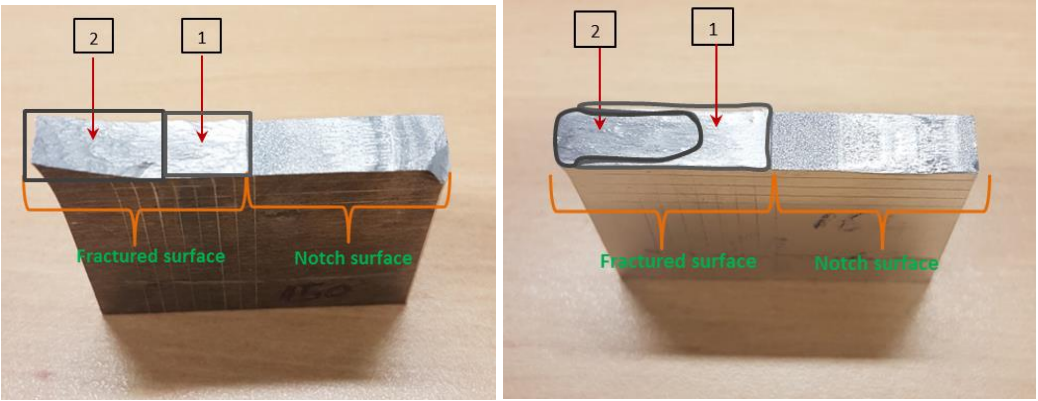
Fig. 3. 27 Microstructure of crack for AA 2024 after impact speed of 114 m.s⁻¹

For AA2024, the cracks propagate under shear Mode II then under combined shear Mode II and tension Mode I (bifurcation following clockwise orientation for upper crack).

For AA7175, the cracks seem to propagate under predominant shear Mode II only (bifurcation following anti-clockwise orientation for upper crack), as if the cracks followed a track (done by e.g. the white band evoked in subsection 3.3.2).

3.3.3.3 Fully fractured surface analysis

AA2024 and AA7175 specimens were observed in original condition, (M1). Fig. 3. 28(a) and Fig. 3. 28 (b) shows the ruptured surface of specimen after being impacted at the speeds of 150 m.s⁻¹ and 164 m.s⁻¹ for AA2024 and AA7175 respectively.



(a) AA2024 – 150 m.s⁻¹

(b) AA7175 – 164 m.s⁻¹

Fig. 3. 28 Fractography of ruptured surface (a) AA2024 at impact speed of 150 m.s⁻¹ (b) AA7175 at impact speed of 164 m.s⁻¹

Analysis on AA2024

According to Fig. 3. 28(a) for AA2024 two different fracture zones can be seen. Zone 1 shows the surface at crack initiation and zone 2 shows the crack propagation which ultimately leads to full fracture of the specimen.

Fig. 3. 29 shows the microstructure of AA2024 for both zones of ruptures after impact at 150 m.s^{-1} . Microstructural view for AA2024 shows, first zone is flat shear (Mode II) and second zone is opening mode where microstructural view shows a dimple cluster (Mode I) for AA2024.

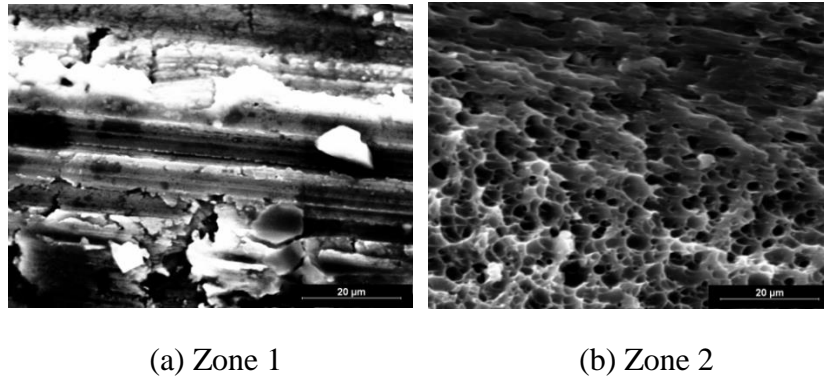


Fig. 3. 29 Microstructural view of AA2024 at fractured surface after impact at speed of 150 m.s^{-1}

Analysis on AA7175

Fig. 3. 28(b) also shows two zones where, zone 1 is crack initiation and zone 2 is crack propagation leading to full fracture of the structure. According to Fig. 3. 28 (b) crack lip area depicts similarity with the crack initiation zone 1.

Fig. 3. 30 shows the microstructure of AA7175 after impact at speed of 164 m.s^{-1} . Microstructural view of AA7175 shows both region are flat shear surface, thus the failure is mainly due to shear (Mode II).

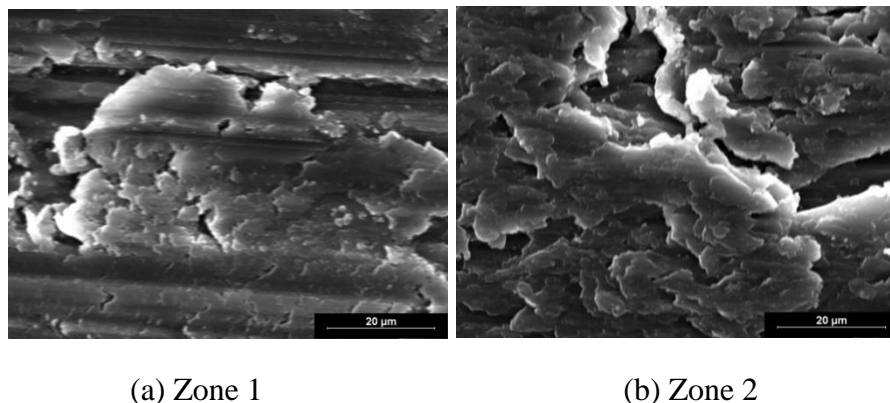


Fig. 3. 30 Microstructural view of AA7175 at fractured surface at speed of 164 m.s^{-1} (a) Flat shear (b) Flat shear

Fig. 3. 31 (a) and Fig. 3. 31(b) shows the ruptured surface of specimen after impact at the speed of 222 m.s^{-1} for AA2024 and 230 m.s^{-1} for AA7175.

Analysis on AA2024

According to Fig. 3. 31(a) two different fractured zones can be seen. Zone 1 shows the surface at crack initiation and zone 2 shows the crack propagation which leads to full fracture of the structure.

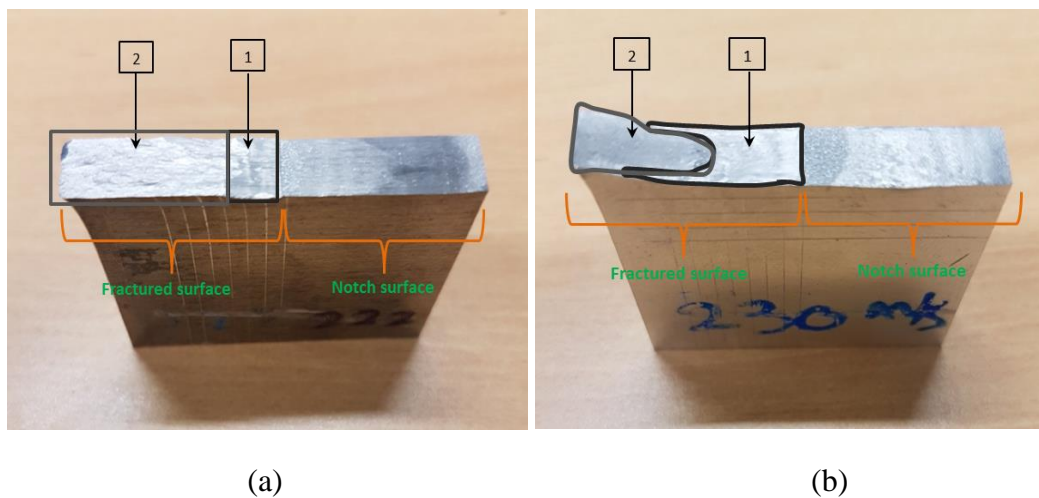
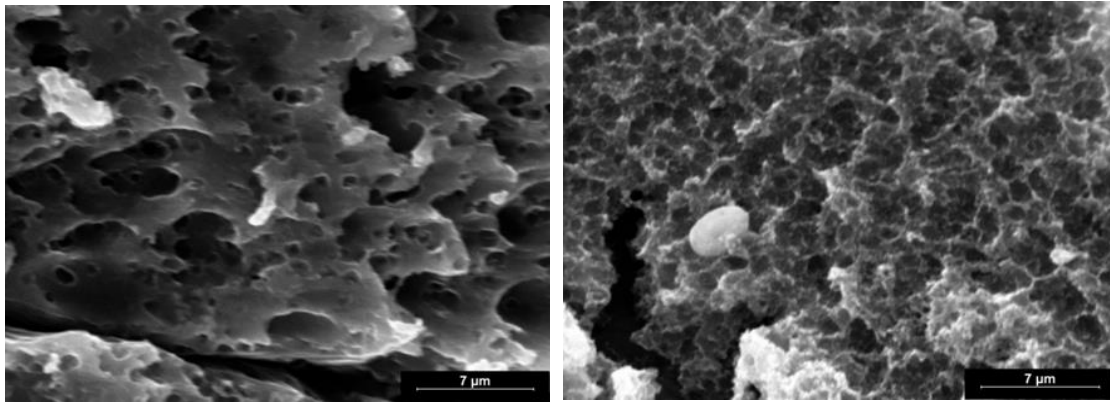


Fig. 3. 31 Fractography of ruptured surface (a) AA2024 at impact speed of 222 m.s^{-1} (b) AA7175 at impact speed of 230 m.s^{-1}

Fig. 3. 32 shows the microstructure of AA2024 for both zones of ruptures. Microstructural view for AA2024 shows, first zone is flat shear (Mode II) and second zone is opening mode where microstructural view shows a dimple cluster (Mode I) for AA2024.

Analysis on AA7175

Fig. 3. 31(b) also shows two zones where, zone 1 is crack initiation and zone 2 is crack propagation lead to full fracture of the structure. According to Fig. 3. 31 (b) crack lip area depicts similarity with the crack initiation zone 1. It is to be noted that this similarity is also observed for AA 7175 at impacted speed of 164 m.s^{-1} .

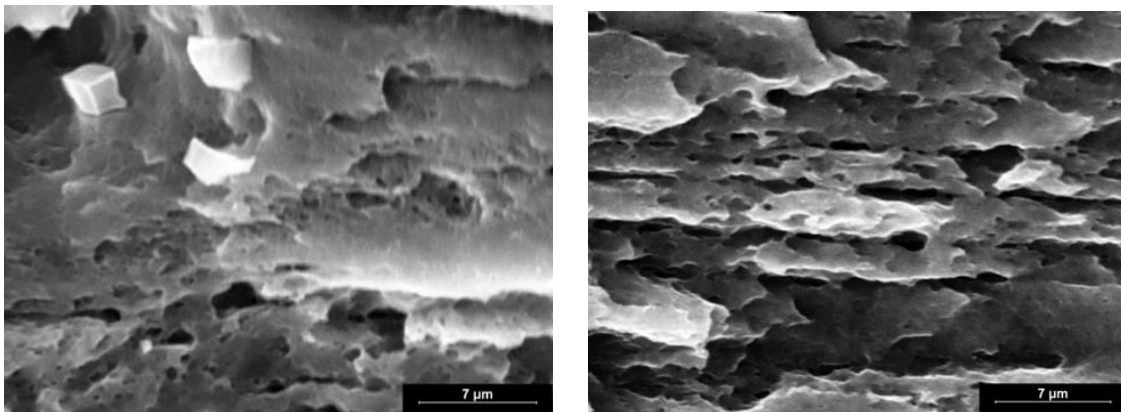


(a)

(b)

Fig. 3. 32 Microstructure view of AA2024 at ruptured surface (a) Flat shear (b) Dimple cluster

Fig. 3. 33 shows the microstructure of AA7175 after impact at speed of 230 m.s^{-1} . Microstructural view of AA7175 shows both region are flat shear surface, thus the failure is once again mainly due to shear (Mode II).



(a)

(b)

Fig. 3. 33 Microstructure view of AA7175 at ruptured surface (a) Flat shear (b) Flat shear

For AA2024, there are evidences of zones of failures under Mode II and Mode I.

For AA7175, there are evidences of zones of failures under Mode II only.

3.3.3.4 Crack lips analysis

Specimens were polished and etched near the crack lip by acid (M4) in order to observe the microstructure near crack lip, see Fig. 3. 34. The impact velocity for AA2024 and AA7175 are 222 m.s^{-1} and 230 m.s^{-1} respectively.

For AA2024 crack lip analysis does not show any evidence of shear band see Fig. 3. 35, and on the other hand for AA7175 the adiabatic shear band with average width of 6µm is visible on the crack lips as shown in Fig. 3. 36. It is to be noted that there is no evidence of adiabatic shear band at lower impact velocities.

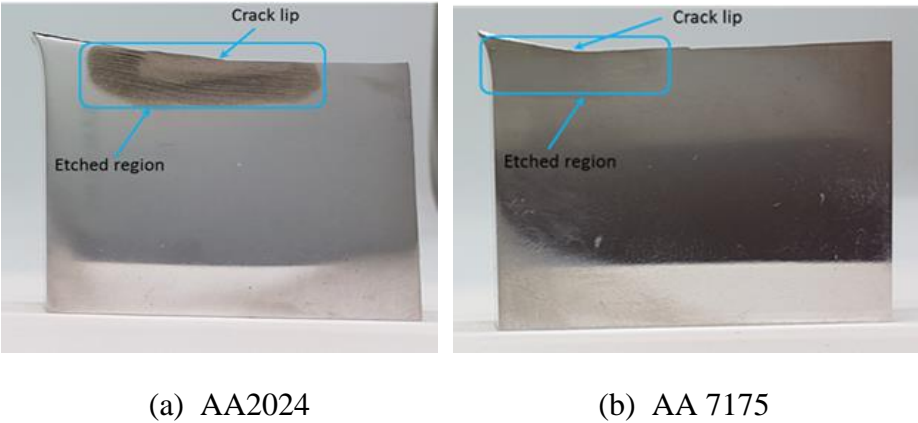


Fig. 3. 34 Crack lip after polished and etched

3.3.4 Nano-hardness of crack tip surface

Nano-hardness on the surface near the crack tip region was done by using nano-indentor apparatus as discussed earlier in the subsection 3.2.5. Total area of the indentation is a 2x2 mm²-square. The region around the crack tip is expected to be the siege of microstructural transformations which may be revealed by the nano-hardness tests.

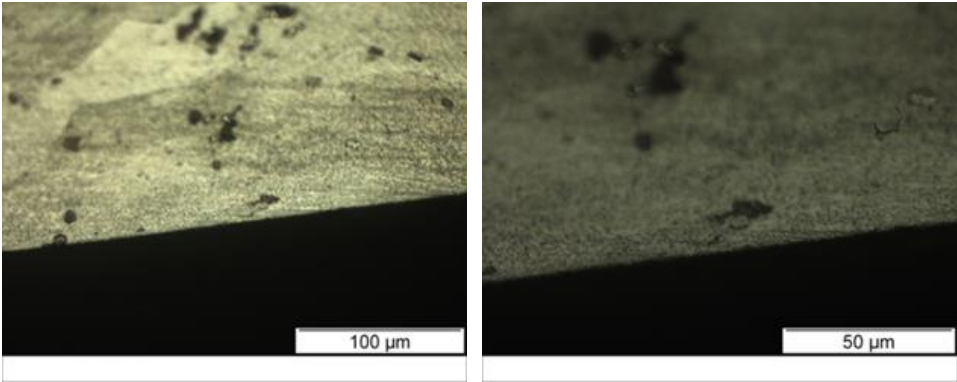


Fig. 3. 35 Optical microscopic view of crack lip region for AA2024

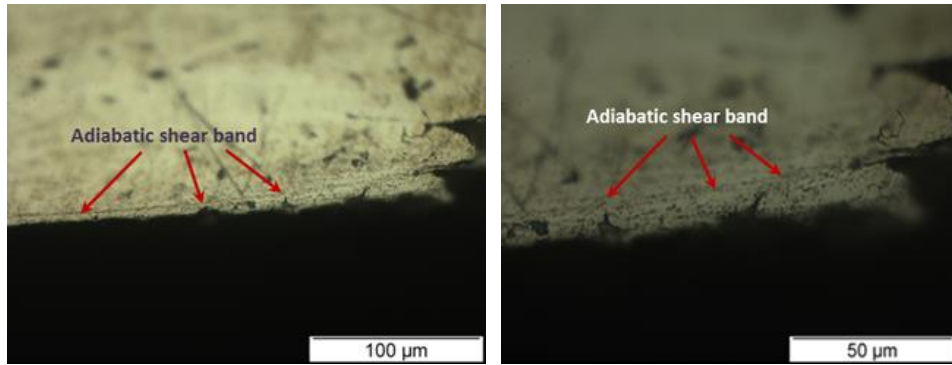


Fig. 3. 36 Optical microscopic view of crack lip region for AA7175

Analysis on AA2024

Fig. 3. 37 and Fig. 3. 38 show the nano-hardness at crack tip for AA 2024 after impact speeds of 111 and 133 m.s⁻¹ respectively.

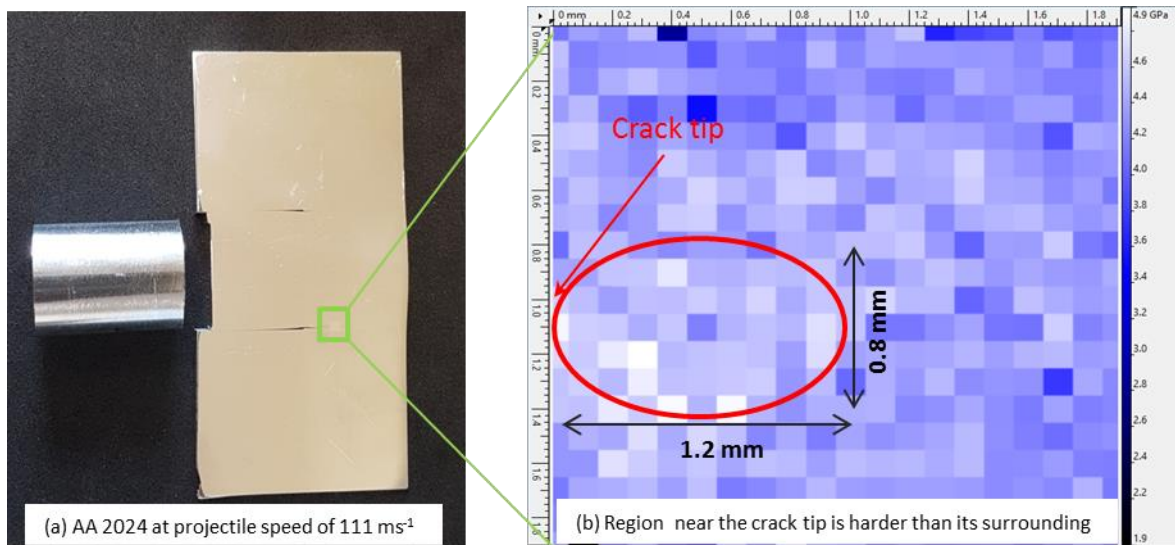


Fig. 3. 37 Nanohardness of crack tip for AA 2024 at impacted speed of 111 m.s⁻¹. Light blue for higher hardness value and dark blue for lower hardness value.

According to Fig. 3. 37-Fig. 3. 38, the region around lower part crack tip shows that nano-hardness is higher near the crack tip (crack process zone) compared to its surrounding regions as depicted in Fig. 3. 37(b) where the white region represents harder area and the dark region represents softer area. The process zone is a wide ellipse. The average value of nano-hardness of crack tip region inside the processing zone is 4.8 GPa whereas average hardness outside the process zone is around 4.5 GPa. The equivalent Vickers hardness (HV) value is given in the table 3.6 according to Eq.(3.1).

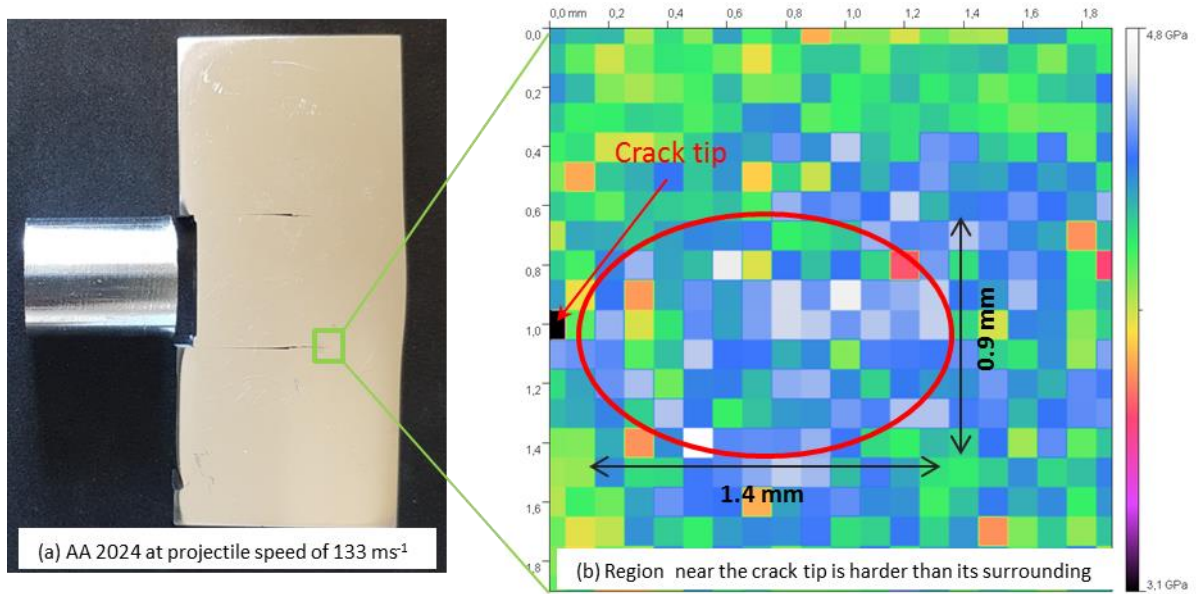


Fig. 3. 38 Nanohardness of crack tip for AA 2024 at impacted speed of 133 m.s^{-1} . White for higher hardness value and black for lower hardness value.

Fig. 3. 38 shows the specimen and hardness mapping at impact speed of 133 m.s^{-1} . The region near the crack shows harder than its surrounding area. The average nano-hardness values inside and outside the process zone are 4.6 GPa and 4.0 GPa respectively.

Analysis on AA7175

Fig. 3. 39 shows nano-hardness mapping for AA7175 after impact speed of 100 m.s^{-1} . The process zone is a narrow ellipse, even a line (Fig. 3. 40(b)). The average nano-hardness inside and outside the processing zone is 4.4 GPa and 4.5 GPa respectively, i.e. a lower hardness inside the process zone and a higher hardness outside.

Fig. 3. 40 shows specimen after impact speed of 120 m.s^{-1} . The process zone is a line of pixels. The crack tip region also shows less hardness inside the process zone compared to its surrounding areas, with 4.2 GPa inside the process zone against 4.4 GPa outside.

3.4 Summary

- **AA2024**

For AA2024, the critical impact speed for crack arrest inside the structure is close to 150 m.s^{-1} . Below this critical speed, the crack propagates and then arrests within the plate. Above this critical impact speed the plate fully fractures into two or three parts as depicted in Fig. 3. 11(a).

The crack tip speed was estimated over a time period of $10 \mu\text{s}$ for impact speed above critical speed. Maximum value of crack tip speed reaches 980 m.s^{-1} for impact speed of 222 m.s^{-1} .

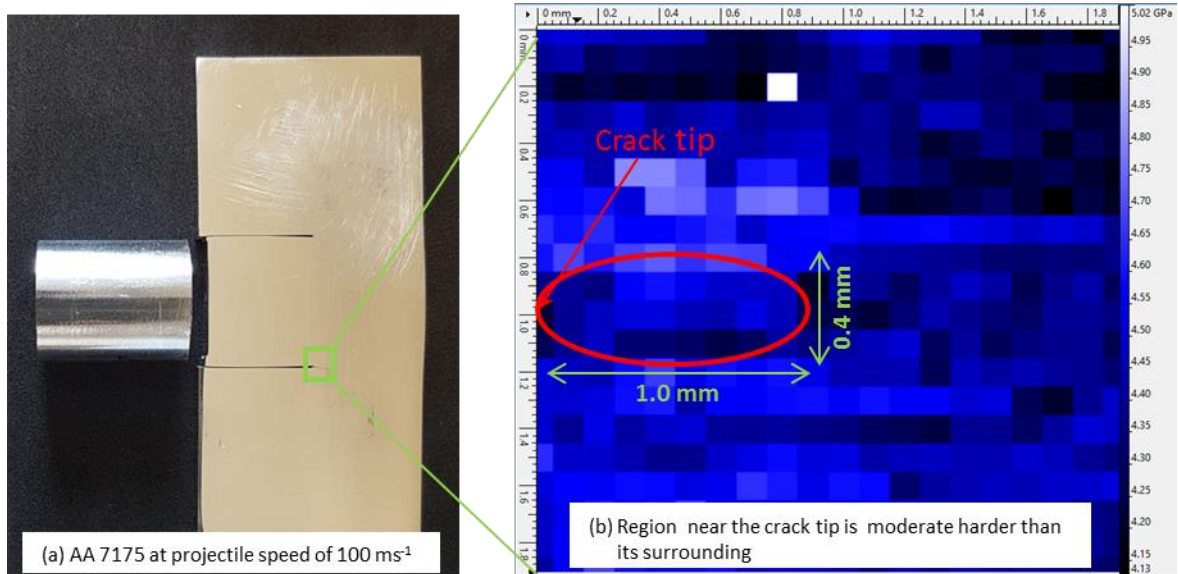


Fig. 3. 39 Nanohardness of crack tip for AA 7175 at impacted speed of 100 m.s^{-1} . Light blue for higher hardness value and dark blue for lower hardness value.

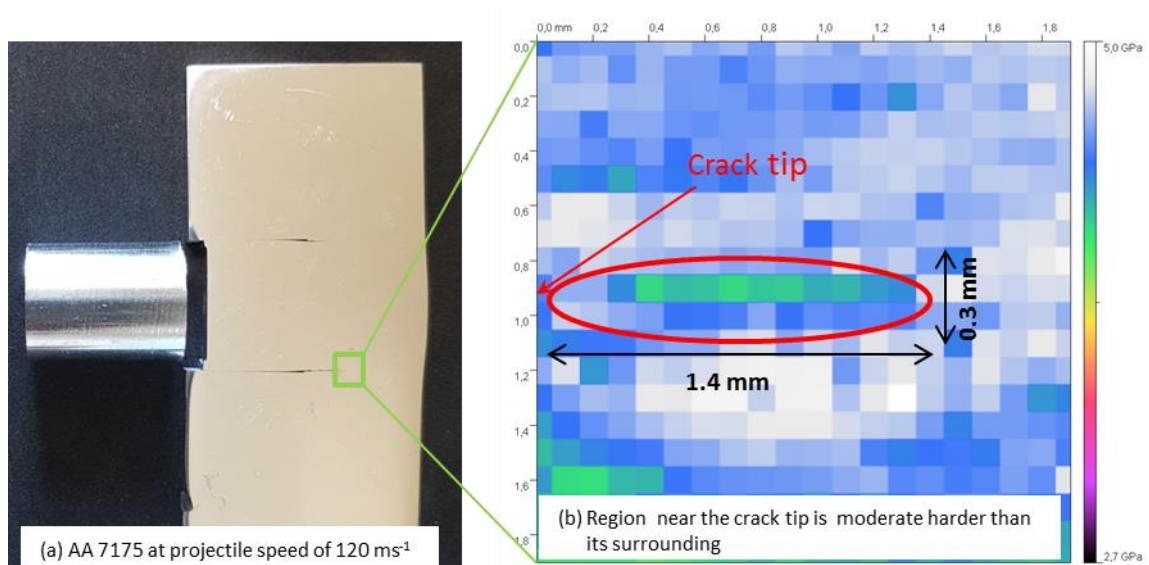


Fig. 3. 40 Nanohardness of crack tip for AA 7175 at impacted speed of 120 m.s^{-1} . White for higher hardness value and black for lower hardness value.

The crack tip analysis for speed lower than critical impact speed, shows the appearance of (open) macro-crack and (closed, cohesive) meso-crack. Both types of cracks are eventually arrested inside the plate.

Microstructural observation inside the crack for the plates impacted below critical speed shows that the failure is predominantly Mode II induced failure. The microstructure shows at early stage of crack initiation near notch tip is flat shear surface surrounded by elongated dimple cluster. Further crack propagation shows the failure mechanism is under shearing

mode due to flat shear surface depicted in this region, see image 2 on Fig. 3. 25. Tip of the crack region shows the bifurcation of the crack where the failure mechanism is combination of flat shear and dimple cluster, see image 3 on Fig. 3. 25.

Fully fractured specimens were analyzed for two different impact speeds, namely 150 and 222 m.s^{-1} . Both fractured surfaces shows at early stage the failure of the plate under shearing induced Mode II and at latter stage under tension induced Mode I, see Fig. 3. 29 and Fig. 3. 32.

Crack lip microstructural observation on fully fractured specimen evidences no adiabatic shear bands, see Fig. 3. 35.

Nano indentation test results prevail that nano-hardness close to crack tip region is larger than surrounding region in the considered process zone for two different specimens analyzed after impact speed of 111 and 133 m.s^{-1} , see Fig. 3. 37 and Fig. 3. 38 respectively. The material in the process zone keeps on being subject to strain hardening without major microstructural changes.

- **AA7175**

For AA7175, the critical impact speed to crack arrest inside the plate is close to 130 m.s^{-1} . Above this critical impact speed the specimen fractures into two or three parts, see Fig. 3. 11 (b).

AA7175 shows the formation of a white band which appears in the frames recorded by a high speed camera as the likely optical signature of adiabatic shear banding. The maximum values of the white band and crack tip speeds for the time frame of 10 μs , was estimated at about 720 m.s^{-1} and 800 m.s^{-1} respectively for the impact speed of 230 m.s^{-1} .

The crack tip analysis for speed lower than critical impact speed shows the presence of macro-crack and meso-crack before both cracks eventually arrest inside the specimen.

Microstructural observation inside the crack for the plates impacted below critical impact speed shows that the failure is predominantly Mode II. The microstructure shows flat shear surface along the crack from initiation up to bifurcation zone as depicted in the Fig. 3. 27.

Fully fractured specimens were analyzed for two different impact speeds which are above the critical impact speed, namely 164 ms^{-1} and 230 ms^{-1} . The microstructure for both specimens shows that the fractured was predominant by shearing induced Mode II, see Fig. 3. 32 and Fig. 3. 33.

Microscopic observations on fully fractured specimen shows that there are bands of shear localization (adiabatic shear bands) with average width of 6 μm along the crack lips, see Fig. 3. 36.

Nano indentation test results prevail that nano-hardness close to crack tip region is lower than surrounding region in the considered process zone for two different specimen analyzed after impact speeds of 100 and 120 m.s⁻¹, see Fig. 3. 39 and Fig. 3. 40 respectively. The material in the process zone is subject to softening caused by major microstructural changes, which is coherent with shear localization upstream from the crack.

- **AA2024 vs. AA7175**

Critical speed for AA2024 and AA7175 to crack arrest inside the material is close to 150 m.s⁻¹ and 130 m.s⁻¹ respectively. The value of the critical impact speed is seen to be higher for AA2024. Crack formation in AA7175 is seen to be preceded by shear localization in the form of adiabatic shear band.

Below critical speed

At lower impact speeds both alloys show the presence of (open) macro-crack and (closed) meso-crack. These cracks arrest inside the plate for impact speeds below the critical speed.

Table 3. 4 shows the maximum values of white band and crack tip speed for both alloys. The white band which is likely the optical signature of the shear localization band appears in AA7175 only. The value of its maximum speed is close to 720 m.s⁻¹. The value of the maximum crack tip speed is higher for AA7175 (800 m.s⁻¹ against 720 m.s⁻¹ for AA2024 for the impact configuration considered).

Table 3. 4 Maximum white band and crack tip speed

Failure Material	Maximum white band speed (m.s ⁻¹)	Maximum crack speed (m.s ⁻¹)
AA 2024	-	980
AA 7175	720	800

Microstructural observation of the inside of the crack for both alloys evidence flat shear surface together with elongated dimple showing that crack initiation is dominated by shearing mode. The crack tip bifurcations of AA2024 and AA7175 are opposite.

Above critical speed

Microscopic observation on fully fractured specimens shows for AA2024 that the first stage of fracture is dominated by shearing induced Mode II and that a second stage is dominated by tension induced Mode I. For AA7175 the fracture is controlled by shearing induced Mode II failure only.

The observation on crack lip on fully fractured specimen evidences the absence of shear localization band for AA2024 and the presence of shear localization band for AA7175.

Table 3. 5 shows the averaged value of nano-hardness and its Vickers hardness (HV) equivalent in a region near the crack tip inside and outside the process zone. For AA2024, the area in front of the crack tip is wide and harder, when compared with the surrounding region, see subsection 3.3.4. For AA7175, the area in front of the crack tip is narrow and softer when compared with the surrounding region, see section 3.3.4.

Table 3. 5 Average nano-hardness and Vickers hardness inside and outside the process zone

Material	AA2024				AA7175			
	Process zone				Process zone			
Impact speed(m/s)	Inside		Outside		Inside		Outside	
	Nano-hardness	Vickers hardness						
	GPa	HV	GPa	HV	GPa	HV	GPa	HV
100	-		-		4.4	407	4.5	416
111	4.8	444	4.5	417	-			
120	-		-		4.2	389	4.4	407
133	4.6	426	4.0	370	-			

3.5 Concluding remarks

In the present work, double notched plates made of AA2024 and AA7175 aluminium alloys were submitted to impact loading in view of experimentally investigating the crack arrest capabilities of the constitutive materials under high strain rate loading in the context of damage tolerance of aeronautical structures. For the impact configurations considered, it is shown that for both alloys there exists a critical impact speed below which cracks, initiated from notch tips, arrest inside the plate and above which cracks propagate throughout the whole plate leading to complete fracture. The critical impact speed is lower for AA7175 which possesses the higher strength, or equivalently higher for AA2024 which possesses the lower strength.

For both alloys the direction of the cracks is initially collinear to the notch direction then follows a slight angle so as the cracks would converge if the plate were infinitely wide, evidencing a crack propagation under predominant shear controlled Mode II. Bands of shear

localization are observed on the crack lips of post-impacted AA7175 plates and not on the ones of post-impacted AA2024 plates. Adiabatic shear bands are known to favor premature failure. Adiabatic shear banding may explain the low value of critical impact speed for AA7175 when compared with the impact speed for AA2024. Moreover, crack propagation according to Mode II (i.e. following a slight angle) is not necessarily preceded by adiabatic shear banding. Yet, if so, it would lead to a premature failure. Microscopic analyses of the crack surfaces reveal ductile fracture for both materials.

A crack bifurcation is observed for arrested cracks, i.e. for impact speed lower than critical speed. The analysis of wave interactions during the impact-induced loading shows that the plate and the cracks are subject to complex, alternate shear and tension loading. The crack bifurcation may thus more probably result from the turn of predominant shear wave-induced loading to predominant tension wave-induced loading, as a consequence of changes in the loading path and not as a consequence of changes in the micro-mechanisms (e.g ductile to brittle).

These experimental results may be used to discriminate numerical models aiming at reproducing the failure of lightweight alloys under impact loading within an engineering design process.

3.6 References

- [1] J. F. Kalthoff and S. Winkler, “Failure mode transition at high rates of shear loading in: C.Y. Chiem, H.-D. Kunze, L.W. Meyer (Eds.),” *Proc. Int. Conf. Impact Load. Dyn. Behav. Mater.*, vol. 1, pp. 185–195, 1987.
- [2] J. F. Kalthoff and A. Bürgel, “Influence of loading rate on shear fracture toughness for failure mode transition,” *Int. J. Impact Eng.*, vol. 30, no. 8–9, pp. 957–971, 2004.
- [3] E. Roux, P. Longère, O. Cherrier, T. Millot, D. Capdeville, and J. Petit, “Analysis of ASB assisted failure in a high strength steel under high loading rate,” *Mater. Des.*, vol. 75, pp. 149–159, 2015.
- [4] M. Zhou, A. J. Rosakis, and G. Ravichandran, “Dynamically propagating shear bands in impact-loaded prenotched plates—I. Experimental investigations of temperature signatures and propagation speed,” *J. Mech. Phys. Solids*, vol. 44, no. 6, pp. 981–1006, 1996.
- [5] P. Longère and A. Dragon, “Dynamic vs. quasi-static shear failure of high strength metallic alloys: Experimental issues,” *Mech. Mater.*, vol. 80, no. PB, pp. 203–218, 2015.
- [6] Y. B. Bradley Dodd, *Introduction to Adiabatic shear localization*, Revised Ed. Imperial College Press, 2015.
- [7] P. Longère, “Adiabatic shear banding assisted dynamic failure: Some modeling issues,”

- Mech. Mater.*, vol. 116, pp. 49–66, 2018.
- [8] C. Zener and J. H. Hollomon, “Effect of strain rate upon plastic flow of steel,” *J. Appl. Phys.*, vol. 15, no. 1, pp. 22–32, 1944.
- [9] J. Dormeal, Richard & Pierre Ansart, “Adiabatic Shearing: Influence of Predeformation.. Journal de Physique (Paris), Colloque. 46. 299-306.,” *J. Phys. Paris*), vol. 46, pp. 299–306, 1985.
- [10] A. Marchand and J. Duffy, “an Experimental-Study of the Formation Process of Adiabatic Shear Bands in a Structural-Steel,” *J. Mech. Phys. Solids*, vol. 36, no. 3, p. 251-, 1988.
- [11] C. Mazeau, L. Beylat, P. Longere, and P. F. Louvigne, “On the quantitative evaluation of adiabatic shear banding sensitivity of various titanium alloys,” *J. Phys. IV JP*, vol. 7, pp. 429–434, 1997.
- [12] S. -C. Liao and J. Duffy, “Adiabatic shear bands in a Ti-6Al-4V titanium alloy,” *J.Mech.Phys.Solids*, vol. 46, no. 11, pp. 2201–2231, 1998.
- [13] Z. guo Gao, X. ming Zhang, Y. sheng Zhao, M. an Chen, and H. jie Li, “The effect of strain rate on the microstructure of 2519A aluminium alloy plate impacted at 573 K,” *J. Alloys Compd.*, vol. 481, no. 1–2, pp. 422–426, 2009.
- [14] X. P. Liang, H. Z. Li, L. Huang, T. Hong, B. Ma, and Y. Liu, “Microstructural evolution of 2519-T87 aluminium alloy obliquely impacted by projectile with speed of 816 m/s,” *Trans. Nonferrous Met. Soc. China (English Ed.)*, vol. 22, no. 6, pp. 1270–1279, 2012.
- [15] Y. Yang, Y. Zeng, and Z. W. Gao, “Numerical and experimental studies of self-organization of shear bands in 7075 aluminium alloy,” *Mater. Sci. Eng. A*, vol. 496, no. 1–2, pp. 291–302, 2008.
- [16] Y. Yang, D. H. Li, H. G. Zheng, X. M. Li, and F. Jiang, “Self-organization behaviors of shear bands in 7075 T73 and annealed aluminium alloy,” *Mater. Sci. Eng. A*, vol. 527, no. 1–2, pp. 344–354, 2009.
- [17] C. Mondal, B. Mishra, P. K. Jena, K. Siva Kumar, and T. B. Bhat, “Effect of heat treatment on the behavior of an AA7055 aluminium alloy during ballistic impact,” *Int. J. Impact Eng.*, vol. 38, no. 8–9, pp. 745–754, 2011.
- [18] Starke E.A. Jr and Staley J.T., “Application of modern aluminium alloys to aircraft,” *Pergamon*, vol. 32, pp. 131–172, 1996.
- [19] T. Dursun and C. Soutis, “Recent developments in advanced aircraft aluminium alloys,” *Mater. Des.*, vol. 56, pp. 862–871, 2014.

4. Constitutive modelling

Abstract. This chapter presents the constitutive equations that characterize the material behavior. Constitutive equations developed here are based on experimental results at various strain rates and temperatures. Matlab R2013a software was used to find the appropriate parameters and constants that influence the yield stress by developing a code and applying curve fitting method. Finally, the models are validated by comparing them to the experimental results.

Table of contents

4.1	Introduction	98
4.2	Modelling procedure	98
4.2.1	Step 1: Determination of the non-viscous stress	99
4.2.1.1	Examples of strain hardening functions.....	100
4.2.1.2	Examples of thermal softening functions.....	100
4.2.1.3	Examples of tension/compression asymmetry	101
4.2.2	Step 2: Determination of the viscous stress	102
4.2.2.1	Examples of strain rate hardening functions.....	102
4.2.2.2	Case of Johnson-Cook model	102
4.3	Application to AA2024 and AA7175.....	103
4.3.1	AA2024	103
4.3.1.1	Global perspective for AA2024	103
4.3.1.2	Constitutive modelling for AA2024	104
4.3.1.3	Curve fitting for AA2024.....	109
4.3.2	AA7175	110
4.3.2.1	Global perspective for AA7175	110
4.3.2.2	Constitutive modelling for AA7175	111
4.3.2.3	Curve fitting for AA7175.....	116
4.4	Conclusion.....	117
4.5	References	118

4.1 Introduction

In this section the behavior of both the AA2024 and AA7175 is considered to be influenced by certain factors, such as plastic strain, strain rate, temperature and stress triaxiality. The effect of direction of machining is not considered in this work due to the fact that all specimens that were used for the experimental study were prepared along the rolling direction of the plate. Constitutive relation was developed based on two approaches; Global oriented approach and modelling oriented approach. Explicit type of model is developed where the material behavior is defined based on phenomenological observations from experimental results. In this chapter the method to develop a constitutive modelling will be discussed for both alloys under consideration, which are AA2024 and AA7175. Matlab R2013a software was used to identify the parameters by a code written for the purpose and applying curve fitting method based on experimental results.

Three phenomena that are important and must be described in the constitutive equations governing the flow stress are: strain hardening, thermal softening and viscoplasticity [1]. The acquired data from tension and compression tests were used to develop a constitutive model for both alloys. The yield stress is the function of plastic strain, plastic strain rate, temperature and also material properties. Considered temperature range in this study was from ambient to elevated temperature of up to 200°C. Tests were done at different range of strain rates, which covers quasi static to dynamic range, see Chapter II, thermo-mechanical characterization. Range of quasi static and dynamic test was 10^{-3} to 10^{-1} s $^{-1}$ and 2000 to 4500s $^{-1}$ respectively.

The modelling procedure is outlined in Section 4.2 then applied to AA2024 and AA7175 aluminium alloys in Section 4.3. Concluding remarks are given in Section 4.4.

4.2 Modelling procedure

In the context of rate-dependent plasticity, the yield function reads

$$f(\underline{\underline{\sigma}}, \sigma_{nv}) = \sigma_{eq}(\underline{\underline{\sigma}}) - \sigma_{nv}(\varepsilon_p, T) = \sigma_v(\varepsilon_p, \dot{\varepsilon}_p, T) \geq 0 \quad (4.1)$$

where $\sigma_{eq} = \sqrt{\frac{3}{2} \underline{\underline{s}} : \underline{\underline{s}}}$ is the equivalent stress, $\underline{\underline{s}}$ being the deviatoric part ($Tr \underline{\underline{s}} = 0$) of the stress tensor $\underline{\underline{\sigma}}$, σ_{nv} is the non-viscous (rate independent) stress and σ_v the viscous (rate dependent) stress. $\varepsilon_p, \dot{\varepsilon}_p, T$ are the accumulated plastic strain, plastic strain rate and temperature. One can rewrite (4.1) in the form

$$\sigma_{eq}(\underline{\underline{\sigma}}) = \sigma_y(\varepsilon_p, \dot{\varepsilon}_p, T) = \sigma_{nv}(\varepsilon_p, T) + \sigma_v(\varepsilon_p, \dot{\varepsilon}_p, T) \quad (4.2)$$

where σ_y represents the strain, strain rate and temperature dependent yield or flow stress. The loading dependent stress state quantified by σ_{eq} is defined by the material yield/flow stress σ_y . The various effects of plastic strain, strain rate, temperature and stress triaxiality ratio are

depicted in Fig. 4. 1 where the non-viscous stress is associated to the radius of the Mises yield function $\sigma_{nv}(\varepsilon_p, T) = R(\varepsilon_p, T)$.

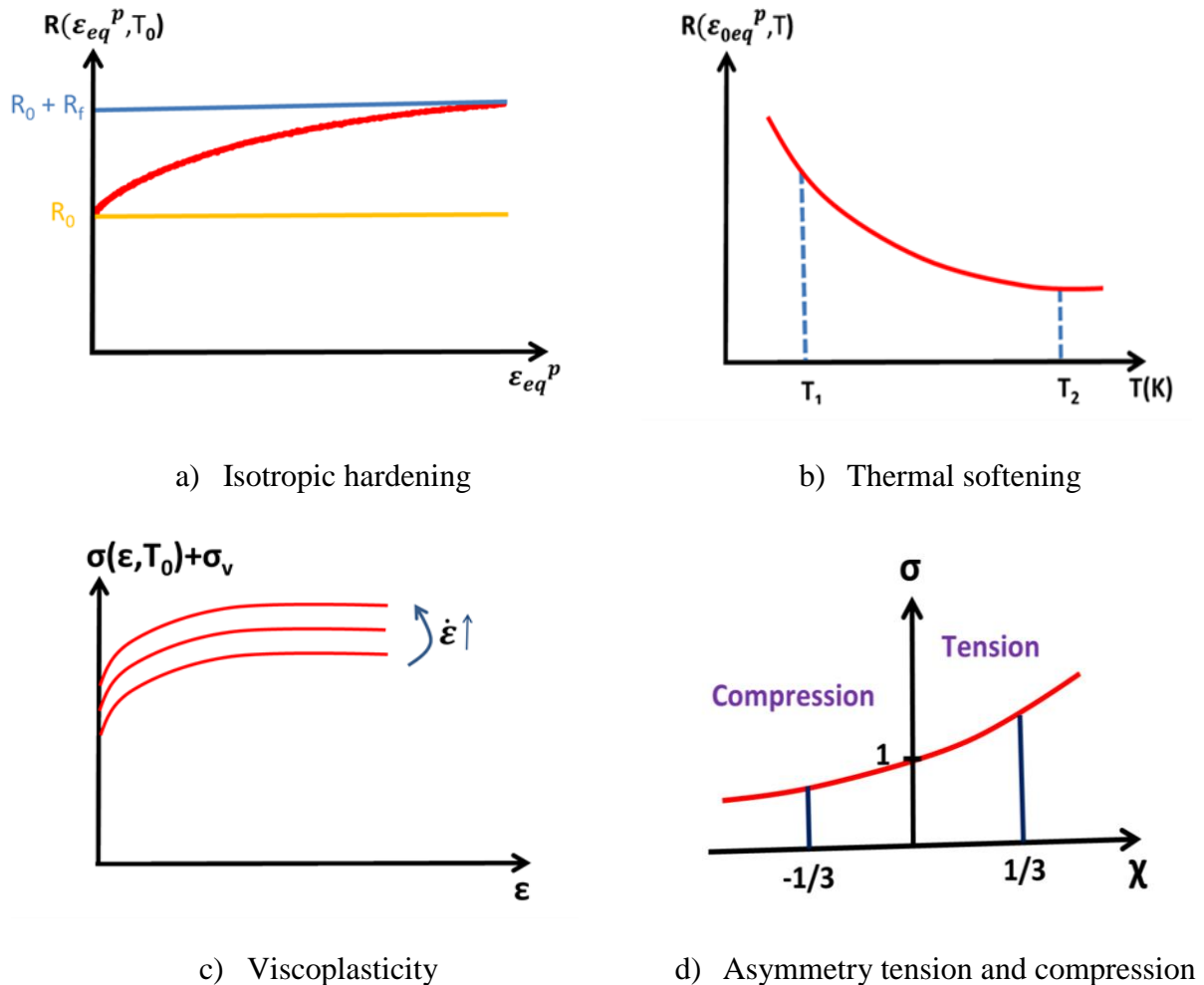


Fig. 4. 1 Modelling parameters [1]

The modelling procedure comprised two steps:

- Step 1 which consists in determining notably the strain hardening and thermal softening contained in the non-viscous stress
- Step 2 which aims at expressing the viscous stress

4.2.1 Step 1: Determination of the non-viscous stress

For a given loading type (compression, tension), a given temperature, a given strain rate, and other given specific parameters (e.g. direction), the non-viscous stress is deduced from (4.3)

$$\sigma_{nv}(\varepsilon_p, T) = \sigma_{eq}(\underline{\underline{\sigma}}) - \sigma_v(\varepsilon_p, \dot{\varepsilon}_p, T) \quad (4.3)$$

This step allows for determining the strain hardening, thermal softening, and further potential tension/compression asymmetry or/and plastic anisotropy. In the present work, the specimens were all machined along the rolling direction.

4.2.1.1 Examples of strain hardening functions

Usual strain hardening functions are listed in Table 4. 1

Table 4. 1 Empirical model showing the dependency of flow stress[2] on plastic strain

No	Empirical model $h(\varepsilon_p)$	Comment
1	$K\varepsilon_p^n$	Hollomon law, deviate at low strain rate, for high strain rate ε may be treated total as well as plastic strain rate
2	$\sigma_0 + K\varepsilon_p^n$	Ludwik law, ε is plastic strain does not give good fit for wide range
3	$\sigma_0(1 + \varepsilon/b)^n$	Swift generalized power law, suitable for wide range
4	$\sigma_0 + \sigma_\infty [1 - \exp(-b.\varepsilon_p)]$	Voce law
5	$\varepsilon = \frac{\sigma}{E} \left\{ 1 + \alpha \left(\frac{\sigma}{\sigma_0} \right)^{m-1} \right\}$	Ramberg-Osgood equation, considers elasticity
6	$\sigma_0 \tanh\left(\frac{E\varepsilon}{\sigma_0}\right)$	Prager's law for ideally plastic material

4.2.1.2 Examples of thermal softening functions

Thermal softening functions are often of the form,

$$\sigma_{nv}(\varepsilon_p, T) = h(\varepsilon_p)g(T) \quad (4.4)$$

Some of them are listed in Table 4. 2

Table 4. 2 Empirical model showing the dependency of flow stress[2] on temperature

No	Empirical model $g(T)$	Comment
1	$\exp\left(\frac{\beta}{T}\right)$	
2	$1 - \left(\frac{T - T_0}{T_{melt} - T_0}\right)^m$	Johnson-Cook model
3	$\left(\frac{T}{T_c}\right)^{-r}$	Power law

4.2.1.3 Examples of tension/compression asymmetry

Cazacu et al [3] introduce new isotropic yield criteria in the form of

$$\left(|S_1| - kS_1\right)^a + \left(|S_2| - kS_2\right)^a + \left(|S_3| - kS_2\right)^a = F \quad (4.5)$$

Where S_i , $i=1, \dots, 3$ are the principal values of the stress deviator, exponent a , is a positive integer, k , is a material constant and F is the size of yield locus [3] see Fig. 4. 2

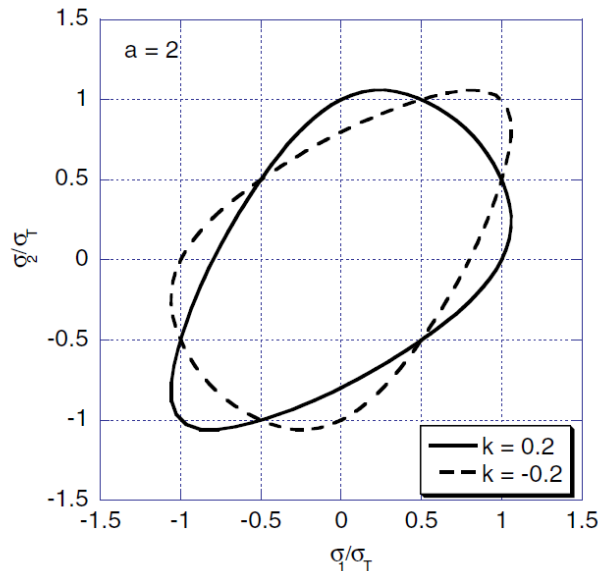


Fig. 4. 2 Plane yield stress loci corresponding to $a=2$ ($k=0.2$) and $a=2$ ($k=-0.2$) [3]

Graft et al [4] had considered the effect of the loading path may be thermally activated mechanism involving mean stress. This approach was retained by Longère et al in his work which lead to the following expression [5]:

$$\sigma_v = \Upsilon \left[\dot{\varepsilon}_p \exp \left(\frac{V_a \sigma_m}{k_b T} \right) \right]^{1/n} \quad (4.6)$$

Where Υ and n are constants of the law, V_a and k_b are constant related to symmetrical behavior, $\dot{\varepsilon}_p$ is plastic strain rate, T is temperature and σ_m is hydrostatic stress

4.2.2 Step 2: Determination of the viscous stress

For a given loading type (compression, tension) and a given temperature

$$\sigma_v(\varepsilon^p, \dot{\varepsilon}^p, T) = \sigma_{eq}(\underline{\underline{\sigma}}) - \sigma_{nv}(\varepsilon^p, T) \quad (4.7)$$

4.2.2.1 Examples of strain rate hardening functions

Strain rate hardening functions are often of the form,

$$\sigma_y(\varepsilon_p, \dot{\varepsilon}_p, T) = h(\varepsilon_p) g(T) z(\dot{\varepsilon}_p) \quad (4.8)$$

Some of them are listed in Table 4. 3

Table 4. 3 Empirical model showing the dependency of flow stress [2] on strain rate

No	Empirical model $z(\dot{\varepsilon}_p)$	Comment
7	$\dot{\varepsilon}_p \exp\left(\frac{Q}{RT}\right)$	Relation considering a strain rate and temperature, Z is Holloman parameter or temperature corrected strain rate
8	$\dot{\varepsilon}_p^m$	Relation considering strain rate and temperature, m is strain rate sensitivity
9	$1 + C \ln\left(\frac{\dot{\varepsilon}_p}{\varepsilon_0}\right)$	Johnson-Cook model, widely used in machining
10	$\left(\frac{\dot{\varepsilon}_p}{\dot{\varepsilon}_0}\right)^m$	Power law

4.2.2.2 Case of Johnson-Cook model

Engineering Johnson-Cook [6] model reads

$$\sigma_y(\varepsilon_p, \dot{\varepsilon}_p, T) = (A + B\varepsilon_p^n) \left(1 + C \ln\left(\frac{\dot{\varepsilon}_p}{\varepsilon_0}\right) \right) \left\{ 1 - \left(\frac{T - T_0}{T_{melt} - T_0} \right)^m \right\} \quad (4.9)$$

Johnson-Cook model is of the product form

$$h(\varepsilon_p) = A + B\varepsilon_p^n; z(\dot{\varepsilon}_p) = 1 + C \ln\left(\frac{\dot{\varepsilon}_p}{\varepsilon_0}\right); g(T) = 1 - \left(\frac{T - T_0}{T_{melt} - T_0}\right)^m \quad (4.10)$$

It can also be rewritten in the form

$$\sigma_y(\varepsilon_p, \dot{\varepsilon}_p, T) = (A + B\varepsilon_p^n) \left\{ 1 - \left(\frac{T - T_0}{T_{melt} - T_0}\right)^m \right\} + (A + B\varepsilon_p^n) C \ln\left(\frac{\dot{\varepsilon}_p}{\varepsilon_0}\right) \left\{ 1 - \left(\frac{T - T_0}{T_{melt} - T_0}\right)^m \right\} \quad (4.11)$$

Or else

$$\sigma_y(\varepsilon_p, \dot{\varepsilon}_p, T) = \sigma_{nv}(\varepsilon^p, T) + \sigma_v(\varepsilon^p, \dot{\varepsilon}^p, T) \quad (4.12)$$

where

$$\begin{cases} \sigma_{nv}(\varepsilon^p, T) = (A + B\varepsilon_p^n) \left\{ 1 - \left(\frac{T - T_0}{T_{melt} - T_0}\right)^m \right\} \\ \sigma_v(\varepsilon^p, \dot{\varepsilon}^p, T) = (A + B\varepsilon_p^n) C \ln\left(\frac{\dot{\varepsilon}_p}{\varepsilon_0}\right) \left\{ 1 - \left(\frac{T - T_0}{T_{melt} - T_0}\right)^m \right\} \end{cases} \quad (4.13)$$

Johnson-Cook model accordingly assumes the dependence of the viscous stress on plastic strain, strain rate and temperature. If the viscous stress is shown to be independent of plastic strain and temperature, Johnson-Cook model cannot apply.

4.3 Application to AA2024 and AA7175

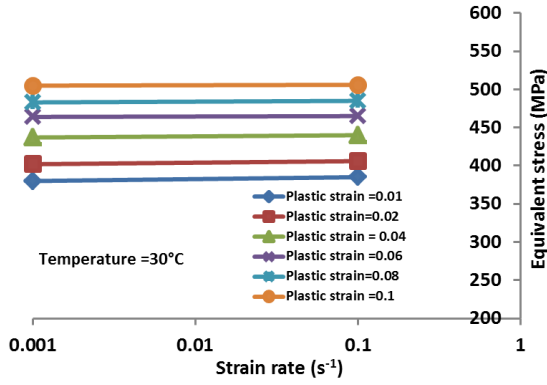
In this section is applied the above outlined modelling procedure for the materials under consideration, viz. AA2024 and AA7175 aluminium alloys.

4.3.1 AA2024

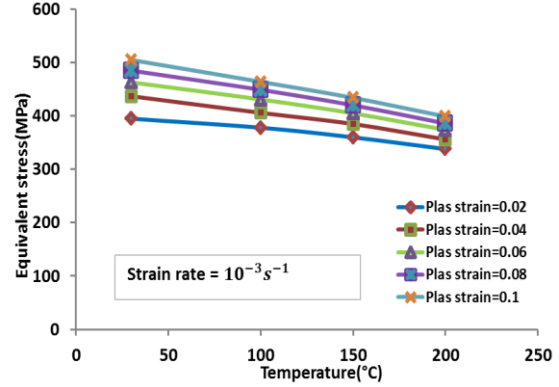
Modelling for AA2024 is considered into two main parts which are global approach and modelling oriented approach.

4.3.1.1 Global perspective for AA2024

Fig. 4. 3 depicts the influence of plastic strain rate and temperature on equivalent stress for AA2024. Both plastic strain rate and temperature have influence on equivalent stress. The latter equivalent stress is seen to increase with increase of strain rate, see Fig. 4. 3 (a) whereas gradual decrease in equivalent is seen with the increase of the temperature, see Fig. 4. 3(b). According to Fig. 4. 3 (a-b), strain hardening is only weakly influenced by plastic strain rate and temperature.



a. Equivalent stress vs strain rate at different plastic strain amounts



b. Equivalent stress vs temperature at different plastic strain amounts

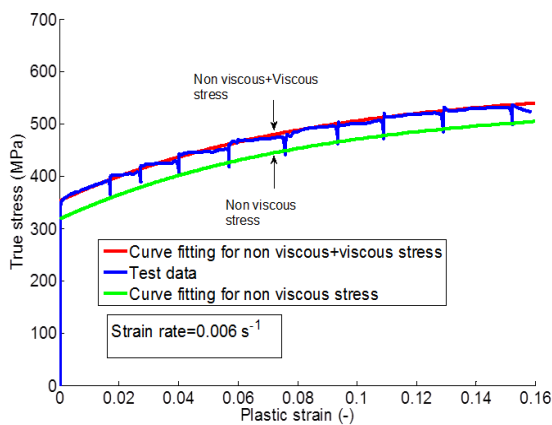
Fig. 4. 3 (a) Influence of plastic strain at different strain rate on equivalent stress (b) Influence of plastic strain at different temperature on equivalent stress in tension

4.3.1.2 Constitutive modelling for AA2024

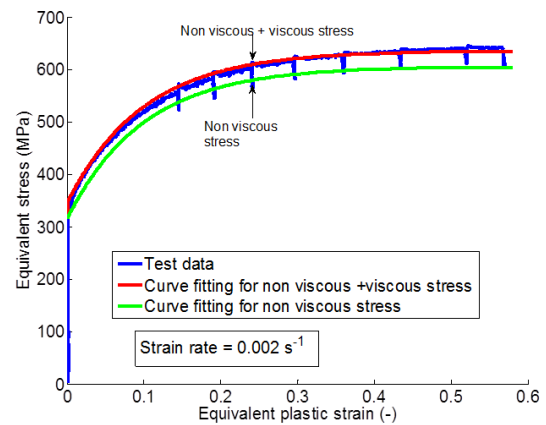
The constitutive modelling follows the two-step procedure.

4.3.1.2.1 Step 1: Non-viscous stress for AA2024 and further strain hardening and thermal softening

The relaxation tests are used for determining the non-viscous stress, as depicted in Fig. 4. 4. The blue curve is the experimental equivalent stress for a given strain rate, temperature and loading type, the red curve its numerical approximation, and the green curve joins the stress values after relaxation. The green curve is thus the non-viscous (rate independent) stress for a given temperature and loading type, see (4.3)



a. Quasi static tension



b. Quasi static compression

Fig. 4. 4 Curve fitting method to determine viscous stress

According to Fig. 4. 4, the non-viscous stress in(4.3) can be written in term of R_0 and R_f ,

$$\sigma_{nv}(\varepsilon^p, T) = R_0(T) + R_f(T) \left[1 - \exp(-b(T) \varepsilon_{eq}^p) \right] \quad (4.14)$$

Where, R_0 , initial stress, R_f , is difference between saturated stress and initial stress. In order to estimate the parameter R_0 and R_f in (4.15) and (4.16), the curve for initial stress versus temperature and difference between initial stress and saturated stress versus temperature was plotted, see Fig. 4. 5 Equivalent stress vs temperature for initial stress, R_0 and saturated stress minus initial stress, R_f .

Initial stress and difference between initial stress and saturated stress can accordingly be expressed as;

$$R_0 = R_1 \exp(\alpha T) \quad (4.15)$$

$$R_f = R_2 \exp(\beta T) \quad (4.16)$$

R_1, R_2, α and β are constants. Initial approximation for the value of R_0 and R_f was from the stress strain relationship of tension test at elevated temperature. Fig. 4. 5 shows the relationship for R_0 (blue curve) and R_f (red curve) as a function of temperature for AA2024.

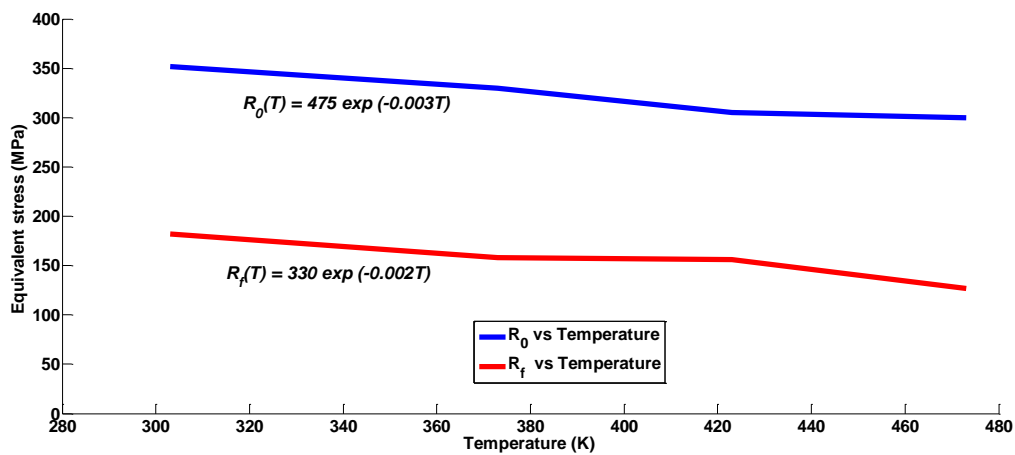


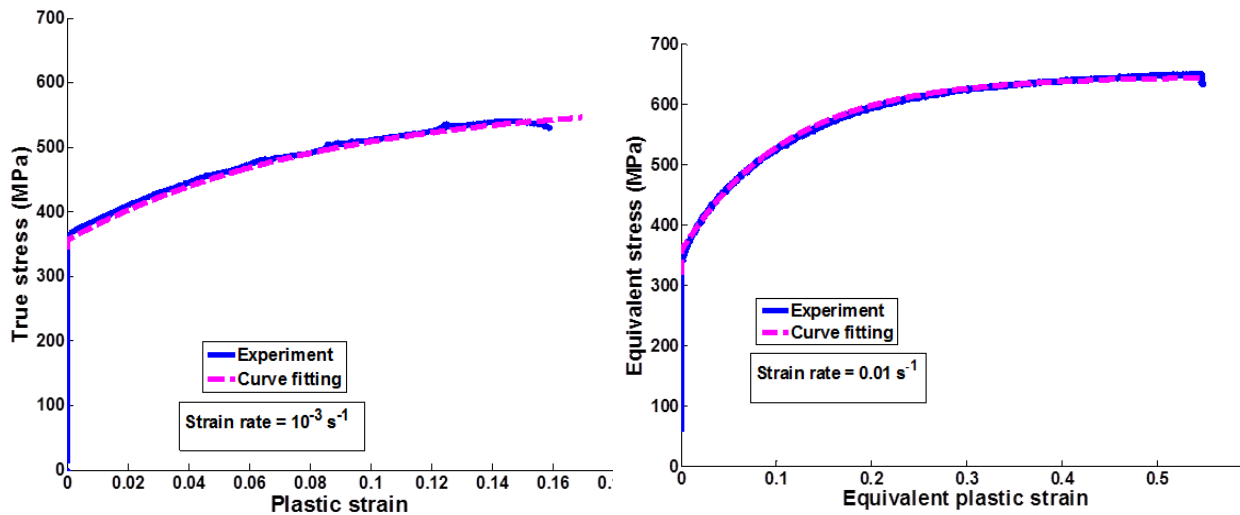
Fig. 4. 5 Equivalent stress vs temperature for initial stress, R_0 and saturated stress minus initial stress, R_f .

R_0 and R_f is given by(4.17) and (4.18) based on relationship from Fig. 4. 5

$$R_0(T) = 475 \exp(-0.003T) \quad (4.17)$$

$$R_f(T) = 330 \exp(-0.002T) \quad (4.18)$$

The Matlab code was developed based on (4.14) in order to verify the value for corresponding variables by applying curve fitting method. Fig. 4. 6 (a) and Fig. 4. 6 (b) shows example of the curve fitting method by applying matlab code for tension and compression test at different strain rates for AA2024. From the curve fitting method value for parameter R_1, R_2, α and β were determined and tabulated in Table 4.4. It is to be noted that these constants are different for tension and compression.

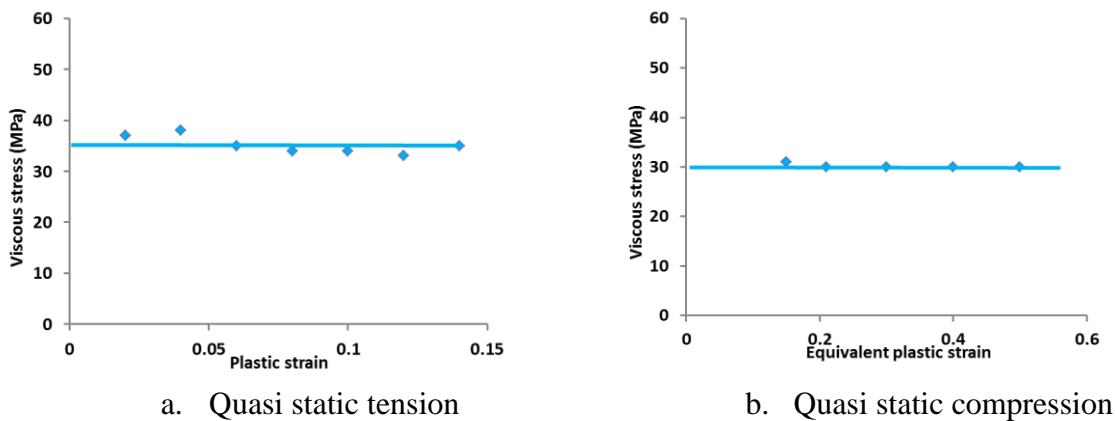


a. Quasi static tension
 b. Quasi static compression
Fig. 4. 6 Curve fitting for true stress vs plastic strain (AA2024)

4.3.1.2.2 Step 2: Viscous stress for AA2024

The viscous stress is deduced for each strain rate from (4.3).

Fig. 4. 7(a) and (b) show the viscous stress versus plastic strain for tension and compression in quasi static range respectively. The curve shows that the viscous stress is independent of plastic strain.



a. Quasi static tension
 b. Quasi static compression

Fig. 4. 7 viscous stress versus plastic strain

Fig. 4. 8 shows the viscous stress as a function of temperature for AA2024. The viscous stress remains constant with the increasing of the temperature at considered temperature range. The viscous stress for this considered temperature range is 14 MPa.

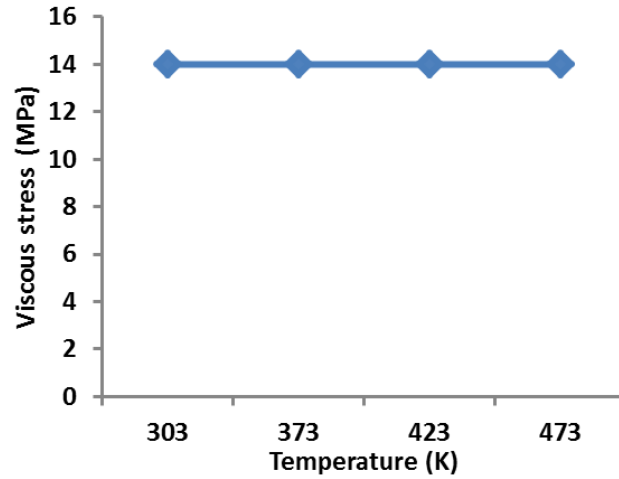
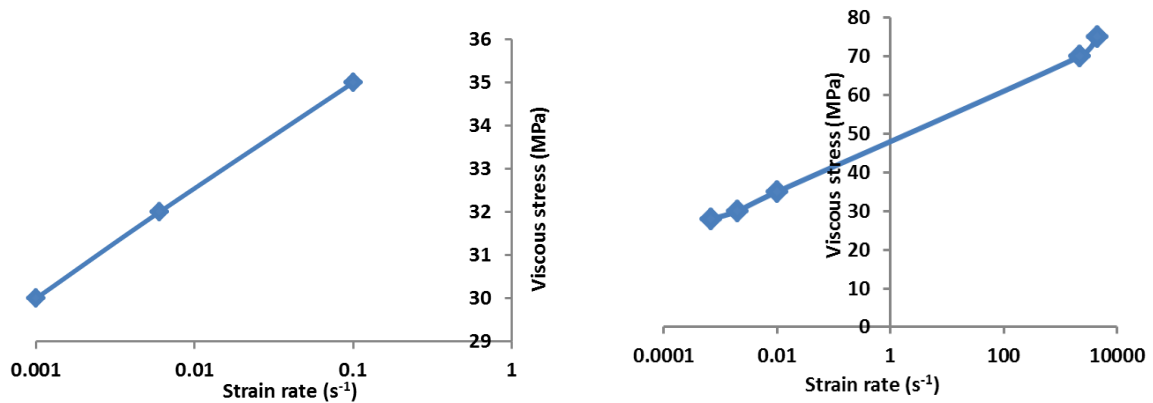


Fig. 4. 8 Viscous stress vs temperature

Fig. 4. 9 (a) and Fig. 4. 9 (b) show the viscous stress versus strain rate (log scale) for tension and compression test. The viscous stress is rate dependent and given by power law as shown in (4.19), where A and n are constants.

$$\sigma_v = A(\dot{\epsilon}^p)^n \quad (4.19)$$



a. Viscous stress vs strain rate for tension

b. Viscous stress vs strain rate for compression

Fig. 4. 9 Viscous stress vs strain rate for (a) Tension and (b) Compression

Viscous stress versus strain rate for tension and compression test is given by(4.20) and (4.21).

$$\sigma_{v(Tension)} = 37.8(\dot{\epsilon}^p)^{0.03} \quad (4.20)$$

$$\sigma_{v(Compression)} = 44.5(\dot{\epsilon}^p)^{0.061} \quad (4.21)$$

It is to be noted that as the viscous stress is independent of the plastic strain and temperature, hence Johnson-Cook model cannot apply, see subsection 4.2.2.2.

Fig. 4. 10 shows the influence of parameter b on temperature. Parameter b, remains constant for AA2024 and is not influenced by temperature.

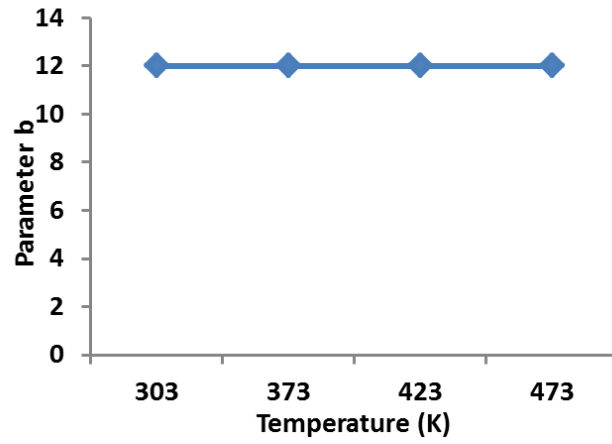


Fig. 4. 10 Parameter b vs temperature

Table 4. 4 shows the constants for AA2024.

Table 4. 4 Constants for AA2024

Constants	Tension ($\chi = \frac{1}{3}$)	Compression ($\chi = -\frac{1}{3}$)
R_1	445	428
R_2	390	530
α	-1e-3	-1e-3
β	-2e-3	-2e-3
b	12	12
A	37.8	44.5
n	0.03	0.061

(4.22) and (4.23) are the final equations to describe the equivalent stress under tension and compression loading respectively.

$$\sigma_{eq}(\varepsilon^p, \dot{\varepsilon}^p, T) = 445(e^{-0.001T}) + 390(e^{-0.002T})[1 - \exp(-12\varepsilon^p)] + 37.8(\dot{\varepsilon}^p)^{0.03} \quad (4.22)$$

$$\sigma_{eq}(\varepsilon^p, \dot{\varepsilon}^p, T) = 428(e^{-0.001T}) + 530(e^{-0.002T})[1 - \exp(-12\varepsilon^p)] + 44.5(\dot{\varepsilon}^p)^{0.061} \quad (4.23)$$

4.3.1.3 Curve fitting for AA2024

For the validation of the constitutive model, the proposed model was compared to the experimental results. Fig. 4. 11 shows the comparison of the modelling and the experimental results for various strain rates under tension and compression loading. Fig. 4. 11(a) and Fig. 4. 11(b) show the flow curve comparison for tension test at strain rate of 10^{-3} and 10^{-1} s^{-1} respectively. Fig. 4. 11(c) and Fig. 4. 11(d) show the comparison for compression loading at strain rate of 10^{-3} and 4500 s^{-1} .

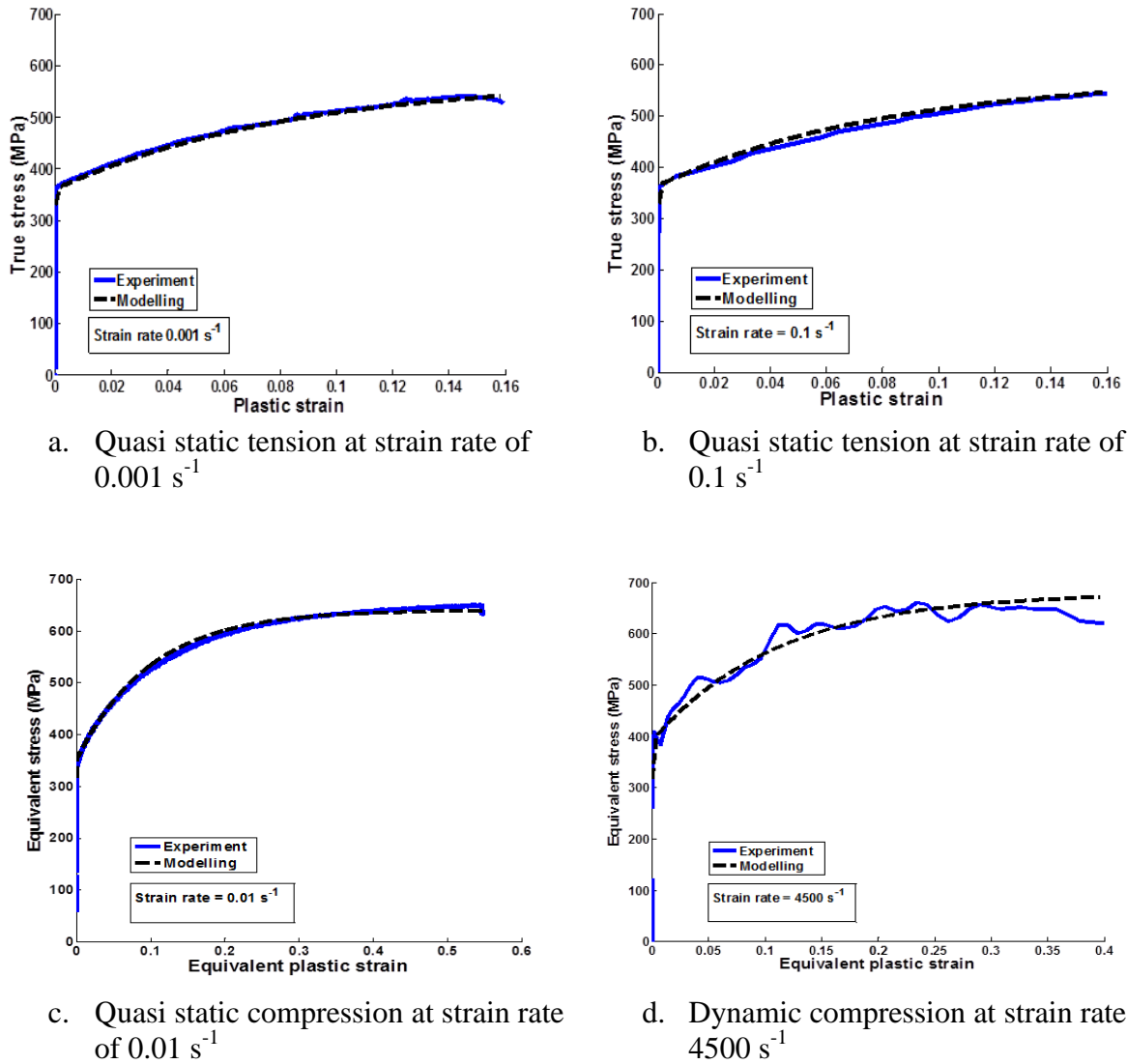
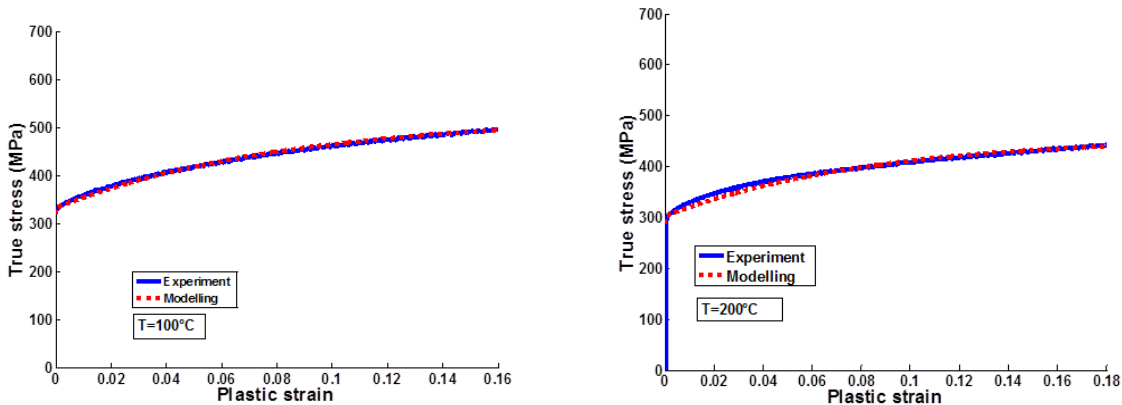


Fig. 4. 11 Comparison of the modelling and experimental results for flow curve at various strain rate range under tension and compression loading

Fig. 4. 12(a) and Fig. 4. 12(b) show superimpose of flow curve for 100°C and 200°C respectively under quasi static tension loading.



a. Quasi static tension at temperature of 100°C

b. Quasi static tension at temperature of 200°C

Fig. 4. 12 Comparison of the modelling and experimental results for flow curve at different temperature

4.3.2 AA7175

Same approach of modelling as applied to AA2024 was applied to model AA7175

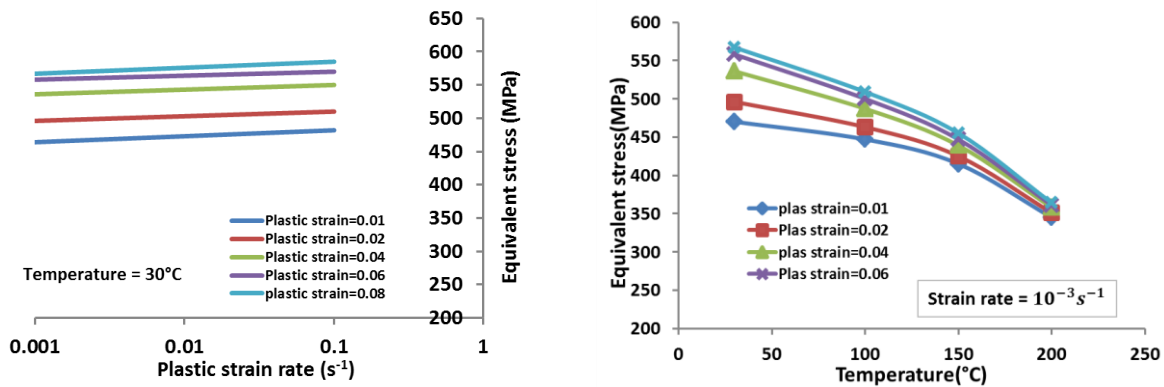
4.3.2.1 Global perspective for AA7175

Fig. 4. 13 depicts the influence of plastic strain rate and temperature on equivalent stress at different plastic strain.

Fig. 4. 13 (a) shows equivalent stress becomes saturated after plastic strain of 0.02, where the curve starts to overlap each other.

Fig. 4. 13 (b) depicts equivalent stress gradually decreasing up to 150°C and dramatically until 200°C for different plastic strain amounts.

According to Fig. 4.13 (a-b), strain hardening is weakly influenced by strain rate and strongly influenced by temperature.



a. True stress vs strain rate at different plastic strain
 b. True stress vs temperature at different plastic strain

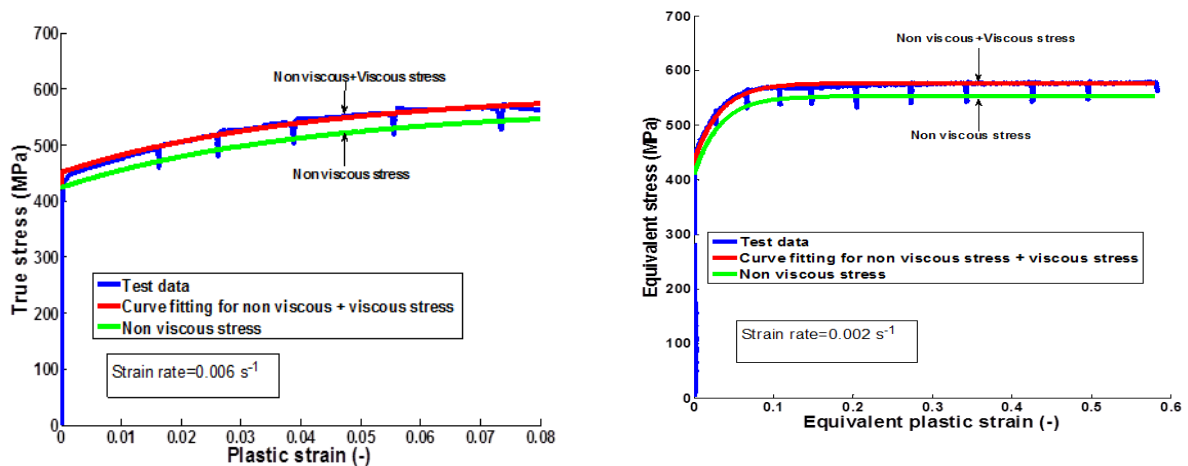
Fig. 4. 13 (a) Influence of plastic strain at different strain rate on equivalent stress (b) Influence of plastic strain at different temperature on equivalent stress in tension

4.3.2.2 Constitutive modelling for AA7175

The equation of flow stress is considered into two parts as discussed earlier for AA2024.

4.3.2.2.1 Step 1: Non-viscous stress for AA7175 and further strain hardening and thermal softening

The curve fitting method was applied to various ranges of strain rates in tension and compression in order to determine the viscous stress. Fig. 4. 14 shows the results from relaxation test, superimposed by non-viscous plus viscous part (red curve) and non -viscous part (green curve) for quasi static tension and quasi static compression respectively.



a. Quasi static tension
 b. Quasi static compression

Fig. 4. 14 Curve fitting method to determine viscous stress

By applying (4.3), non-viscous stress was determined, for AA7175.

In order to estimate the parameter R_0 and R_f the curve for initial stress versus temperature and difference between initial stress and saturated stress versus temperature was plotted. Initial stress and difference between initial stress and saturated stress were expressed in quadratic function as;

$$R_0(T) = R_1T^2 + R_2T + R_3 \quad (4.24)$$

$$R_f(T) = R_4T^2 + R_5T + R_6 \quad (4.25)$$

The relationship is a quadratic function due to the best fitting for the curve, see Fig. 4. 15.

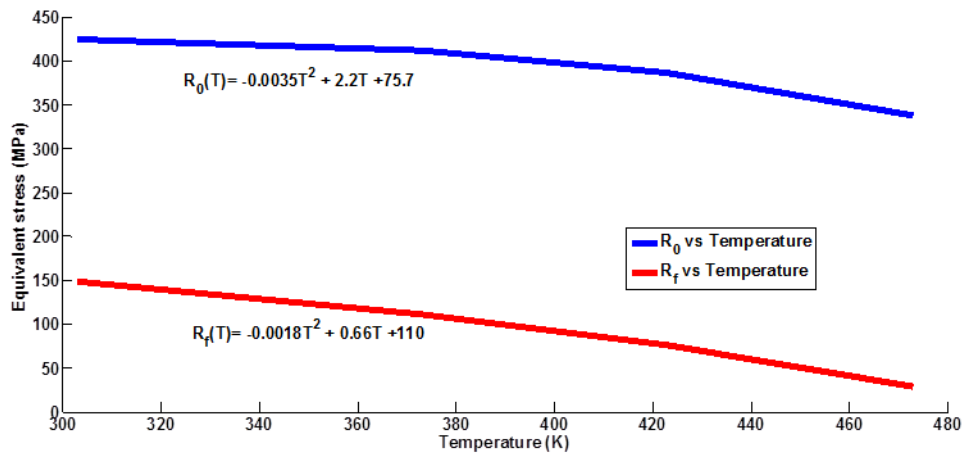


Fig. 4. 15 Equivalent stress vs temperature for initial stress, R_0 and saturated stress minus initial stress, R_f .

$$R_0(T) = -0.0035T^2 + 2.2T + 75.7 \quad (4.26)$$

$$R_f(T) = -0.0018T^2 + 0.66T + 110 \quad (4.27)$$

The Matlab code was developed based on (4.14) and in order to verify the value for appropriate variables by applying curve fitting method. Fig. 4. 16(a) and Fig. 4. 16 (b) shows example of the curve fitting method by applying matlab code for tension and compression test at different strain rate for AA7175. From the curve fitting method value for parameter R_1 , R_2 , R_3 , R_4 , R_5 and R_6 were determined and tabulated in Table 4. 5. It is to be noted that this constants are same for tension and compression.

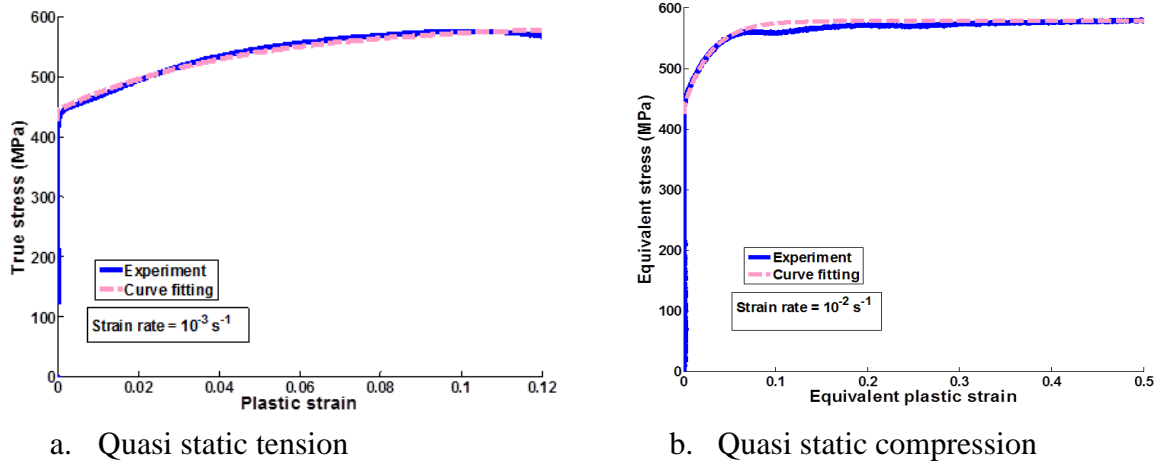


Fig. 4. 16 Curve fitting for flow curve (AA7175)

4.3.2.2.2 Step 2: Viscous stress for AA7175

The viscous stress is deduced for each strain rate from (4.3). Fig. 4. 17(a) and Fig. 4. 17(b) show the viscous stress versus plastic strain for tension and compression in quasi static range respectively. The curve shows that the viscous stress is independent of plastic strain.

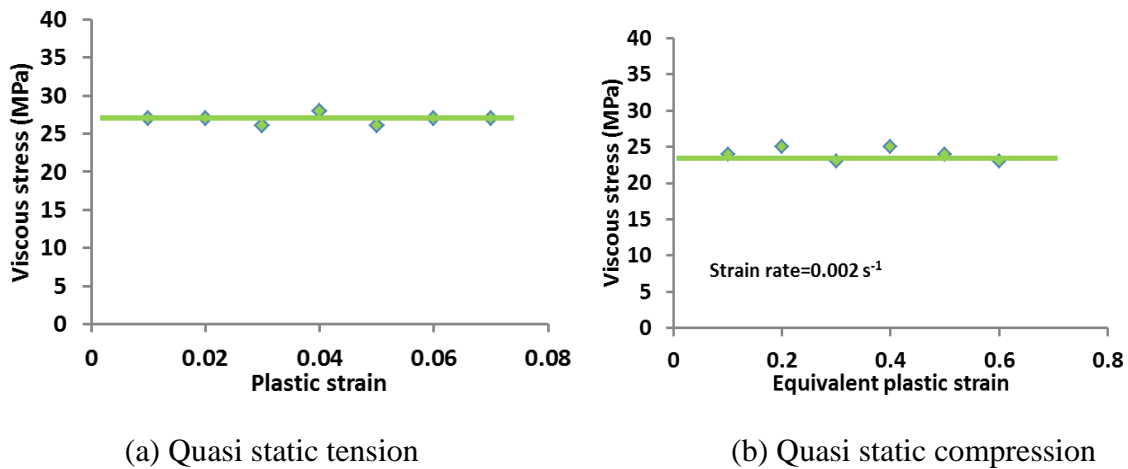


Fig. 4. 17 viscous stress versus plastic strain

Fig. 4. 18 shows the viscous stress as a function of temperature for AA7175. The viscous stress remains constant with the increasing of the temperature at considered temperature range. The viscous stress for this considered temperature range is 20 MPa.

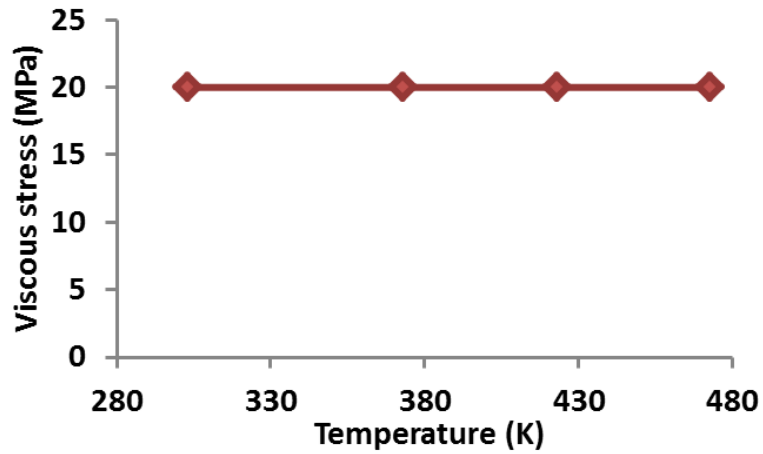


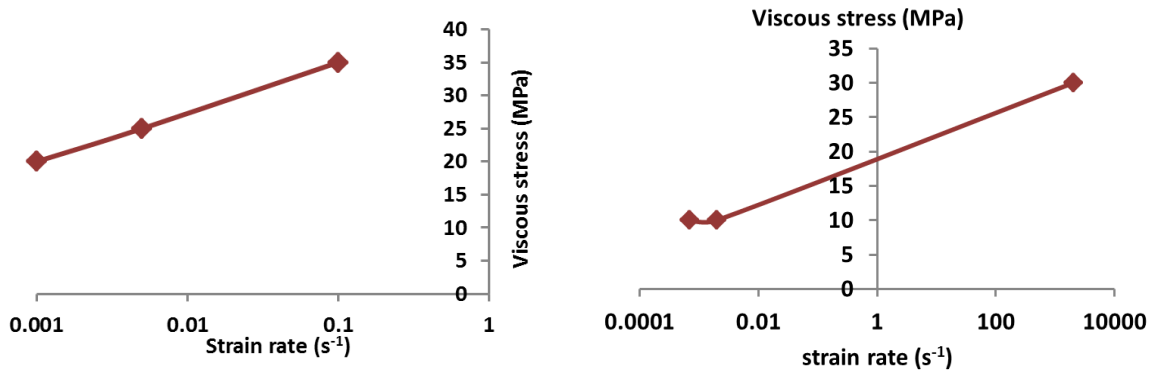
Fig. 4. 18 Viscous stress vs temperature

Fig. 4. 19(a) and Fig. 4. 19(b) show the viscous stress versus strain rate in tension and compression loading respectively. Power law type of equation in tension loading and exponential type of equation for compression loading was obtained. With B , η , C , p and ψ are constants. To be noted that for tension the tests were carried out at quasi static range whereas for compression it covered quasi static to dynamic range.

$$\sigma_{v(Tension)} = B(\dot{\epsilon}^p)^\eta \quad (4.28)$$

$$\sigma_{v(compression)} = C \exp(\psi \dot{\epsilon}^p) \quad (4.29)$$

Once again, as the viscous stress is independent of the plastic strain and temperature, Johnson-Cook model cannot apply, see subsection 4.2.2.2.



a. Viscous stress vs strain rate for tension

b. Viscous stress vs strain rate for compression

Fig. 4. 19 Viscous stress vs strain rate (a) for tension and (b) compression test.

$$\sigma_{v(Tension)} = 46.5(\dot{\epsilon}^p)^{0.12} \quad (4.30)$$

$$\sigma_{v(compression)} = 10.4 \exp(0.0005\dot{\epsilon}^p) \quad (4.31)$$

Fig. 4. 20 shows the influence of temperature on parameter b and shown by(4.32).

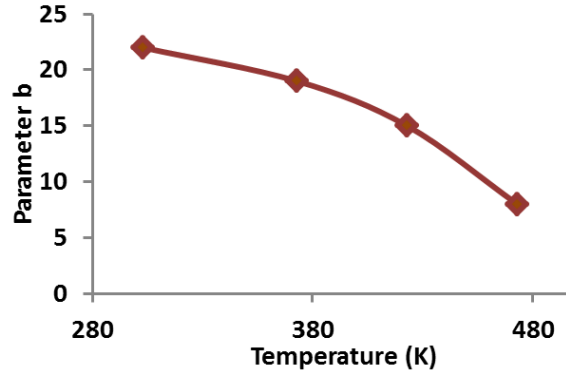


Fig. 4. 20 Parameter b vs temperature

(4.32)shows the relationship of the parameter, b, with temperature where, r,s, and t are constants that found by the best fit for the experimental curves as shown in (4.33).

$$b = -rT^2 + sT - t \quad (4.32)$$

$$b = -0.0004T^2 + 0.25T - 14.585 \quad (4.33)$$

Table 4. 5 shows the constants for AA7175.

Table 4. 5 Constants for AA7175

Constants	Tension ($\chi = \frac{1}{3}$)	Compression ($\chi = -\frac{1}{3}$)
R ₁	-0.0035	-0.0035
R ₂	2.2	2.2
R ₃	75.7	75.7
R ₄	-0.0018	-0.0018
R ₅	0.66	0.66
R ₆	110	110
B	46.5	-
C	-	10.4
η	0.12	-
ψ	-	0.0005
r	-0.0004	-0.0004
s	0.25	0.25
t	-14.585	-14.585

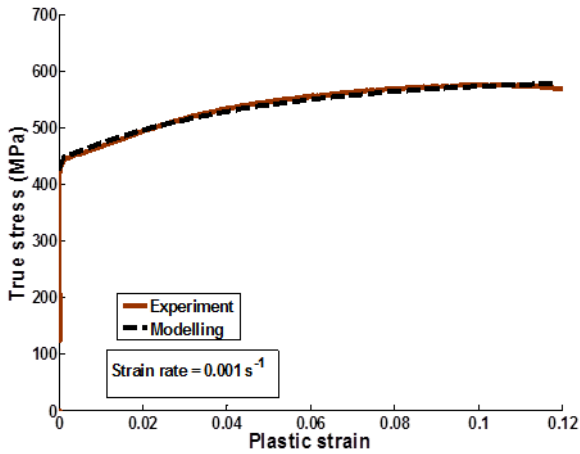
(4.34) and (4.35) are the final equation to describe the equivalent stress for tension and compression loading respectively for AA7175.

$$\sigma_{eq}(\varepsilon^p, \dot{\varepsilon}^p, T) = (-0.0035T^2 + 2.2T + 75.7) + (-0.0018T^2 + 0.66T + 110) \left[1 - \exp((-0.0004T^2 + 0.25T - 14.585))\varepsilon^p \right] + 46.5(\dot{\varepsilon}^p)^{0.12} \quad (4.34)$$

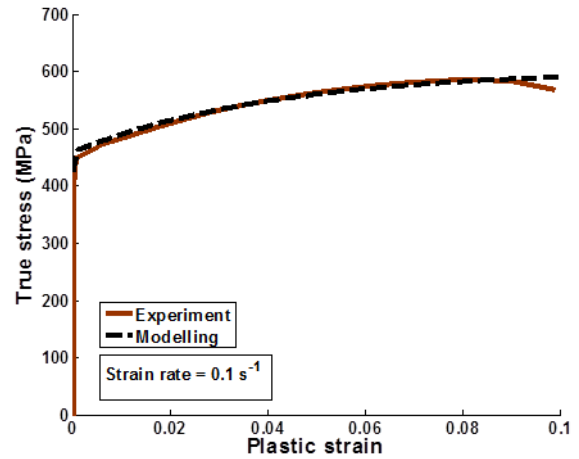
$$\sigma_{eq}(\varepsilon^p, \dot{\varepsilon}^p, T) = (-0.0035T^2 + 2.2T + 75.7) + (-0.0018T^2 + 0.66T + 110) \left[1 - \exp((-0.0004T^2 + 0.25T - 14.585))\varepsilon^p \right] + 10.4\exp(0.0005\dot{\varepsilon}^p) \quad (4.35)$$

4.3.2.3 Curve fitting for AA7175

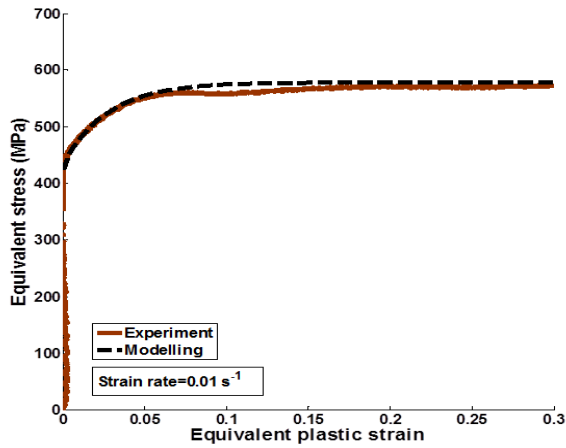
The following curve shows the fitting for experimental and modelling for various strain rates and temperatures for both alloys. Fig. 4. 21(a) and Fig. 4. 21(b) show the comparison of experimental and modelling at strain rate of 10^{-3} s^{-1} and 10^{-1} s^{-1} respectively for tension load. Fig. 4. 21 (c) and Fig. 4. 21 (d) show the comparison of experimental and modelling at strain rate of 10^{-3} s^{-1} and 4500 s^{-1} respectively for compression load. The approximated curve is above the experimental one because self-heating induced softening is not accounted for in this first attempt of modelling.



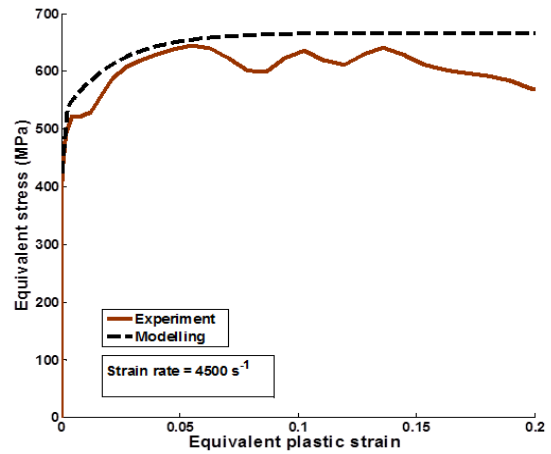
a. Quasi static tension at strain rate of 0.001 s^{-1}



b. Quasi static tension at strain rate of 0.1 s^{-1}



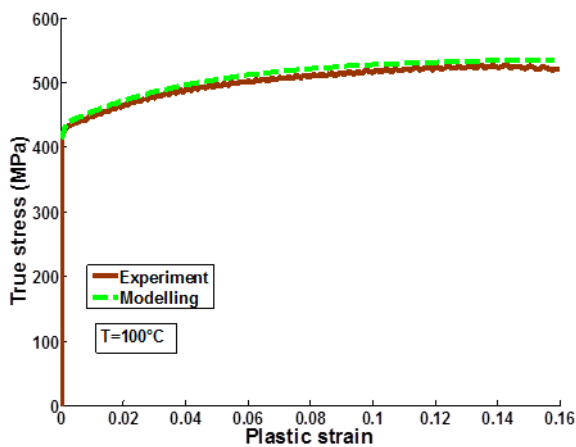
c. Quasi static compression at strain rate of 0.01 s^{-1}



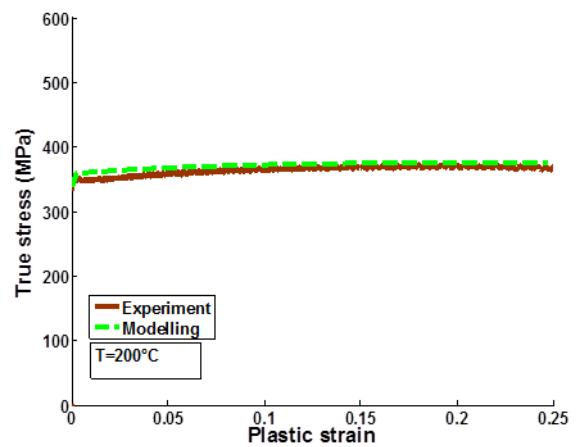
d. Dynamic compression at strain rate of 4500 s^{-1}

Fig. 4. 21 Comparison of the modelling and experimental results for flow curve at various strain rate range under tension and compression loading

Fig. 4. 22(b) shows comparison for experimental and modelling for temperature 100°C and 200°C respectively for quasi static tension loading.



a. Quasi static tension at temperature of 100°C



b. Quasi static tension at temperature of 200°C

Fig. 4. 22 Comparison of the modelling and experimental results for flow curve at different temperature

4.4 Conclusion

In this chapter we can see the influence of the variables on flow curve. The hardening parameters and viscous part of the stress were computed and presented in constitutive equations for both alloys. The constitutive equations were mostly the same for tension and

compression but with different constants for each alloy. Good agreement was seen between the constitutive modelling and experimental results in the considered strain rate and temperature range. In fact, the present constitutive equation is still far from representing the complete characterization of material response. The experimental result for temperature effect is only considered at one strain rate and the specimen only considered at the machine rolling direction without considering at transverse rolling direction. In addition, self-heating due to plastic dissipation needs to be accounted for in future works to describe thermal softening during ongoing deformation.

4.5 References

- [1] Jean-Philippe Créte, “Traitement numérique de la fissuration d’une structure navale.,” Université de Bretagne Sud, 2013.
- [2] U. S. Dixit, S. N. Joshi, and J. P. Davim, “Incorporation of material behavior in modeling of metal forming and machining processes: A review,” *Mater. Des.*, vol. 32, no. 7, pp. 3655–3670, 2011.
- [3] O. Cazacu, B. Plunkett, and F. Barlat, “Orthotropic yield criterion for hexagonal closed packed metals,” *Int. J. Plast.*, vol. 22, no. 7, pp. 1171–1194, 2006.
- [4] S. Graff, S. Forest, J. L. Strudel, C. Prioul, P. Pilvin, and J. L. Béchade, “Strain localization phenomena associated with static and dynamic strain ageing in notched specimens: Experiments and finite element simulations,” *Mater. Sci. Eng. A*, vol. 387–389, no. 1–2 SPEC. ISS., pp. 181–185, 2004.
- [5] P. Longère, A. G. Geffroy, B. Leblé, and A. Dragon, *Modeling the transition between dense metal and damaged (microporous) metal viscoplasticity*, vol. 21, no. 7. 2012.
- [6] G. R. Johnson, and W. H. Cook, “A constitutive model and data for metals subjected to large strains, high strain rates and high temperatures,” in *Proceedings of the 7th International Symposium on Ballistic*, P. 541, The Hague, The Netherland, 1983.

5. Conclusions and future scopes

5.1 Conclusion on thermo-mechanical characterization

In order to characterize the thermo-mechanical behaviour of the materials under consideration, viz. AA2024 and AA7175 aluminium alloys, an experimental campaign was carried out at various strain rates and temperatures. In the Quasi static range i.e between 10^{-3} and 10^{-1} s^{-1} , at ambient temperature, both AA2024 and AA7175 show no significant strain rate dependence. However when compared to higher strain rate, i.e. 4500 s^{-1} , during dynamic compression test, both alloys exhibit slight strain rate sensitivity which is still not very significant. Flow curve in dynamic compression test depicts a sudden drop in stress at plastic strain of 0.2 for AA7175 whereas the stress keep on increasing for AA2024.

Quasi static tension tests at strain rate of 10^{-3} s^{-1} carrying out at elevated temperatures of 100°C , 150°C and 200°C show that both alloys are strongly influenced by temperature especially AA7175. The results shows the gradual decrease in initial yield stress for AA2024 until 200°C whereas for AA7175 after 150°C the yield stress decrease dramatically. AA2024 exhibit a strain hardening up to 200°C whereas for AA7175 at temperature of 150°C there is very small portion of strain hardening and at 200°C no strain hardening at all.

Shear compression test results shows larger load required to rupture a Couque type specimen compared to Meyer for both in quasi static and dynamic range of tests, as expected. Indeed, As explained earlier in the chapter of thermomechanical characterization, stress triaxiality ratio (STR) for Meyer and Couque type specimen is close to -0.1 and -0.5 respectively. The microstructure observation of the crack lip shows the formation of adiabatic shear band (ASB) for AA7175 for dynamic shear compression tests. It is To be noted that there is no evidence of ASB on crack lip for AA2024.

Microstructure of AA2024 remains quasi homogeneous after both quasi static and dynamic compression test whereas AA7175 depicts zones of weakly heterogeneous deformation for quasi static compression and ASB for dynamic compression. Dynamic shear compression specimen shows shear induced Mode II failure for both alloys on Meyer shape specimens and combination of shear induced Mode II and tension induced Mode I for Couque shape. For dynamic shear compression test, Couque shape specimen evidenced an ASB for AA7175 whereas there was no evidence of ASB on AA2024.

5.2 Conclusion on crack arrest capability of aluminium alloys

The Crack arrest capability of the two aluminium alloys under consideration was experimentally studied by carrying out Kalthof and Winkler (KW) type impact tests on double notched plate specimens. The aim is to identify for both a critical impact velocity, record the crack propagation during impact loading using a high-speed camera and determine the micro-mechanisms of failure.

For the configurations considered, the Critical impact velocity for AA2024 and AA7175 for crack arrest inside the material is close to 150 m.s^{-1} and 130 m.s^{-1} respectively.

The Analysis of recorded frames during projectile and plate interaction shows the appearance of white band as the likely optical signature of shear localization in AA7175 for impact velocity of 164 m.s^{-1} and 230 m.s^{-1} . Further analysis on crack lip shows that the white band is indeed an ASB. As Adiabatic shear bands are known to favour premature failure they may explain the low value of critical impact velocity for AA7175 when compared with the impact velocity for AA2024. The direction of the crack which is arrested inside the material for both alloys, is initially collinear with the notch direction before following a slight angle so as the cracks would converge if the plate were infinitely wide evidencing cracks propagation under predominant shear control Mode II. A crack bifurcation is observed for arrested cracks, i.e. for impact velocity lower than critical velocity. The analysis of wave interactions during the impact-induced loading shows that the plate and the cracks are subject to complex, alternate shear and tension loading. The crack bifurcation may thus more probably result from the turn of predominant shear wave-induced loading to predominant tension wave-induced loading, as a consequence of changes in the loading path and not as a consequence of changes in the micro-mechanisms (e.g ductile to brittle).

Microstructural observations on fractured surface reveal that the mechanism of the failure is dominated by flat shear (Mode II) at the fracture initiation and followed by dimple cluster (Mode I) for AA2024 whereas for AA7175 the fracture is dominated by flat shear surface (Mode II).

5.3 Conclusion on constitutive modelling

A Constitutive model has been developed taking into account the combined effects of plastic strain, strain rate and temperature. Generally the model shows good agreement with the experimental results in term of true stress vs. plastic strain relationship at considered strain rate and temperature range. In fact, the present constitutive model needs still further improvement to reproduce the complete material response. Indeed, the experimental results only considered the rolling direction and does not yet reproduce the asymmetry between tension and compression.

5.4 Future works on thermomechanical characterization

A complementary experimental campaign should consider tension tests at high strain rate. Tensile Hopkinson bar is required to characterize the material in high strain rate tension loading. Tension and compression tests at low temperatures should also be done.

5.5 Future works on crack arrest capability

The impact tests should be carried out at temperatures of -50°C and 70°C . This is important because the real working environment of the aircraft structure is in that particular temperature range. The usage of more powerful camera with higher resolution is required to record the projectile and plate interaction and perform digital image correlation.

5.6 Future works on constitutive modelling

Constitutive equations should be unified and represent the material behaviour for both tension and compression loading.

A fracture criterion needs to complete the constitutive model and should take into account the machine rolling direction of the sheet metal and stress triaxiality ratio in order to have a better representation of the materials behaviour.

In addition, self-heating due to plastic dissipation under high strain rate loading needs to be accounted for in future works to describe thermal softening during ongoing deformation.

Finally damage parameter should be introduced to predict the damage.

Blank page

Bibliography

- Abrate, S. (2016). Soft impacts on aerospace structures. *Progress in Aerospace Sciences*, 81, 1–17. <https://doi.org/10.1016/j.paerosci.2015.11.005>
- Achouri, M., Germain, G., Dal Santo, P., & Saidane, D. (2013). Experimental characterization and numerical modeling of micromechanical damage under different stress states. *Materials and Design*, 50, 207–222. <https://doi.org/10.1016/j.matdes.2013.02.075>
- Aerospace Supply Chain & Raw Material Outlook. (2014). Retrieved from <https://docplayer.net/7341132-Aerospace-supply-chain-raw-material-outlook.html>
- Allan, J. R. (2000). The costs of bird strikes and bird strike prevention. *Human Conflicts with Wildlife: Economic Considerations*, (August), 147–153. Retrieved from <http://digitalcommons.unl.edu/nwrchumanconflicts/18/>
- Bao, Y. (2003). *Prediction of ductile crack formation in Prediction of ductile crack formation in uncracked bodies*. Massachusetts Institute of Technology.
- Bao, Y., & Wierzbicki, T. (2004). On fracture locus in the equivalent strain and stress triaxiality space. *International Journal of Mechanical Sciences*, 46(1), 81–98. <https://doi.org/10.1016/j.ijmecsci.2004.02.006>
- Blackwell, B. F., DeVault, T. L., Fernández-Juricic, E., & Dolbeer, R. A. (2009). Wildlife collisions with aircraft: A missing component of land-use planning for airports. *Landscape and Urban Planning*, 93(1), 1–9. <https://doi.org/10.1016/j.landurbplan.2009.07.005>
- Bradley Dodd, Y. B. (2015). *Introduction to Adiabatic shear localization* (Revised Ed). Imperial College Press.
- Bridgman, P. W. (1952). *Studies in large plastic flow and fracture*. New York: McGraw-hill.
- Cause of MH17 crash by Dutch Safety Board. (2015). Retrieved from https://www.google.com.my/search?q=mh17&source=lnms&tbm=isch&sa=X&ved=0ahUKEwjP1LfA19vdAhUN-YUKHWN0BRgQ_AUIDigB&biw=1920&bih=945#imgrc=RkLdzNOdbson2M
- Cazacu, O., Plunkett, B., & Barlat, F. (2006). Orthotropic yield criterion for hexagonal closed packed metals. *International Journal of Plasticity*, 22(7), 1171–1194. <https://doi.org/10.1016/j.ijplas.2005.06.001>
- Chen, G., Lu, L., Ren, C., & Ge, X. (2018). Temperature dependent negative to positive strain rate sensitivity and compression behavior for 2024-T351 aluminum alloy. *Journal of Alloys and Compounds*, 765, 569–585. <https://doi.org/10.1016/j.jallcom.2018.06.196>
- Dixit, U. S., Joshi, S. N., & Davim, J. P. (2011). Incorporation of material behavior in modeling of metal forming and machining processes: A review. *Materials and Design*, 32(7), 3655–3670. <https://doi.org/10.1016/j.matdes.2011.03.049>
- Dormeval, Richard & Pierre Ansart, J. (1985). Adiabatic Shearing: Influence of Predeformation.. *Journal de Physique (Paris), Colloque*. 46. 299-306. *Journal de*

- Physique(Paris)*, 46, 299–306.
- Dursun, T., & Soutis, C. (2014). Recent developments in advanced aircraft aluminium alloys. *Materials and Design*, 56, 862–871. <https://doi.org/10.1016/j.matdes.2013.12.002>
- Edwards, N. J., Song, W., Cimpoeru, S. J., Ruan, D., Lu, G., & Herzig, N. (2018). Mechanical and microstructural properties of 2024-T351 aluminium using a hat-shaped specimen at high strain rates. *Materials Science and Engineering A*, 720(February), 203–213. <https://doi.org/10.1016/j.msea.2018.02.049>
- Flight safety Australia. (2017). Retrieved from <https://www.flightsafetyaustralia.com/2017/08/17-may-to-13-july-2017-4/>
- Froustey, C., Panteleev, I., Lyapunova, E., & Naimarkb, O. (2016). Defect induced shear instability and ASB failure in metals, 2, 1959–1966.
- Gao, Z. guo, Zhang, X. ming, Zhao, Y. sheng, Chen, M. an, & Li, H. jie. (2009). The effect of strain rate on the microstructure of 2519A aluminium alloy plate impacted at 573 K. *Journal of Alloys and Compounds*, 481(1–2), 422–426. <https://doi.org/10.1016/j.jallcom.2009.03.006>
- Garrison, W M, M. N. . (1987). Ductile fracture. *Journal of Physics and Chemistry of Solids*, 48, 1035–1074.
- Graff, S., Forest, S., Strudel, J. L., Prioul, C., Pilvin, P., & Béchade, J. L. (2004). Strain localization phenomena associated with static and dynamic strain ageing in notched specimens: Experiments and finite element simulations. *Materials Science and Engineering A*, 387–389(1–2 SPEC. ISS.), 181–185. <https://doi.org/10.1016/j.msea.2004.02.083>
- Gurson, A. L. (1977). Continuum Theory of Ductile Rupture by Void Nucleation and Growth: Part I—Yield Criteria and Flow Rules for Porous Ductile Media. *Journal of Engineering Materials and Technology*, 99(1), 2. <https://doi.org/10.1115/1.3443401>
- Index of /courstheor/doccourstheo. (2010). Retrieved from <http://www.acop.net/courstheor/doccourstheo/grelejet/Image.image003.jpg@01C778F9.380FAE10.jpg> easy
- Jean-Philippe Crété. (2013). *Traitement numérique de la fissuration d'une structure navale*. Université de Bretagne Sud.
- Johnson, and W. H. Cook, G. R. (n.d.). A constitutive model and data for metals subjected to large strains, high strain rates and high temperatures. In *Proceedings of the 7th International Symposium on Ballistic*, P. 541, The Hague, The Netherland, 1983. The Hague, The Netherlands.
- Kaiser, M. A. (1998). *Advancements in the Split Hopkinson Bar Test*. Mechanical Engineering. Virginia Polytechnic Institute and State University, Blacksburg Virginia.
- Kalthoff, J. F., & Bürgel, A. (2004). Influence of loading rate on shear fracture toughness for failure mode transition. *International Journal of Impact Engineering*, 30(8–9), 957–971. <https://doi.org/10.1016/j.ijimpeng.2004.05.004>
- Kalthoff, J. F., & Winkler, S. (1987). Failure mode transition at high rates of shear loading in:

- C.Y. Chiem, H.-D. Kunze, L.W. Meyer (Eds.), *Proceedings of the International Conference on Impact Loading and Dynamic Behaviour of Materials, 1*, 185–195.
- Kim, J. H., Kim, D. H., & Moon, S. I. (2004). Determination of Dynamic Fracture Toughness Using Strain Measurement. *Key Engineering Materials*, 261–263, 313–318.
- Kolsky, H. (1949). An investigation of the mechanical properties of materials at very high rates of loading. *Proceedings of the Physical Society*, 62, 676–700. <https://doi.org/10.1088/0370-1301/62/11/302>
- Liang, X. P., Li, H. Z., Huang, L., Hong, T., Ma, B., & Liu, Y. (2012). Microstructural evolution of 2519-T87 aluminum alloy obliquely impacted by projectile with velocity of 816 m/s. *Transactions of Nonferrous Metals Society of China (English Edition)*, 22(6), 1270–1279. [https://doi.org/10.1016/S1003-6326\(11\)61315-0](https://doi.org/10.1016/S1003-6326(11)61315-0)
- Longère, P. (2018). Adiabatic shear banding assisted dynamic failure: Some modeling issues. *Mechanics of Materials*, 116, 49–66. <https://doi.org/10.1016/j.mechmat.2017.03.021>
- Longère, P., Bhogaraju, S., & Craciun, D. (2015). Void collapse/growth in solid materials under overall shear loading. *Mechanics Research Communications*, 69, 1–7. <https://doi.org/10.1016/j.mechrescom.2015.05.009>
- Longère, P., & Dragon, A. (2015). Dynamic vs. quasi-static shear failure of high strength metallic alloys: Experimental issues. *Mechanics of Materials*, 80(PB), 203–218. <https://doi.org/10.1016/j.mechmat.2014.05.001>
- Longère, P., Geffroy, A. G., Leblé, B., & Dragon, A. (2012). *Modeling the transition between dense metal and damaged (microporous) metal viscoplasticity. International Journal of Damage Mechanics* (Vol. 21). <https://doi.org/10.1177/1056789511427472>
- Marchand, A., & Duffy, J. (1988). An Experimental Study of the Formation Process of Adiabatic Shear Bands in a Structural Steel. *Journal of the Mechanics and Physics of Solids*, 36(3), 251–. [https://doi.org/10.1016/0022-5096\(88\)90012-9](https://doi.org/10.1016/0022-5096(88)90012-9)
- Mazeau, C., Beylat, L., Longere, P., & Louvigne, P. F. (1997). On the quantitative evaluation of adiabatic shear banding sensitivity of various titanium alloys. *Journal De Physique. IV : JP*, 7, 429–434. <https://doi.org/10.1051/jp4:1997374>
- MH-17: The Untold Story. Exploring possible causes of the tragedy. (2014). Retrieved from <https://www.youtube.com/watch?v=iuoIw3jBV4g&t=189s>
- Molinari, A., Mercier, S., & Jacques, N. (2013). Dynamic failure of ductile materials. *Procedia IUTAM*, 10, 201–220. <https://doi.org/10.1016/j.piutam.2014.01.019>
- Mondal, C., Mishra, B., Jena, P. K., Siva Kumar, K., & Bhat, T. B. (2011). Effect of heat treatment on the behavior of an AA7055 aluminum alloy during ballistic impact. *International Journal of Impact Engineering*, 38(8–9), 745–754. <https://doi.org/10.1016/j.ijimpeng.2011.03.001>
- Neihouse, I., Pepoon, W., Aeronautical, L., & Force, L. A. (1950). National advisory committee for aeronautics. *Library*.
- Peirs, J., Verleysen, P., Degrieck, J., & Coghe, F. (2010). The use of hat-shaped specimens to study the high strain rate shear behaviour of Ti-6Al-4V. *International Journal of Impact*

- Engineering*, 37(6), 703–714. <https://doi.org/10.1016/j.ijimpeng.2009.08.002>
- Quan, G. Z., Liu, K. W., Zhou, J., & Chen, B. (2009). Dynamic softening behaviors of 7075 aluminum alloy. *Transactions of Nonferrous Metals Society of China (English Edition)*, 19(SUPPL. 3), s537–s541. [https://doi.org/10.1016/S1003-6326\(10\)60104-5](https://doi.org/10.1016/S1003-6326(10)60104-5)
- Rendigs, K. (n.d.). Airbus and current aircraft metal technologies. Retrieved from http://www.polishengineers.org/data/history_activities/18.pdf
- Roux, E., Longère, P., Cherrier, O., Millot, T., Capdeville, D., & Petit, J. (2015). Analysis of ASB assisted failure in a high strength steel under high loading rate. *Materials and Design*, 75, 149–159. <https://doi.org/10.1016/j.matdes.2015.03.025>
- S. -C. Liao, & Duffy, J. (1998). Adiabatic shear bands in a Ti-6Al-4V titanium alloy. *J.Mech.Phys.Solids*, 46(11), 2201–2231.
- Seidt, J. D., & Gilat, A. (2013). Plastic deformation of 2024-T351 aluminum plate over a wide range of loading conditions. *International Journal of Solids and Structures*, 50(10), 1781–1790. <https://doi.org/10.1016/j.ijsolstr.2013.02.006>
- STALEY, J. T., & LEGE, D. J. (1993). Advances in aluminium alloy products for structural applications in transportation. *Le Journal de Physique IV*, 03(C7), C7-179-C7-190. <https://doi.org/10.1051/jp4:1993728>
- Starke E.A. Jr and Staley J.T. (1996). Application of modern aluminum alloys to aircraft. *Pergamon*, 32, 131–172.
- Van Stone, R.H., Cox, T.B., Low, J.R., Psioda, J. A. (1985). Microstructural aspects of fracture by dimple rupture. *International Metal Review*, 30, 157–179.
- Weinong W.Chen, B. S. (2011). *Split Hopkinson(Kolsky) Bar*. Springer.
- Wu, X., Li, L., Liu, W., Li, S., Zhang, L., & He, H. (2018). Development of adiabatic shearing bands in 7003-T4 aluminum alloy under high strain rate impacting. *Materials Science and Engineering A*, 732(March), 91–98. <https://doi.org/10.1016/j.msea.2018.06.087>
- Yang, Y., Li, D. H., Zheng, H. G., Li, X. M., & Jiang, F. (2009). Self-organization behaviors of shear bands in 7075 T73 and annealed aluminum alloy. *Materials Science and Engineering A*, 527(1–2), 344–354. <https://doi.org/10.1016/j.msea.2009.08.032>
- Yang, Y., Zeng, Y., & Gao, Z. W. (2008). Numerical and experimental studies of self-organization of shear bands in 7075 aluminium alloy. *Materials Science and Engineering A*, 496(1–2), 291–302. <https://doi.org/10.1016/j.msea.2008.07.043>
- Zener, C., & Hollomon, J. H. (1944). Effect of strain rate upon plastic flow of steel. *Journal of Applied Physics*, 15(1), 22–32. <https://doi.org/10.1063/1.1707363>
- Zhou, M., Rosakis, A. J., & Ravichandran, G. (1996). Dynamically propagating shear bands in impact-loaded prenotched plates—I. Experimental investigations of temperature signatures and propagation speed. *Journal of the Mechanics and Physics of Solids*, 44(6), 981–1006. [https://doi.org/10.1016/0022-5096\(96\)00003-8](https://doi.org/10.1016/0022-5096(96)00003-8)